
Electronic Thesis and Dissertation Repository

9-23-2016 12:00 AM

Model of the Formation of Iron Oxide Nanoparticles by Irradiation in Aqueous Media

Thomas I. Sutherland
The University of Western

Supervisor
Dr. J Clara Wren
The University of Western Ontario

Graduate Program in Chemistry
A thesis submitted in partial fulfillment of the requirements for the degree in Doctor of Philosophy
© Thomas I. Sutherland 2016

Follow this and additional works at: <https://ir.lib.uwo.ca/etd>

 Part of the [Physical Chemistry Commons](#)

Recommended Citation

Sutherland, Thomas I., "Model of the Formation of Iron Oxide Nanoparticles by Irradiation in Aqueous Media" (2016). *Electronic Thesis and Dissertation Repository*. 4178.
<https://ir.lib.uwo.ca/etd/4178>

This Dissertation/Thesis is brought to you for free and open access by Scholarship@Western. It has been accepted for inclusion in Electronic Thesis and Dissertation Repository by an authorized administrator of Scholarship@Western. For more information, please contact wlsadmin@uwo.ca.

Abstract

This thesis aims to develop the mechanistic understanding of the formation of iron oxide nanoparticles by γ -irradiation. Water breaks down into a wide array of redox active species ($\text{H}\cdot$, $\cdot\text{OH}$, H_2O_2 , $\cdot\text{e}^-_{(\text{aq})}$) uniformly throughout the solution when exposed to ionizing radiation. These species are capable of rapidly interconverting soluble Fe^{2+} and insoluble Fe^{III} species resulting in the formation of nanoparticles with a narrow size distribution. The initial concentration of Fe^{2+} in the solution, the solution pH, the presence of any radical scavengers, the temperature of the reaction, and the dose rate of the Co^{60} source were all parameters investigated to elucidate this mechanism. UV-Vis spectrographic methods, gas chromatography, pH, and transmission electron microscopy were used to study the kinetics of the solution and growing particles. Raman, Fourier transform infrared spectroscopy, x-ray absorption near edge spectroscopy were employed to study the final composition of particles. Computer modelling was employed to model the water radiolysis speciation.

It was found that the growth follows a three stage mechanism. The first stage involves the rapid oxidation of Fe^{2+} to Fe^{III} by $\cdot\text{OH}$ which forms the initial nucleate sites. Lower initial pH values will favour larger particles because the Fe^{III} species will be more soluble and fewer nucleates will form. Lower dose rates will also favour larger particles because fewer nucleates are generated initially. In the second stage, H_2O_2 is responsible for the bulk oxidation of Fe^{2+} which adsorbs on the surface of these initial nucleates. The nucleates convert to mixed oxide FeOOH intermediates. The second stage ends when the reverse reduction reactions are capable of competing with the forward oxidation reactions. Solutions with higher initial Fe^{2+} concentrations stay in the growth stage for longer periods of time resulting in larger particles. The final stage is the pseudo steady-state in which continuous cycling of Fe^{II} and Fe^{III} species by H_2O_2 converts the oxide to magnetite with

residual mixed oxides incorporated in the system. The system continues to undergo radiation-assisted Ostwald ripening. Temperature promotes this ripening by rapidly converting the residual mixed oxides in the system allowing the particles to agglomerate.

Key words: iron oxide, radiolytic oxidation, magnetite nanoparticles, particle growth kinetics, scavenger, pH, temperature, dose rate, nitrous oxide, t-butanol.

Co-authorship Statement

All work presented herein was co-authored with my supervisor Dr. J. Clara Wren. J. Joseph assisted in all articles with experimental measurement and editing. The contributions of others are described below.

Chapter 4: C.J. Sparks assisted with experimental measurement. Z. Wang performed the XANES analysis. Dr. T.K. Sham assisted with analysis of XANES.

Chapter 5: C.J. Sparks assisted with experimental measurement.

Chapter 6: C.J. Sparks assisted with experimental measurement.

Chapter 7: C.J. Sparks assisted with experimental measurement. Z. Wang performed the XANES analysis. Dr. T.K. Sham assisted with analysis of XANES.

Chapter 8: P.A. Yakabuskie et al. are responsible for the previous studies reused here. The publication was replicated with permission.

Acknowledgements

I would like to thank first and foremost my supervisor Dr. J. Clara Wren. Without her guidance and assistance, the submission of this thesis would be impossible. She always strove to serve as an excellent example of diligence and professionalism and for that I am grateful. She always encouraged me to get out and network in conferences and taught me many of the soft skill I know will be invaluable to my future career.

I would like to thank Dr. Dave Wren for his guidance and support through this degree. He was always willing to patiently go through my work and assist me in refining my writing skill.

Dr. Jiju Joseph provided me with a great deal of assistance throughout this degree in experimental approach and in editing. Her knowledge in matter regarding how to perform an experiment proved useful to me time and time again. She was always willing to take extra time to help me edit my work. Her sacrifices will not soon be forgotten.

I would like to thank the CNS for providing me with the CNS Scholarship for PhD Graduate Research. It was because of these funds that I was able to focus on my studies and not worry too much about my home finances.

I would like to thank the members of the Wren group, both past and present. It's amazing to see how much the group has changed inside five short years, but the common thread is that we are all our family away from home. I would like to specifically mention Dr. Susan Howett for always being my calming manatee. She was always more than willing to support my extracurricular endeavors, provided there would be a crunchy snack for her to eat.

Finally, I would like to thank my family, Katherine, Ian, and Duncan Sutherland. The three of them steadfastly supported me, not only these past five years, but for all the

ones before that. They are always willing to celebrate with me when things were going well in lab, or provide a sympathetic ear when things were going less well. They helped me get through the numerous challenges I have faced in my life. It is because of them that I am the man I am today. I do have some bad news for them though: their job is far from over.

Table of Contents

Abstract	ii
Co-authorship Statement.....	iv
Acknowledgements.....	v
Table of Contents	vii
Symbols, Acronyms, and Iron Oxides	xiii
List of Figures	xv
List of Tables	xxiii
List of Appendices	xxiv
Chapter 1. Thesis Objectives and Structure	1
Chapter 2. Technical Background and Literature Review	5
2.1. IRON OXIDES	5
2.1.1. Aqueous Chemistry of the Ferrous and Ferric Species.....	5
2.1.2. The Iron Oxides	7
2.2. IONIZING RADIATION AND RADIATION CHEMISTRY	13
2.2.1. Ionizing Radiation.....	13
2.2.2. Ionizing Radiation’s Interaction with Water.....	15
2.2.3. The CANDU Nuclear Reactor	19
2.3. MECHANISM OF NANOPARTICLE FORMATION.....	24
2.3.1. Conventional Methods to Produce Iron based Nanoparticles.....	25

2.3.2. Radiolytically Induced Particle Formation	30
2.4. REFERENCES	35
Chapter 3. Experimental Principles and Procedures	39
3.1. EXPERIMENTAL PRINCIPLES	39
3.1.1. UV-Vis Spectroscopy	39
3.1.2. Gas Chromatography (GC)	41
3.1.3. pH.....	42
3.1.4. Fourier Transform Infrared Spectroscopy (FTIR)	43
3.1.5. Raman Spectroscopy.....	45
3.1.6. Transmission Electron Microscopy (TEM)	47
3.1.7. X-ray Absorption Near Edge Structure (XANES).....	48
3.1.8. Computer Modelling.....	49
3.2. EXPERIMENTAL PROCEDURES	51
3.2.1. Sample Preparation	51
3.2.2. Sample Irradiation.....	52
3.2.3. Sample Analysis.....	54
3.3. REFERENCES	55
Chapter 4. The Effect of Ferrous Ion Concentration on the Kinetics of Radiation-Induced Iron-Oxide Nanoparticle Formation and Growth	57
4.1. INTRODUCTION	57

4.2. EXPERIMENTAL	57
4.3. RESULTS	60
4.3.1. Analysis of the UV-Vis Absorption Spectrum	60
4.3.2. Kinetics of Iron-Oxide Particle Formation and Growth	62
4.3.3. Effect of $[\text{Fe}^{2+}]_0$ on Reaction Yields at 5-h Irradiation at $0.8 \text{ Gy}\cdot\text{s}^{-1}$	67
4.3.4. Spectroscopic Characterization of the Particles	70
4.3.5. Radiolysis Kinetics Calculations	73
4.4. DISCUSSION	78
4.5. CONCLUSION	85
4.6. REFERENCES	87
Chapter 5. The Effect of pH on the Formation of Iron Oxide Nanoparticles by Radiation	88
5.1. INTRODUCTION	88
5.2. EXPERIMENTAL	88
5.2.1. Sample Preparation	88
5.2.2. Sample Irradiation	89
5.2.3. Sample Analysis	89
5.3. RESULTS AND DISCUSSION	91
5.3.1. Particles prepared at pH 4 - 6	93
5.3.2. Particles Prepared at pH 7 & 8	101

5.3.3. Computational Analysis	108
5.3.4. Mechanism	110
5.4. SUMMARY	114
5.5. REFERENCES	115
Chapter 6. The Effect of Radical Scavengers on the Formation of Iron Nanoparticles ..	116
6.1. INTRODUCTION	116
6.2. EXPERIMENTAL	116
6.2.1. Sample Preparation	116
6.2.2. Sample Irradiation.....	117
6.2.3. Sample Analysis.....	118
6.3. RESULTS	120
6.3.1. Observed Kinetic Behaviour in Different Scavenging Solution Environments	120
6.3.2. Effect of $[\text{Fe}^{2+}]_0$ on Particle Growth in N_2O Saturated Solutions.....	129
6.4. DISCUSSION	132
6.4.1. Mechanism of Particle Formation and Growth.....	132
6.4.2. Effect of Radical Scavengers on Radiolysis Product Concentrations	134
6.4.3. Effects of $[\text{Fe}^{2+}]_0$ and Scavengers on Particle Nucleation and Growth	139
6.5. SUMMARY	140
6.6. REFERENCES	141

Chapter 7. The Effect of Temperature on Iron Oxide Nanoparticle Formation	143
7.1.1. INTRODUCTION	143
7.2. EXPERIMENTAL	144
7.2.1. Sample Preparation	144
7.2.2. Sample Irradiation.....	145
7.2.3. Sample Analysis.....	146
7.3. RESULTS AND DISCUSSION	148
7.3.1. Radiolysis Kinetic Modeling	148
7.3.2. Observed Effect of Temperature on Oxidation Yields After 1-h Irradiation.	151
7.3.3. Effect of Temperature on Particle Composition	155
7.3.4. Effect of Temperature on Particle Composition	158
7.3.5. Effect of Temperature on Particle Formation and Growth Kinetics.....	159
7.4. CONCLUSIONS.....	161
7.5. REFERENCES	162
Chapter 8. The Effect of Dose Rate on the Iron Oxide Nanoparticles Formation.....	163
8.1. INTRODUCTION	163
8.2. EXPERIMENTAL	163
8.2.1. Sample Preparation	163
8.2.2. Sample Irradiation.....	164
8.2.3. Sample Analysis.....	164

8.3. RESULTS	165
8.4. DISCUSSION	168
8.5. CONCLUSION	169
8.6. REFERENCES	170
Chapter 9. Summary and Future Work	171
9.1. SUMMARY	171
9.2. FUTURE WORK	173
Appendix A: Copyrights	177
Curriculum Vitae	182

Symbols, Acronyms, and Iron Oxides

Symbols

A	pre-exponential factor
$A_{\bar{\nu}}$	absorbance at a specific wavelength
D_R	dose rate
d_{5h}	diameter at 5 hours
G_a	G-value of species a
E_a	activation energy
E^0	standard potential
k	rate constant
c	concentration
$\varepsilon_{\bar{\nu}}$	molar extinction coefficient at a specific wavelength
Gy	Gray
I_0	incoming intensity
I	intensity
l	path length
R	universal gas constant
ρ	density
ρ_{H_2O}	density of water
T	absolute temperature
$t_{1/2}$	half life
n	neutron
V_{SHE}	voltage wrt the standard hydrogen cell

Acronyms

3D	
CANDU	Canada deuterium uranium
ccp	cubic close-packed
CLS	Canadian light source
ECD	electron capture detector
fcc	face-centred cubic

FIS	flow injection synthesis
FLY	fluorescence yield
FTIR	Fourier transform infrared
GC	gas chromatography
hcp	hexagonal close-packed
IR	infrared
pH	power of hydrogen
PTFE	polytetrafluoroethylene
SCC	stress corrosion cracking
SXRMB	soft x-ray microcharacterization beam
TCD	thermal conductivity detector
TEM	transmission electron microscopy
TEY	total electron yield
UV-Vis	ultraviolet-visible
XANES	x-ray absorption near edge structure
XRD	x-ray diffraction

Iron Oxides

Feroxyhyte (δ -FeOOH)

Goethite (α -FeOOH)

Akaganéite (β -FeOOH)

Lepidocrocite (γ -FeOOH)

Haematite (α -Fe₂O₃)

Maghemite (γ -Fe₂O₃)

Magnetite (Fe₃O₄)

List of Figures

Figure 2.1 The solubility of Fe ^{II} and Fe ^{III} in solution at various pH values. The solid lines indicate the maximum solubility limit of Fe ²⁺ and Fe ³⁺ above which they will form their solid hydroxides in solution. The blue overlay indicates the concentrations and pH values of the systems studied in this thesis.	6
Figure 2.2: Structural representation of ferrosilite [1].	9
Figure 2.3: Structural representation of goethite [1].	10
Figure 2.4: Structural representation of lepidocrocite [1].	10
Figure 2.5: Structural representation of haematite [1].	11
Figure 2.6: Structural representation of magnetite [1].	12
Figure 2.7: Pictorial representation of the three stages of water radiolysis.	19
Figure 2.8: Diagram of a CANDU nuclear reactor core and primary heat transport system [40].	20
Figure 3.1: A visual representation of a Michelson Interferometer. The beam from the source is split by the mirror in the centre which transmits half of the incident beam to the fixed mirror and reflects half of the incident beam to the variable mirror. These beams both reflect off their respective mirrors and recombine before passing through the sample and into the detector.	44
Figure 3.2: A visual illustration of the processes corresponding to IR absorption, Rayleigh scattering, Stokes shifts, and anti-Stokes shifts. Arrows pointing upward correspond to light absorption processes, while those pointing downward correspond to light emitting processes.	46
Figure 3.3: A visual representation of a) the photo-ejection of a core level electron, b) a higher level electron dropping down to fill the vacancy and emitting a photon in the process,	

and c) a higher energy electron dropping down to fill the hole and releasing the extra energy by ejecting another electron.48

Figure 4.1: (a) UV-Vis absorption spectra of solutions containing 0.5 mM $[\text{Fe}^{2+}]_0$ irradiated for different durations, and the spectrum of ferric nitrate solution, (b) the corresponding deconvoluted spectra of ‘ferric nitrate’ and ferric-nitrate subtracted’, and (c) the absorbances at 304 and 380 nm as a function of irradiation time.....61

Figure 4.2: Kinetic behaviours observed during radiolytic conversion of dissolved ferrous ions to iron oxide/hydroxide nanoparticles for three different $[\text{Fe}^{2+}]_0$, (a) 0.5 mM, (b) 1 mM and (c) 5 mM, at pH 6.0. Four different sets of kinetic data are shown from the top to bottom: $[\text{Fe}^{2+}]$ and $[\text{Fe}^{\text{III}}]$ determined by the ferrozine method, the UV-vis absorbances at 304 nm and 380 nm, $[\text{H}_{2(\text{g})}]$ in the headspace and pH. The three kinetics stages are indicated by the bars at the top of each data set. The lines are drawn to guide the eyes.....64

Figure 4.3: TEM images of the particles formed by γ -irradiation of 0.5 mM $[\text{Fe}^{2+}]_0$ solutions at pH 6.0 as a function of irradiation time (indicated on the images). The bars above the images indicate the kinetic stages.66

Figure 4.4: TEM images of the particles collected after 5-h irradiation at $0.8 \text{ Gy}\cdot\text{s}^{-1}$ of deaerated solutions containing different $[\text{Fe}^{2+}]_0$67

Figure 4.5: Product yields after 5-h irradiation of deaerated solutions containing different $[\text{Fe}^{2+}]_0$ at an initial pH of 6.0, (a) $[\text{Fe}^{\text{III}}]$, (b) $[\text{H}_{2(\text{g})}]$ in the headspace and (c) the average size of particles. The lines representing slopes of 1.0, 1/2 and 1/3 are also shown in respective plots.....69

Figure 4.6: XANES Fe K-edge spectra of the particles formed after 5-h irradiation of solutions containing different $[\text{Fe}^{2+}]_0$ at an initial pH of 6.0, (a) the full TEY, (b) the pre-

edge TEY, (c) the FLY. The XANES spectra of a standard magnetite sample are also shown for comparison.....71

Figure 4.7: (a) Fourier transform infrared spectra and (b) Raman spectra of the particles formed after 5-h irradiation of deaerated solutions containing different $[\text{Fe}^{2+}]_0$ at an initial pH of 6. The reference spectra taken from standard powder samples are shown.....72

Figure 4.8: Calculated concentrations of radiolysis products as a function of irradiation time for deaerated solutions containing different $[\text{Fe}^{2+}]_0$ at an initial pH of 6.0. Only the key radiolysis products critical to the formation of the iron nanoparticles are illustrated here, though many others are present.77

Figure 4.9: Schematic of the main processes occurring in different kinetic stages to form mixed $\text{Fe}^{\text{II}}/\text{Fe}^{\text{III}}$ nanoparticles.....80

Figure 5.1: The solubilities of ferrous and ferric ions (as hydroxides) at 25 °C (taken from Baes and Mesmer [1]). The blue diamond box indicates the span of the variables used in this study.92

Figure 5.2: Kinetic data for solutions containing $[\text{Fe}^{2+}]_0 = 1 \text{ mM}$ and a pH of either 5 or 6. Plots a) compares the hydrogen evolution above the reaction solution as a function of irradiation time, b) shows the pH in the reaction vessel measured as a function of irradiation time, and c) the change in proton concentration.94

Figure 5.3 Transmission electron micrographs of particles formed with initial conditions indicated after 20 minutes and 5 h of irradiation.96

Figure 5.4: FTIR spectra of samples obtained after five hours of irradiation under conditions indicated on the graph. Standard are displayed underneath for reference.....97

Figure 5.5: The Raman spectra of samples prepared from solutions with different pH values which were irradiated for five hours. Standards are displayed underneath for reference..99

Figure 5.6 Raman spectra of two solutions with initial pH of 6 and $[\text{Fe}^{2+}_{(\text{aq})}]_0 = 0.5 \text{ mM}$. The top spectrum was buffered with borate and its pH did not change during the experiment. The bottom spectrum was not buffered and its pH dropped into the acidic region over the course of the reaction.	100
Figure 5.7: TEM images obtained after five hours of irradiation. Both systems were $[\text{Fe}^{2+}]_0 = 0.5 \text{ mM}$ and $\text{pH}_0 = 6$. The ‘buffered’ solution contained 0.01 M borate.	101
Figure 5.8: Kinetic data for solutions containing $[\text{Fe}^{2+}]_0 = 0.1 \text{ mM}$ and a pH of either 6 or 8. a) shows the concentration of Fe^{II} (black squares) Fe^{III} (white squares) measured in the reaction solution as a function of irradiation time, b) compares the hydrogen evolution above the reaction solution as a function of irradiation time, and c) shows the pH in the reaction vessel measured as a function of irradiation time.	102
Figure 5.9: TEM images of particles formed with initial conditions indicated after 20 minutes of irradiation and 5 h of irradiation.	103
Figure 5.10: TEM images of particles from a solution with $[\text{Fe}^{2+}]_0 = 0.1 \text{ mM}$, and a pH_0 of 8. The images were obtained prior to irradiation and after 20 and 60 minutes of irradiation time.	104
Figure 5.11: The Raman spectra of samples prepared from solutions with different pH values and different concentrations which were irradiated for five hours. Standards are displayed underneath for reference.	106
Figure 5.12: Raman spectra of two particle samples grown in solution. The ‘unbuffered’ with an initial pH of 8 and $[\text{Fe}^{2+}]_0$ of 0.1 mM. The ‘buffered’ with an initial pH of 8 and $[\text{Fe}^{2+}]_0$ of 0.1 mM. The top spectrum was buffered with borate and its pH did not change during the experiment. The bottom spectrum was not buffered and its pH dropped into the acidic region over the course of the reaction.	107

Figure 5.13: TEM images obtained after five hours of irradiation. Both systems were $[\text{Fe}^{2+}]_0 = 0.1 \text{ mM}$ and $\text{pH}_0 = 8$. The ‘buffered’ solution contained 0.01 M borate.	108
Figure 5.14: Computer modelling performed to simulate the key radiolysis products generated in pure water solutions held at constant pH.....	109
Figure 5.15: Computer modelling performed to simulate the key radiolysis products generated in Fe^{2+} solutions held at constant pH.....	110
Figure 6.1: Kinetic behaviours observed during radiolytic conversion of dissolved ferrous ions to iron oxide/hydroxide nanoparticles for 0.5 mM $[\text{Fe}^{2+}]_0$ solutions containing different scavengers, (a) 26 mM t-butanol, (b) free of scavenger and (c) N_2O . Four different sets of kinetic data are shown from the top to bottom: $[\text{Fe}^{2+}]$ and $[\text{Fe}^{\text{III}}]$ determined by the ferrozine method, the UV-vis absorbances at 304 nm and 380 nm, pH (or $\Delta[\text{H}^+]$) and $[\text{H}_{2(\text{g})}]$ in the headspace. The three kinetics stages are indicated by the bars at the top of each data set.	123
Figure 6.2: TEM images of the particles formed as a function of irradiation time in solutions containing 0.5 mM $[\text{Fe}^{2+}]_0$ with a different scavenger, (a) 26 mM t-butanol, (b) free of scavenger and (c) N_2O	125
Figure 6.3: Raman spectra of the particles formed after 5-h irradiation in 0.5 mM $[\text{Fe}^{2+}]_0$ solutions with different scavengers. Shown below are the reference spectra taken with standard powder samples of different iron oxides.	127
Figure 6.4: Kinetic behaviours observed during radiolytic conversion of dissolved ferrous ions to iron oxide/hydroxide nanoparticles in N_2O saturated solutions containing (a) 0.1 mM $[\text{Fe}^{2+}]_0$, (b) 0.5 mM $[\text{Fe}^{2+}]_0$ and (a) 1.0 mM $[\text{Fe}^{2+}]_0$. Three different sets of kinetic data are shown from the top to bottom: $[\text{Fe}^{\text{II}}]$ and $[\text{Fe}^{\text{III}}]$ determined by the ferrozine method,	

[H_{2(g)}] in the headspace, and pH (or Δ[H⁺]). The three kinetics stages are indicated by the bars at the top of each data set. Note that the data are presented in two different time scales to show the changes observed in Stages 1 and 2 more clearly. 130

Figure 6.5: TEM images of the particles collected following γ-irradiation for different durations of 0.1 mM [Fe²⁺]₀ solution with or without N₂O. Irradiation times are indicated above the images. 131

Figure 6.6: TEM images of the particles collected following γ-irradiation for different durations of 1 mM [Fe²⁺]₀ solution with or without N₂O. Irradiation times are indicated above the images. 132

Figure 6.7: Calculated concentrations of radiolysis products as a function of irradiation time for deaerated solutions at pH 6.0, (a) free of a scavenger, (b) saturated with N₂O or (c) with t-butanol (0.026 M). The top row presents the results for the solutions free of iron species and the bottom row presents those for the solutions initially containing 0.5 mM [Fe²⁺]₀ under the same scavenging conditions. Only the key radiolysis products critical to the formation of the iron nanoparticles are illustrated here, though many others are present. 137

Figure 7.1: Temperature profiles of the reaction vessel. Irradiation began once the vessel reached 40 °C (the vertical red line) and reached the target temperature within 10 minutes of irradiation start time. 145

Figure 7.2: Computational modelling results for the radiolysis of pure water at different temperatures. The results obtained for two solution pHs, 6.0 and 3.0, are compared. Only the concentrations of key radiolysis products that are relevant to iron-oxide formation are shown although many more species are considered in the model. 149

Figure 7.3: Computational modelling results for the radiolysis of 0.5 mM $[\text{Fe}^{2+}]_0$ solutions at different temperatures. The results obtained for two solution pHs, 6.0 and 3.0, are compared. Only the concentrations of key radiolysis products that are relevant to iron-oxide formation are shown although many more species are considered in the model. The concentration of Fe^{2+} remains nearly constant at 0.5 mM over the calculated reaction period of 100 s and hence, is not shown. 149

Figure 7.4: The measured concentrations of Fe^{2+} and $\text{Fe}_{(\text{total})}$ in the solution after one hour as a function of temperature with and without radiation. 152

Figure 7.5: The hydrogen concentrations determined after an hour in a solution of either 0.5 mM $[\text{Fe}^{2+}]_0$ or pure water at pH 6. 153

Figure 7.6: The fluorescent emission spectrum of three samples prepared with an initial pH of 6 and concentrations of 1 mM Fe^{2+} for 20 °C while 60 and 80 °C had concentrations of 0.5 mM. Each sample was prepared at a different temperature in the range of 20-80 °C. They are compared to a standard magnetite sample. 156

Figure 7.7: The electron emission spectrum of three samples prepared with an initial pH of 6 and concentrations of 1 mM Fe^{2+} for 20 °C while 60 and 80 °C had concentrations of 0.5 mM. Each sample was prepared at a different temperature in the range of 20-80 °C. They are compared to a standard magnetite sample. The graph on the left (a) is the full Fe K-edge while the graph on the right (b) is a magnification on the pre-K edge region. 156

Figure 7.8: Raman spectra obtained from samples irradiated at the temperature indicated on the graph. The 20 °C sample was irradiated for five hours, while those irradiated at 40 °C or higher were irradiated for one hour. 157

Figure 7.9: TEM images of the particles formed after 1-h irradiation of 0.5 mM $[\text{Fe}^{2+}]_0$ solutions at various temperatures (from left to right 20 °C, 40 °C, 60 °C and 80 °C).....159

Figure 7.10: TEM images of particles all obtained from a sample with $[\text{Fe}^{2+}]_0 = 0.5$ mM, a pH of 6, heated to 80 °C, and irradiated for an hour.....159

Figure 7.11: Schematic of the proposed particle growth mechanism of radiolysis-assisted Ostwald ripening.161

Figure 8.1: The concentration of Fe^{III} in solution as a function of irradiation time. Both systems modelled had $[\text{Fe}^{2+}]_0 = 0.5$ mM. One system (black) had a dose rate of 1.9 Gy/s and a pH of 5.5, while the other (grey) had a dose rate of 0.8 Gy/s and a pH of 6.....165

Figure 8.2: TEM images of particles obtained after 5 h of irradiation with $[\text{Fe}^{2+}]_0 = 0.5$ mM. The image on the left had a dose rate of 0.8 Gy/s and an initial pH of 6, while that on the right had a dose rate of 1.9 Gy/s and an initial pH of 5.5 which were obtained from Yakabuskie et al [1].166

Figure 8.3: Computer modelling of the relevant radiolysis products as a function of irradiation time.....167

Figure 8.4: The concentration of Fe^{III} in solution as a function of irradiation time. Both systems modelled had $[\text{Fe}^{2+}]_0 = 0.5$ mM. One system (black) had a dose rate of 1.9 Gy/s and a pH of 5.5, while the other (grey) had a dose rate of 0.8 Gy/s and a pH of 6.....168

List of Tables

Table 2.1: Crystallographic information and stability of the iron oxides discussed.....	13
Table 2.2: G-values of the primary radiolysis products in liquid water at 25 °C for γ -rays. All values reported in $\mu\text{mol}\cdot\text{J}^{-1}$ [28].....	18
Table 4.1: Averages and standard deviations of the sizes of particles formed after 5-h irradiation of solutions containing different $[\text{Fe}^{2+}]_0$ at $3.0 \text{ kGy}\cdot\text{h}^{-1}$	67
Table 5.1: Average particle sizes and standard deviation determined at the $[\text{Fe}^{2+}_{(\text{aq})}]_0$ and pH studied.	96
Table 6.1: Rate of hydroxyl radical production and time to reach saturation limit of Fe^{III} in the presence of various scavengers.	139
Table 8.1: Average particle sizes and standard deviation determined at $[\text{Fe}^{2+}_{(\text{aq})}]_0 = 0.5 \text{ mM}$. The sample with a dose rate of 0.8 Gy/s had an initial pH of 6 while that of 1.9 Gy/s had an initial pH of 5.5.	166

List of Appendices

Appendix A: Copyrights

Chapter 1. Thesis Objectives and Structure

This thesis explores the mechanism by which iron oxide nanoparticles are formed under continuous gamma irradiation. The main outcome of this research work has two major practical applications. Firstly, this work provides a technical basis for the assessment of corrosion product and activity transport in a reactor coolant circuit system. Secondly this phenomenon is exploitable to produce nanoparticles for industrial and medicinal use.

Our objective is to develop a mechanistic understanding of radiation-induced nanoparticle formation from dissolved corrosion products in a reactor core environment. One of the major issues for nuclear power plants arises from corrosion product and activity transport in the reactor coolant circuit. Corrosion of coolant circuit piping releases dissolved metal ions (such as iron) into the coolant. In the heat transport circuit, the reactor coolant is subjected to high flux of ionizing radiation. Since the solubility of metal species depends strongly on temperature, the concentration of dissolved metal ions in the coolant can exceed its solubility limit as the coolant passes through the lower temperature region. This can lead to the formation of insoluble solids ('crud') that deposit on the coolant pipes, which reduce the heat transfer efficiency. The dissolved metal ions once transported to the reactor core can neutron activate and become radioactive. For e.g ^{54}Fe and ^{56}Fe can be neutron activated to form radioactive ^{55}Fe with $t_{1/2}$ of 2.74 years. If the radioactive solids are resuspended into the coolant and deposit outside the biological shield of the reactor core, they can cause a risk to the reactor maintenance workers. Most reactors have on-line coolant purification systems which are often not effective for removing colloids or particulates less than $0.1\ \mu\text{m}$.

Radiation-induced nanoparticle formation is a promising technique for generating nano-scale particles with a uniform size distribution. When exposed to ionizing radiation water decomposes to a number of different reacting species which are uniformly distributed throughout the system on a short timescale. The radiolysis products include both oxidizing (e.g., $\bullet\text{OH}$, H_2O_2 , and O_2) and reducing (e.g., $\bullet\text{H}$, $\bullet\text{e}_{\text{aq}}^-$, and $\bullet\text{O}_2^-$) species. These species control the redox state of the water and can readily interact with any dissolved species present in the water. Metal species present in the water can be oxidized or reduced by these species in the system. Differing oxidation states of metals often have different solubilities from one another. As such, rapidly converting between oxidation states can lead to solid formation in the solution. Under continuous radiation conditions, these reactions are driven so quickly that these growing solids are unable to agglomerate together and instead form nanoscale particles. This phenomenon has the potential to present a new and facile method for nanoparticle formation for a variety of metal species.

Generally, the formation of nanoparticles by chemical methods requires the addition of harsh chemical additives in order to maintain a narrow size distribution. These additives need to be removed after post synthesis in order for these particles to be useful. This method does not suffer from this drawback, but does keep a narrow size distribution. Once the system is removed from the gamma source, the final products include trace amounts of hydrogen peroxide, hydrogen and oxygen. The hydrogen and oxygen can diffuse out of the system while the peroxide will decompose to water and oxygen on its own.

Metals are thought to undergo this phenomenon provided they have oxidation states with differing solubilities and that the oxidation change (reduction or oxidation of the

metal) is a favoured conversion under continuous radiation. Iron, copper, chromium, and cobalt all form nanoparticles under continuous irradiation.

This work analyzes the oxidation and reduction of Fe^{II} and Fe^{III} species in solution. Ferric iron, Fe^{III}, is orders of magnitude less soluble than ferrous iron, Fe^{II}, at a range of pHs. Owing to the rapid and uniform distribution of the water decomposition products, any Fe^{II} in the system is oxidized too rapidly to less soluble Fe^{III} resulting in the formation of nanoparticles. Initial studies have shown that the phenomenon exists. No studies currently exist that explore the effects of the environment on particle size, composition, and morphology. These studies would also provide valuable information on the mechanistic understanding of this process. Unlike many other metals for which this phenomenon is available, iron has a whole host of potential oxides as which it can precipitate. This study aims to bridge this gap in knowledge.

Computer modelling was performed in order to analyze the mechanism by which these particles form. To perform this modelling, the numerous reactions which occur under continuous radiation in water were input into a FACSIMILE program and the key iron reactions of interest were also input in order to match the model with the data acquired. The experimental results are presented and discussed in a series of chapters.

- The effect of initial [Fe²⁺_(aq)] on the particle growth kinetics, size, and composition was studied.
- The effect of the initial solution pH on the particle growth kinetics, size, and composition was studied. Studies were performed in which (a) the solution pH was allowed to fluctuate during irradiation and (b) the solution contained a buffer to prevent pH fluctuations.

- The effect of radical scavengers on the particle growth kinetics, size, and composition were studied. The scavengers removed either the hydroxyl radical or the solvated electron which are important to the production of these particles.
- The effect of solution temperature during irradiation on the particle growth kinetics, size, and composition was studied. Analogous experiments were performed with and without radiation in order to isolate the effect of temperature.
- The effect of dose rate on the particle growth kinetics, size, and composition was studied. The studies performed herein compared to previous work which was identical experimentally except using a higher dose rate.

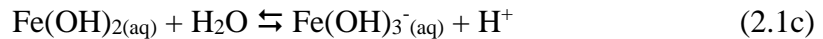
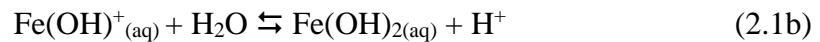
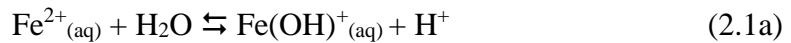
Chapter 2. Technical Background and Literature Review

2.1. IRON OXIDES

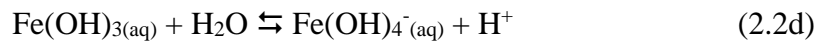
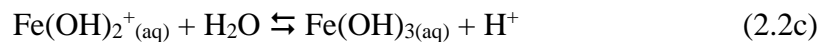
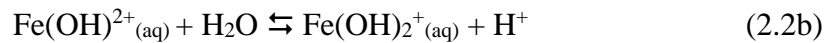
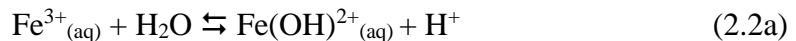
Iron is one of the most abundant elements on Earth. Due to its reactivity with both water and oxygen it is most often found in its oxidized states of Fe^{II} and Fe^{III}. Even elemental iron, given contact to oxidizing environments, such as in the primary heat transport system of a nuclear reactor, will undergo oxidation to form a Fe^{II} or Fe^{III} compound. Fe^{II} and Fe^{III} can exhibit sixteen unique structures in the form of oxides, oxyhydroxides, and hydroxides making up the iron oxide family.

2.1.1. Aqueous Chemistry of the Ferrous and Ferric Species

In solution, Fe²⁺ is hydrolyzed by water.

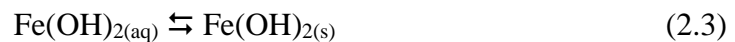


Analogous reactions exist for the Fe³⁺ ion.



Of the above reactions, the charged species are water soluble. The sum concentrations of the charged species in water determine the solubility of Fe^{II} and Fe^{III} species in solution.

The neutral species are insoluble which rapidly reach equilibrium with its solid state.



Once the solid forms of either of the iron hydroxides are formed they are capable of agglomerating together. These are the precursor of ordered crystal formation. The likelihood of water expulsion, forming an oxyhydroxide and finally an oxide, increases as the charge on the initial monomer decreases and hence increases as the pH of the solution (abundance of OH^- is increased) [1].

The concentration of charged species vary with pH due to the hydrolysis equilibria (reactions 2.1 & 2.2). Thus, the solubilities of ferrous and ferric ions (or other transition metals) depend strongly on pH [2]. The pH dependences of ferrous and ferric ion solubilities are shown in Figure 2.1.

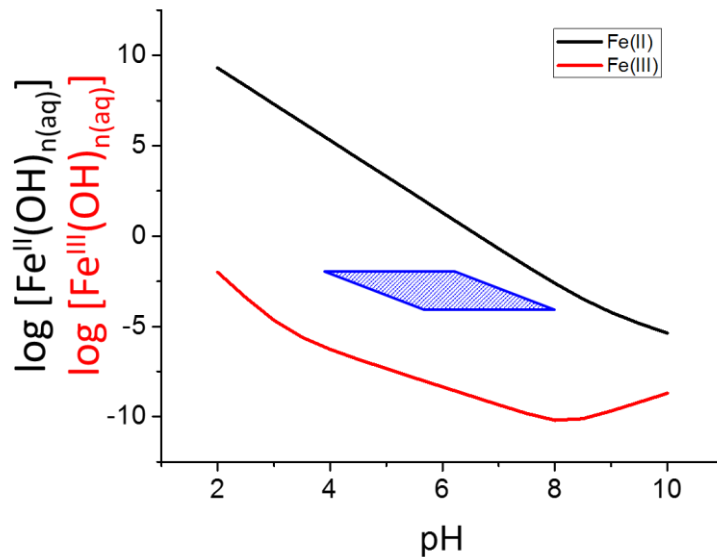


Figure 2.1 The solubility of Fe^{II} and Fe^{III} in solution at various pH values. The solid lines indicate the maximum solubility limit of Fe^{2+} and Fe^{3+} above which they will form their solid hydroxides in solution. The blue overlay indicates the concentrations and pH values of the systems studied in this thesis.

2.1.2. The Iron Oxides

The iron oxides exist in a variety of forms. These forms exhibit different behaviours. The following section details a few features of a selection of oxides. Lepidocrocite, haematite, and goethite make up the most common forms of iron oxide found in nature [3]. Magnetite and maghemite are less common than the aforementioned three. Finally, ferrihydrite, ferrihydrite, and green rust are transient oxides which tend to transform to other forms.

These oxides can interconvert between one another given certain conditions [4]. The main reactions which these oxides use to undergo transformations are classified as isochemical (no change in molecular formula; change in phase), dehydrations (loss of water), dehydroxylations (loss of OH^-), and oxidation/reduction (change of oxidation state). Broadly speaking these reactions follow two types of pathways: solid-state rearrangements and dissolution/reprecipitation. Solid-state rearrangements are possible between two structures that have similar 3D structural arrangements. These reactions generally need elevated temperatures as it requires atom rearrangement in the solid. Dissolution/reprecipitation rearrangements have no structural relationship from precursor to the final product. Because these do not require elevated temperatures, dissolution followed by reprecipitation is the main pathway taken to transform oxides in nature. The solution kinetics of the iron species also impacts the resultant oxide [1].

The dominant oxide to form depends on a variety of factors such as temperature [5], concentration [6], impurities [7], pressure, and environment [3, 8, 9]. Corrosion on iron surfaces also exhibits different oxide formation behaviour dependant on any species present in the oxide [10, 11], and on exposure to oxidizing environments [12].

2.1.2.1. *Green Rust*

A newer addition to the iron oxide family is green rust. It exhibits a mixed oxidation state of iron which can vary depending on the environment. It consists of $\text{Fe}^{\text{II}}(\text{OH})_6$ stacked octahedra with some Fe^{II} replaced with Fe^{III} . The positive charge is countered by anions between the octahedral sheets. These anions can be Cl^- (green rust I), SO_4^{2-} (green rust II), or CO_3^{2-} (fougèrite). They tend to form from corrosion of iron in oxygen deficient environments, but are extremely unstable in atmospheric conditions [1, 13]. Green rusts are suitable for removing pollutants from drinking water [14].

2.1.2.2. *Ferrihydrite*

Ferrihydrite is poorly ordered and varies depending on the water content. Because of this, the structure has been difficult to truly elucidate. The chemical formula of ferrihydrite is nominally $5\text{Fe}_2\text{O}_3 \cdot 9\text{H}_2\text{O}$. There exist two extreme structures that have been proposed, two-line and six-line. The six-line structure, which is the more ordered of the two, has been proposed as an hcp array of O^{2-} anions (like that of haematite), but with more Fe^{III} vacancies and a significant amount of water present. Two line ferrihydrite is the less ordered of the two structures. The proposed structure proposes locally ordered regions of four corner-sharing octahedrally coordinated Fe^{III} . The two structures are distinguishable by their XRD patterns with exhibit two broad lines for the two-line structure and six lines for the six-line structure. Ferrihydrite is a metastable oxide which forms from the rapid hydrolysis of Fe^{3+} solutions and from the rapid oxidation of Fe^{II} . It usually converts to more crystalline structures [15, 16], but this can easily be blocked by the chemical environment [1].

2.1.2.3. *Feroxyhyte* (δ - $FeOOH$)

Feroxyhyte consists of a disordered hcp structure of anions with the Fe^{III} distributed through the octahedral interstitial sites. The arrangement of the Fe^{III} is ordered as sheets of edge sharing octahedral sites adjacent to completely vacant layers (Figure 2.2). Ferroxyhyte is isostructural with $Fe(OH)_2$ and can form from the rapid oxidation of Fe^{II} species [1]. Ferroxyhyte shares structural similarities with goethite based on XRD evidence [17].

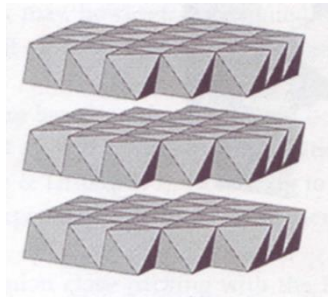


Figure 2.2: Structural representation of feroxyhyte [1].

2.1.2.4. *Goethite* (α - $FeOOH$)

Goethite is made of an hcp arrangement of OH^- and O^{2-} groups. The Fe^{III} groups arrange themselves in half of the octahedral sites within the structure. They form two double chains of face sharing Fe^{III} octahedra with a double layer of vacant sites adjacent to them. These chains are connected to the layer of Fe^{III} above through corner sharing octahedral (Figure 2.3) [1]. Goethite can form in most aqueous systems provided they have a source of Fe^{III} (be it from Fe^{II} oxidation or Fe^{3+} precipitation).

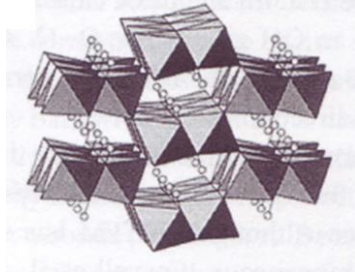


Figure 2.3: Structural representation of goethite [1].

2.1.2.5. *Lepidocrocite (γ -FeOOH)*

Lepidocrocite is commonly formed through the weathering of iron substances in aqueous environments [18]. This form can exhibit coloration from yellowish to a reddish-brown. On a microscale, the oxide has an orthorhombic structure. It consists of ccp stacking of the O^{2-}/OH^- groups. The Fe^{III} occupy half of the octahedral sites between these oxy/hydroxy groups, but they stack in two adjacent rows with two empty rows of octahedral sites (Figure 2.4). The structure is held together by the hydrogen bonds throughout the structure which gives the oxide its flaky behaviour on the macroscale [1].

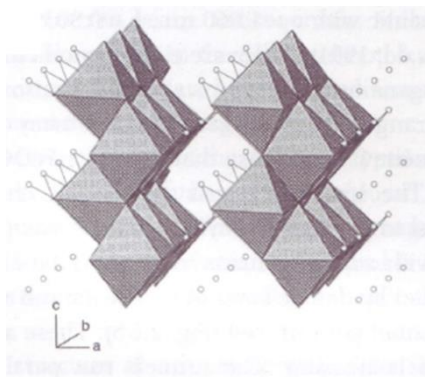


Figure 2.4: Structural representation of lepidocrocite [1].

In natural environments they often form from green rusts (discussed above) [19]. In a synthetic context it can be brought about by rapidly increasing the pH of an aqueous Fe^{2+} solution.

2.1.2.6. Haematite ($\alpha\text{-Fe}_2\text{O}_3$)

Haematite has a rhombohedral structure. The O^{2-} groups are structured in an hcp arrangement. Two thirds of the octahedral interstices are filled sites followed by a vacant one. This results in $\text{Fe}^{\text{III}}(\text{O})_6$ coordination of the iron species (Figure 2.5). This coordination will share a face with a neighbouring $\text{Fe}^{\text{III}}(\text{O})_6$ group which results in the Fe^{III} molecules repelling one another. This results in a deviation from ideal packing of the two cations shifting towards the unoccupied face. Haematite forms from higher temperature aqueous systems [1].

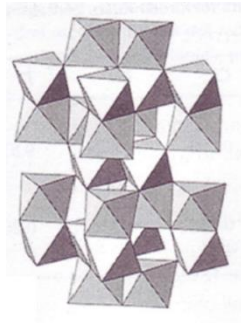


Figure 2.5: Structural representation of haematite [1].

2.1.2.7. Maghemite ($\gamma\text{-Fe}_2\text{O}_3$)

Maghemite is made up of an fcc arrangement of O^{2-} anions with the Fe^{III} filling all of the tetrahedral interstices and most of the octahedral interstices. The vacancies in the octahedral interstices are distributed at random throughout the structure. The structure of

maghemite is similar to that of magnetite (Figure 2.6) in that magnetite consists of sites filled with Fe^{II} and Fe^{III} not simply Fe^{III}. Because of this there exists intermediate structures between the two oxides with varying degrees of oxidation [1].

2.1.2.8. Magnetite (Fe_3O_4)

As mentioned above, the structure of magnetite is similar to that of maghemite. It is made up of an fcc arrangement of O²⁻ groups. The Fe^{III} cations occupy both the tetrahedral interstices as well as the octahedral interstices, while the Fe^{II} cations are limited to the octahedral sites (Figure 2.6). Magnetite is unique in the family of iron oxides as it is the only oxide with a mixed oxidation state of the iron. It exhibits magnetic properties and has held an important industrial position in both the past and present. It is formed in alkaline systems from a Fe^{II}/Fe^{III} solution, a green rust intermediate, or a ferrihydrite intermediate [1].

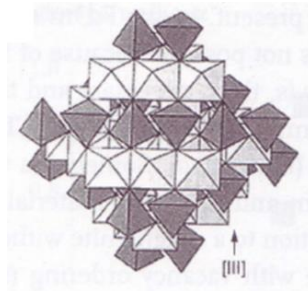


Figure 2.6: Structural representation of magnetite [1].

2.1.2.9. Summary

Table 2.1 summarizes the oxides discussed above. Though the crystal habit is noted within the table is the most common habit. Crystal habit can be influenced by a number of factors in the environment and the same oxide can grow in a number of different ways.

Table 2.1: Crystallographic information and stability of the iron oxides discussed.

Oxide	Crystal Structure	Standard free energy (kJ/ mol)	Crystal Habits
Ferrihydrite	Hexagonal	-699	Spheres
Feroxyhyte	Hexagonal	N/A	Plates
Goethite	Orthorhombic	-488.6	Acicular
Lepidocrocite	Orthorhombic	-477.7	Laths
Haematite	Rhombohedral hexagonal	-742.7	Hexagonal plates
Maghemite	Cubic or tetragonal	-711.1	Laths or cubes
Magnetite	Cubic	-1012.6	Octahedra

2.2. IONIZING RADIATION AND RADIATION CHEMISTRY

Ionizing radiation is a powerful driver of chemical processes. It delivers huge amounts of energy into a system which can promote unconventional reactivity in systems. This reactivity has most readily been studied in the contexts of its destructive powers [8, 9, 11, 20-22], but more and more inquiry is being directed towards its synthetic applications [23-27]. The following will outline the fundamentals of ionizing radiation and some environments in which it is found.

2.2.1. Ionizing Radiation

Ionizing radiation is any type of radiation which can ionize particles as it passes through a medium. Chemistry driven by ionizing radiation relies on fundamentally different processes than that of the non-ionizing radiation studied in photochemistry. Ultraviolet, visible, and infrared radiation are capable of exciting target molecules if there is an energy transition within the target molecule that matches the energy of the radiation. The photon is totally absorbed by this process on a one-to-one basis with the target molecule. In this way, photochemistry is seen as a solute specific process in that it will only interact with target molecules that have the matching energy gap which they can excite.

Ionizing radiation on the other hand, has such a high amount of energy that there is no excitation in the molecule which matches the energy which the photon or particle contains. As ionizing radiation passes through a medium it undergoes Compton scattering, wherein it deposits an amount of its energy into the target molecule (most probable events deposit near 0 or near 100 % of the photon's energy). This results in an excited state or the ionization of the molecule by the ejection of an electron. Unlike photochemistry, the photons involved in radiation chemistry are able to excite multiple molecules as it passes through the medium. As Compton scattering is not a selective processes, the ionizing radiation will interact with any molecules and so radiation chemistry is said to be a solvent specific process in that the nature of the medium plays the most important role in the radiation chemistry of the system [28].

Particle irradiation is caused by particles with such high kinetic energy that they are capable of ionizing the medium as they pass through before being absorbed into the medium. Particle radiation, such as the irradiation by He^{2+} (α -particles) or $\cdot e^-$ (β -particles), interacts with the electron cloud surrounding the nucleus. It typically has short penetration depths and does not drive water chemistry as significantly as γ -radiation or neutron radiation (n-radiation).

High energy photons (γ -rays) have the longest penetration depth. This type of radiation interacts primarily through Compton scattering. The photon is absorbed by a target molecule and then reemitted resulting in ejected electrons. These ejected electrons have huge amounts of kinetic energy with which they cause secondary ionization events throughout the solution. Because the chance of Compton scattering is relatively low compared to the inelastic collisions of particle irradiation, γ -rays penetrate much more

deeply into a medium. The probability of a scattering event also decreases as the energy of the photon decreases resulting in photons that become less and less likely to be consumed as they travel. Shielding for γ -rays typically requires a dense material with a thickness of a few inches [28].

Despite being particles, neutrons do not have the same fundamental dominant interactions with matter as α - or β - particles. Being neutral, the neutron interacts with the nucleus of an atom rather than its electron cloud. Neutrons are taken out by two main interactions. When a neutron strikes a hydrogen atom it has the ability to force the nuclear recoil of hydrogen producing a fast proton which can go on to ionize other species along its path. With most other forms of matter, neutrons are captured by the nucleus to produce (in most cases) a radioactive isotope which will ionize the system around it as it decays and releases the types of radiation described above. Neutron radiation is an indirect ionizing source of radiation because the ionization of the medium is the result of the interaction by the products of the nucleus' reactions rather than its own interaction. Its penetration depth is long because it has a low probability of interacting with matter. Neutrons can, in some cases, be more penetrating than γ -rays because the process with which they interact with matter is different. Unsaturated hydrocarbons are used most effectively to shield neutron irradiation as it promotes the formation of fast protons and diminishes the effect of neutron capture by other atoms [28].

2.2.2. Ionizing Radiation's Interaction with Water

Section 2.2.1 describes the way with which these radiation forms interact with water, but it says nothing about what happens when these events occur. The chemistry of

a system under a radiation source has two kinetically distinct processes: primary processes, and pseudo steady-state kinetics. The primary processes of radiation are well characterized in the literature [29-34]. The longer term pseudo steady-state is less well understood on a kinetic level [35, 36].

2.2.2.1. Primary Processes in an Aqueous Medium

The focus of this thesis is on the chemistry driven in an aqueous medium. The fundamentals discussed herein are generally applicable to any system, but the following discussion will focus on the processes present in water. For all of these different types of radiation, the processes remain the same, but the density of these interactions has long-term consequences for the products' abundances. When radiation deposits energy in the system it can break down the target molecule, in a process known as radiolysis. The deposited energy can excite the target molecule or eject an electron completely. In water this means the two initial processes are excitation to produce a highly unstable water molecule (H_2O^*) or ionization producing an ion pair ($\text{H}_2\text{O}^+ + \text{e}^-_{(\text{hot})}$). These processes occur on the order of $10^{-16} - 10^{-14}$ s which is referred to as the physical stage of radiolysis. Ejected electrons (hot electrons) can go on to initiate one or two more excitation events within a spur or along a branch to the main radiation path before it becomes thermalized by the medium ($\text{e}^-_{(\text{sol})}$). This result in two to three ions or excited species formed per interaction with radiation [28].

Following this, these spurs of excited and ionized species begin to diffuse and interact with the medium around them as they relax from their unstable states. These relaxations can involve rotational and vibrational relaxations as well as bond formation and dissociation. As these molecules relax they can form ion pairs as well as radical pairs. Ion-ion pair recombination (geminate recombination) is driven by electrostatic attraction

between the ions formed. The probability of this recombination is dominated by the dielectric constant of the medium. For species with high dielectric constants, the medium is capable of shielding the ions from their geminate pair with only a short distance between them making the escape of ion pairs from each other more probable. In mediums with low dielectric constants, the medium is ineffective at shielding the charge on ions and thus they will be attracted towards each other even if they have a high distance between them. Water is a high dielectric constant medium meaning more of the geminate ion pairs formed do not recombine and instead react with other species than of other mediums. As these species diffuse through the system they react with themselves and the species surrounding them to form ions, radicals, and molecular species ($\text{H}\cdot$, $\text{OH}\cdot$, $\text{e}_{(\text{aq})}^-$, H_2O^+ , OH^- , H_2O_2 , etc.). These produced species though must still react with species in close proximity to them as the system is still somewhat diffusion limited. These processes dominate on the order 10^{-14} – 10^{-7} s and is referred to as the physiochemical stage of radiolysis [28].

The abundance of products which will persist and react when the system becomes homogeneous is dependent on the nature of the medium and on the nature of the radiation used. The medium will determine the probability that the products of radiolysis can escape one another and thus react with their surroundings. For every species produced in this way there is a corresponding G-value. A G-value is a linear proportionality constant that related the energy deposited into a system to the concentration of a species generated by the primary processes. The rate of species generation by radiolysis is dependant linearly on the dose rate of the system and consequently the units are expressed as $\mu\text{mol}\cdot\text{J}^{-1}$. An example table of G-value for γ -radiation is below in Table 2.2 This value is a constant dependant on the type of radiation and temperature of the system which permits concentration

calculations from the absorbed dose of the system. A more detailed discussion of the calculations involved with G-values can be found in section 3.1.8. These values are largely independent of any solutes in the system [37]. Despite the general scientific consensus on these values, the inherent difficulty in studying speciation at such a short time scale has left some discussion unresolved on the exact values in higher temperature conditions and supercritical conditions [38, 39].

Table 2.2: G-values of the primary radiolysis products in liquid water at 25 °C for γ -rays. All values reported in $\mu\text{mol}\cdot\text{J}^{-1}$ [28].

Species	H ₂ O	H ⁺	e _(aq) ⁻	•OH	•H	H ₂	H ₂ O ₂
γ-ray 0.1–20 MeV	-0.43	0.28	0.28	0.28	0.062	0.047	0.073

2.2.2.2. Long term speciation of an irradiated system

These G-values provide the initial estimate of the products brought into existence from radiation driven processes, but once the system becomes homogeneous, reactions between these created species and the surrounding medium begin to dominate. These processes are distinct from those discussed in the context of the primary processes because the reactions here are not controlled by the type of radiation. The primary processes are estimated using pulse radiolysis experiments. Once the species generated by radiolysis diffuse homogeneously through the system, the kinetics can be described using conventional means using the reaction rates and respective concentrations [28].

As the system is continuously irradiated, the radiolysis products will continue to be formed, but they will be removed by further chemical processes in the system. The analyses of these rates and the interconnectedness of the concentration of these species are not feasibly solved manually. Instead, commercially available software is employed to

estimate the system speciation for long term irradiation. This software is described in detail in Chapter 3. The products formed in the primary processes reach equilibrium on a small time scale, but their concentrations will slowly alter with time as the system kinetics change due to slow processes such as interfacial mass transfer and corrosion or other such processes and thus the system is said to have reached pseudo steady state in the μs time scale. This corresponds to the chemical stage of the radiolysis process [28].

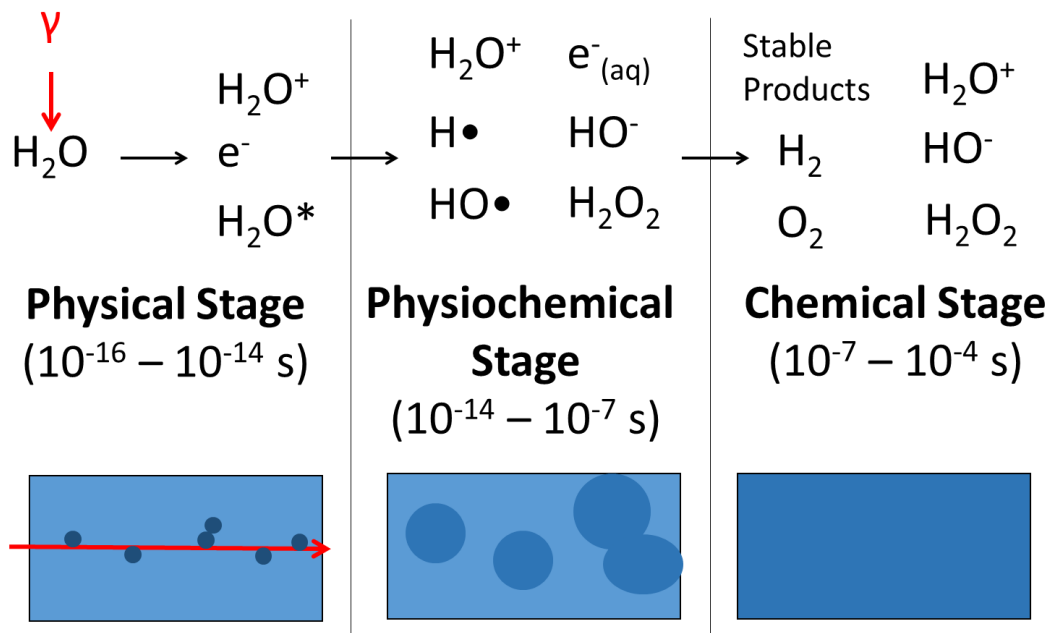


Figure 2.7: Pictorial representation of the three stages of water radiolysis.

2.2.3. The CANDU Nuclear Reactor

A nuclear reactor is fundamentally a method to boil water. The CANDU nuclear reactor design (Figure 2.8) uses the energy stored in the nucleus to heat water. Heat is generated in the core of the reactor by the fission of the fuel. The primary heat transport system transports the heat from the core to the steam generator. The steam generator, a part of the secondary heat transport system, will use the heat to generate the steam which will

condense further along the secondary heat transport system. The condensed steam spins the turbine to generate power before cycling back through to the steam generator.

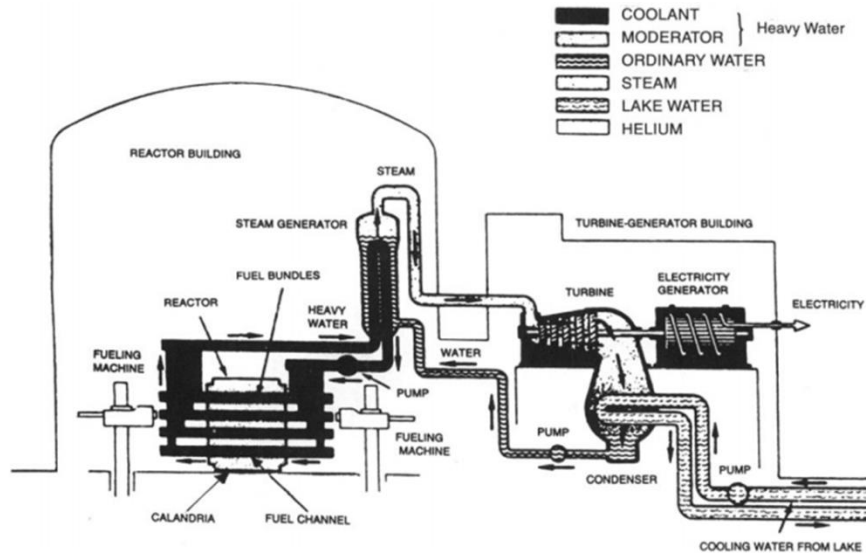


Figure 2.8: Diagram of a CANDU nuclear reactor core and primary heat transport system [40].

2.2.3.1. The core

Nuclear reactor designs use the energy stored in the nucleus to heat water. The fuel of the nuclear reactor system is uranium. Natural uranium is composed primarily of ^{235}U (0.72 %) and ^{238}U (99.28 %). The isotope of interest is that of ^{235}U which is capable of undergoing nuclear fission which produces power. CANDU reactors require no further enrichment of natural uranium, while the light water builds require enrichment of the ^{235}U isotope to $> 2.5\%$ [41].

The core of the CANDU nuclear reactor is made up of a system of pressurized fuel rods housed in a massive tank of moderator called the Calandria. The fuel bundles are composed of a number of ceramic rods composed of UO_2 sealed inside a tube made of zircaloy. Zircaloy is an alloy composed predominantly of zirconium, which has a small

neutron cross section. This permits neutrons to freely pass between the fuel bundles, another feature to make unenriched uranium a viable fuel. The fuel rods are surrounded by a small amount of helium in order to slow the heat transport by errant neutrons between the fuel and the moderator. The fuel bundles are loaded into the pressurized tubes over which the heavy water of the primary heat transport system flows. The Calandria, which houses these fuel rods, is essentially a large vessel filled with heavy water. The vessel is kept at a near-neutral pH. The coolant is able to degrade radiolytically to form D_2O_2 , D_2 , and O_2 . In order to control the concentration of these species, the cover He gas, into which these volatile species enter, is cycled through a hydrogen recombination unit in order to regenerate the D_2O . In the event of total failure of other safety features, the Calandria is capable of absorbing a large amount of heat generated by fission giving operators more time to find a solution [40].

Adjustor rods made of stainless steel are raised and lowered into the Calandria in order to control the rate of fission in the reactor. The stainless steel is able to absorb neutrons to kill the fission processes. These rods are held up by electromagnets. In the event of a power failure these rods would automatically lower into the Calandria and kill the fission processes. Should these rods fail, the Calandria is equipped with injection ports which will fill the system with gadolinium nitrate. Gadolinium nitrate is a neutron poison and will effectively kill fission in the reactor. Both of these systems work independently of one another and are capable of independently killing the fission. Even if both of these systems fail, the fuel rods themselves offer some protection against reactor melt down. They run horizontal to the Calandria and with elevates temperatures will sag in the middle.

The neutron flux in the fuel diminishes as the rod sags until the system cannot maintain the fission process [40].

2.2.3.2. The primary heat transport system

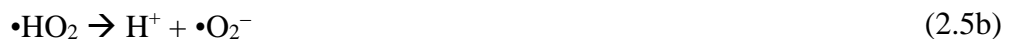
The primary heat transport system is flowing pressurized heavy water which absorbs the heat from the fuel rods and transports it to a steam generator to dissipate the heat before returning to the fuel rods. Refueling can be performed while the reactor is still in operation because the fuel rods are housed in their own independently pressurized systems. The piping is made up of zircaloy for the portions that run through the core, and are made of carbon steel throughout the rest of the system. The heavy water is kept near pH = 10.0 – 10.5 [42]. CANDU reactors maintain these pH values because it corresponds to the minimum solubility of iron species at elevated temperatures and promotes the formation of magnetite as the primary corrosion product which forms a protective layer on the piping. The system enters the core at a temperature of around 250 °C and increases to 300 °C as it passes through the core [40, 41].

Heavy water is used in the primary heat transport system. Deuterium has a lower neutron capture cross section than hydrogen does. This means that using heavy water allows the fission process to remain critical with a smaller amount of fissile material. In the light water designs, the uranium needs to have its ^{235}U enriched. The use of heavy water, and other specification in the CANDU design, allows unenriched uranium to be used as the fuel or uranium which has already been used in the light water reactors. This reduces the cost of processing the fuel before it can be used and allows fuels from other reactors to be

recycled. This also helps prevent nuclear weapons proliferation by eliminating the need for facilities which can enrich uranium [40, 41].

Oxidation of the piping occurs by both uniform and non-uniform processes. In systems with elevated electrochemical activity, metal surfaces have a tendency to undergo stress corrosion cracking (SCC) which is difficult to monitor in the reactor and can lead to unpredictable lifetimes of metal components [43]. Furthermore, oxidation releases soluble metal species into the system. Due to the temperature gradient through the system, the solubility of these species will change over the cycle, which will promote precipitation of metal oxide. These precipitates can deposit onto the surface of the piping which diminishes the heat transport efficiency. These precipitates can become neutron-activated by errant neutrons in the core. These precipitates may then resolubilize and travel elsewhere in the primary heat transport system resulting in a buildup of radioactive material in less effectively shielded areas in the system. This will decrease the amount of time employees can safely work in local areas and therefore increase the cost of energy generation. Metal species have the ability to perturb the chemistry control in the primary heat transport system.

The two most problematic species which contribute to the corrosion of piping are oxygen and hydrogen peroxide. Hydrogen peroxide is produced in the initial spurs of water radiolysis, while oxygen is produced through the following series of reactions:



In order to suppress these reactions, hydrogen is added to the system to promote reactions which will consume hydrogen peroxide and prevent the formation of oxygen by consuming hydroxyl radicals, the reactant in R 2.5.



Though hydrogen is formed by the radiolysis processes, it is not formed in sufficient quantities in order to drive the following reactions. The quantity of dissolved hydrogen (or rather deuterium) required to promote reaction 2.6 in the CANDU reactor is determined experimentally. Work to reconcile this value with computational models is ongoing [44].

2.3. MECHANISM OF NANOPARTICLE FORMATION

Nanoparticles are particles sized from 1 to 100 nm. As particle size decreases, interesting and size dependant properties begin to emerge in these particles which are unique from bulk sized masses. These properties tend to emerge at 100 nm or lower hence the limitation. That being said, for other purposes, such as filtration, particles of less than 500 nm can be considered nanoscaled. As discussed in Section 2.1.2 iron oxides can be formed in a variety of ways. They will not generate nanoparticles unless care is taken to control the size and aggregation of the growing particles. This is best controlled by controlling the chemistry in which the particles grow [45, 46].

The two main kinetic reactions which dictate size and morphology of nanoparticle formation are nucleation and growth. To generate nanoparticles, the rate of nucleation needs to be sufficiently high to generate sites on which particles can grow while the rate of

growth needs to be sufficiently slow or limited to prevent the particles from agglomerating or growing beyond the nanoscale.

2.3.1. Conventional Methods to Produce Iron based Nanoparticles

Nanoparticles synthesised in lab are predominantly made of magnetite and maghemite, this is because of their superparamagnetic properties. They find use in many fields such as data storage, magnetic resonance imaging, catalysis, and sensors. There are many different routes for making these nanoparticles discussed below along with some broader strategies for avoiding aggregation of the particles [45].

Because the focus of this thesis is on iron and the iron oxides, the following discussion limits itself to nanoparticles composed of iron or anything in the iron oxide family. Several reviews explore the in depth synthesis of iron oxide nanoparticles [45-49]. The conventional methods to do this are discussed below along with some novel radiation based methods.

2.3.1.1. Co-precipitation

The co-precipitation method is a method whereby Fe^{II} and Fe^{III} are precipitated in an alkaline medium to produce magnetite particles. This reaction can be carried out homogeneously in an aqueous environment [50, 51]. To provide further control of particle synthesis, a heterogeneous environment can be created wherein the Fe²⁺ and Fe³⁺ are dissolved in an aqueous phase and the base is dissolved in an oleic phase [52-54].

In the homogeneous mechanism of reaction, precipitation is brought about from the alkalization of the system by a base. This is thought to proceed through FeOOH intermediates (akaganéite, β -FeOOH, followed by goethite, α -FeOOH) at mid-range pH values followed by a topotactic conversion to Fe₃O₄. In addition to this main pathway, the

Fe^{2+} in solution can undergo a rapid nucleation to ferrous hydroxide which converts to γ -FeOOH by oxidation which subsequently converts to magnetite at sufficiently alkaline pH values [55, 56]. The reaction proceeds via a rapid nucleation step once the solution becomes supersaturated followed by a slower growth step as the species migrate to the nucleates. The nucleation step will dictate the number of particles produced while the growth step most heavily influences their final size and size distribution. Separating these steps helps control the size distribution of the particles formed [48]. Increasing temperature can alter the particle composition and increase crystallinity [57].

In heterogeneous environments caused by the presence of micelles, the reaction mechanism is similar to that discussed above though the base and iron species may only interact at the interface. The key differences are that the magnetite is thought to form not from a FeOOH polymorph precursor, but instead from a 2-line ferrihydrite precursor. The nucleation and growth of the particles are based at the water-oil interface. As the particles grow they begin to move towards the water because of the hydrophilic character of the particles and thus growth ceases once the particle moves away from the interface [58].

Another variation of this technique is called flow injection synthesis (FIS) technique. In this method, the reagents are continuously fed into a capillary reactor in a segmented fashion in order to restrict the particle size. This method produced highly reproducible particles of small sizes (2-7 nm) using a co-precipitation reaction as its synthetic strategy [59]. Functionalized particles can be prepared using co-precipitation making it a versatile synthetic approach [60].

2.3.1.2. Droplet Synthesis

Synthesis in constrained environments involves the synthesis of these nanoparticles in environments wherein the environmental factors prevent the particles from growing beyond a certain size [61]. This is accomplished using reverse micelles in an oil-water environment. Surfactants are added to form these reverse micelles which work as nanoreactors in which the reaction is driven. These methods are highly tunable because the surfactant and conditions can be changed to greatly change the resultant particles. Unfortunately, these methods require purification of the nanoparticles from their parent solutions for various uses which can be technically challenging. These methods generate particles of uniform size because the environment limits the maximum size a particle can grow by limiting a bulk system into a finite number of nanosized systems in which particle growth is allowed to grow to its maximum size [62, 63].

Aerosol techniques can also generate nanoparticles. In this technique, a solution of iron precursor salts and some reducing agent are sprayed into a reactor. The aerosol nature of the droplets is maintained in the reactor as the environment is heated. As the solvent is evaporated the solutes react and condense to form a uniform particle size. Once the solvent has dried, further reactions cannot take place [64, 65].

2.3.1.3. High Temperature Synthesis

High temperature synthesis exploits the decomposition of inorganic iron salts at high temperatures which are the source of iron in these reactions. They control the size of the resultant nanoparticles by giving a degree of control over the competing nucleation and growth processes. Nucleation processes tend to be favoured at higher temperatures while

growth is favoured with longer reaction times. Additives are often included in the reaction vessel in order to stabilize the particles and prevent them from aggregating together.

An example of this is the decomposition of iron pentacarbonyl at high temperatures. In this reaction iron pentacarbonyl is dissolved in an oleic medium and heated to 100 °C which drives the decomposition of the precursor. These reactions generate iron nanoparticles which can be processed after their formation to form other oxides if desired [66]. The presence of surfactants can also catalyze the reaction by promoting the expulsion of a CO molecule [67]. The exact mechanism of decomposition is complex and can be altered by the presence of catalytic species [46].

2.3.1.4. Sol-gel Techniques

Sol-gel is a useful technique for embedding iron nanoparticles within a gel, commonly an SiO₂ matrix. Iron precursors are solubilized in solution and allowed to hydroxylate and condense. As the solution is aged it becomes gel like while 3D iron networks are formed. The sol portion of the reaction is carried out at room temperature though the final product needs to be heat treated in order to achieve the final product (a xerogel). The iron oxide nanoparticles are stabilized by the gel as they are embedded in and prevented from agglomerating. The final 3D structure of the gel is dependent on the prevailing structures in the sol of this process. The final products are highly dependent on the kinetics of the condensation and hydroxylation which leads to high tunability with the rate of agitation, pH, solution temperature, reaction time, and concentrations [68-71].

A variation on this process is referred to as the polyol process wherein the initial sol is made from a polyol (e.g polyethylene glycol) instead of the silica based system. The

polyols are capable of reducing dissolved iron in the system to form solid iron nucleated sites within the structure [72, 73]. Because of the higher boiling point of the polyols, the reaction has a greater temperature range. The ability to heat the reaction helps promote the nucleation of iron oxide nanoparticles and decreases final particle size or shortens required reaction times. The heating is also important as it decomposes the polyol and removes it from the reaction. The advantages of this system include higher crystallinity and more monodispersed particles [45].

2.3.1.5. Electrochemical

Electrochemical techniques have been employed to control the size of nanoparticles. These methods are able to control the particle size by controlling the current density passing through the system which in turn will dictate the rate of nucleation and of growth. Because these rely on relatively low temperature synthesis by electrochemical deposition, they can produce poorly ordered structures with impurities impregnated in the structure [45, 47].

2.3.1.6. Photochemistry and Laser Pyrolysis

Iron pentacarbonyl decomposes on exposure to non-ionizing radiation to form iron plate-like nanoparticles [74]. In order to more precisely control the size, laser pyrolysis is used. In laser pyrolysis, a flowing gas is passed through a laser beam. The laser is able to rapidly nucleate particles. Once the gas has passed through the laser it no longer reacts and thus particle sizes are controlled. A suitable reactant for this is iron pentacarbonyl (discussed in 2.3.1.3) which is stable in gas phase [45, 75, 76].

2.3.1.7. *Sonolysis*

Sonolysis can also be used to drive the decomposition of iron precursors to form iron oxide nanoparticles [77, 78]. The sonication of the reaction solution generates localized areas of elevated temperatures which are capable of decomposing the precursor. This drives the nucleation of localized particles [45].

2.3.2. Radiolytically Induced Particle Formation

In addition to the above mentioned techniques, new techniques involving radiations are being investigated. The key advantages they offer over the conventional methods are that they generally require mild conditions (ambient pressure and temperature) and achieve high degrees of replicability. The radiation acts as the driving force and thus there is no need for harsh chemical reducing or oxidizing agents. Control over dose rate provides control over the particle features. These methods generally exploit the fact that a metal species has different solubilities at different oxidation states. The radiation is used to induce an oxidation change from a more soluble oxidation state to a sparingly soluble oxidation state in order to precipitate the product [26].

The generation of nanoparticles involves the competition of nucleation events with growth. By altering the radiation dose it is possible to change the size and morphology of the resultant particles. Higher doses tend to generate more nucleation events which deplete the concentration of metal salt available for particle growth. Thus higher doses tend towards a greater number of smaller particles. There are however exceptions to this rule. Higher dose rate can also facilitate radical crosslinking between particles [79].

2.3.2.1. *Metallic Particles*

Metallic nanoparticles have been synthesized from a variety of metals using radiation [25, 80-84]. In order to produce metallic particles, it is possible to dissolve a soluble metal salt species and then reduce the non-zero valence metal to its zero-valency. Radiation generated a range of redox active species which includes both the hydrated electron, $e^-_{(aq)}$ and hydrogen atom, $H\bullet$, which are each powerful reducing agents. These species reduces the metallic species to their zero oxidation state driving their precipitation. Water radiolysis also produces oxidizing species such as the hydroxyl radical, $\bullet OH$, which is capable of oxidizing particles as they are formed. In order to diminish the effect of the hydroxyl radical and make reduction the dominant reaction, hydroxyl radical scavengers are added into the solution to pre-emptively react with the hydroxyl radicals [79].

Nanoparticles in solutions, with nothing to stop them, will aggregate together with time. In order to prevent this process polymeric stabilizers are added into the solution to prevent nanoparticles from growing beyond a certain nuclearity. In this way, the rate of particle growth is limited to a certain size at which point growth will cease and the particle size will not change.

Systems in which multiple metals are dissolved have been studied within the context of metallic particle generation. Within these studies three outcomes are expected [79]. Alloys are produced when the two metal ions have similar probabilities of associating with the growing cluster and undergoing a subsequent reduction [85, 86]. Typically the more easily reduced ion will generate the initial nucleate, but association of metal ions has no strong preference between metals. These are best generated with low dose rates which allow the association and subsequent reductions to dominate rather than using up much of

the metal ions in homogenous reduction [87, 88]. Core/shell structures are produced when one metal completely reduces before the other metal ion can compete. The more easily reduced metal forms the core of the structure and once it is exhausted, the second metal undergoes association and reduction on the surface [89]. Heterostructures are produced when the two metals in the system nucleate individually and then subsequently grow together. This can be achieved by virtue of rapid reduction of both metal ions, or through using presynthesized nanoparticles of one of the metals [90].

The solution conditions, such as solvent, pH, and precursor concentration, and ionic strength tailor the nanoparticles synthesized [91]. The stabilizer present is responsible for preventing aggregation and in scavenging oxidants. Different stabilizers will ultimately change the way the reducing agent interacts with the particle. The slower the reduction interaction is, the narrower the size distribution of the nanoparticles. The pH of the solution impacts how well the precursor will associate with the stabilizer, the rate of reoxidation of the metal, and finally whether or not there will be any precipitation prior to irradiation. Each metal precursor will have an optimum pH that can be determined experimentally [92, 93]. As the concentration of metal ions in the initial solution increases, so too does the size of the particles formed. As the metal ion concentration increases the metal ions have a higher adsorption probability, more nucleates form and increases their collision likelihood, and the capping ability of the stabilizer is reduced. All three of these effects are conducive to the formation of larger particles. Ionic strength of the solution tends to favour larger particles. High ionic strength solutions result in short Debye lengths for the particles. This effect destabilizes smaller particles and shifts the average size larger [94].

The radiation provides the driving force for the nucleation of the particles. As such, it is able to influence the properties of the resultant particles by way of its control over the rate of nucleation. The greater the dose rate, the smaller the particles which are produced [95]. This is true within an electron beam [83] and using gamma rays [87]. This happens because at low dose rates, fewer nucleations occur and so more of the metal ion is able to reduce by adsorbing on the surface of the particle and reducing on it and so the metal ions are distributed over fewer nucleation sites. At higher doses, more of the initial metal ion is consumed in making nucleates and therefore there is less metal ions available for growth which will be distributed over more nucleates [79, 96].

2.3.2.2. *Oxides*

The formation of metal oxides from solubilized metal salt without the addition of additives is possible for a number of metals [97-100]. In this method, the redox potential of the resulting irradiated bulk solution is sufficient to drive oxidation and reduction. Either oxidation or reduction can be used to generate nanoparticles, it depends on the solubility of the differing oxidation states and the ability of the radiolysis products to drive a change in oxidation state from a more soluble oxidation state to a less soluble one. Unlike the synthetic approach for zero valent metals, metal oxide nanoparticles are generated in the presence of both highly oxidizing and highly reducing species and the competition between these reactions is critical to control for the size and composition of the particles formed. Viability of this method varies from metal to metal. It is dependent on the stability and solubility of the oxides which the metal forms. Stabilizers are required to form zero valent nanoparticles because the oxidizing species generated in water radiolysis are sufficiently

powerful to oxidize any metallic particles formed. Conversion between oxidation states is possible even in the redox active environment generated by water radiolysis.

Cobalt(II) salts are oxidized by the hydroxyl radicals formed by water radiolysis. The mechanism goes through three stages. The initial nucleates are generated by oxidation by atmospheric oxygen to form Co(OH)_2 particles. These nucleates eventually convert to CoOOH and finally to Co_3O_4 by the water radiolysis products. The composition of the particles becomes more and more dehydrated with increasing irradiation time. The size of these particles is controlled by the competition of the oxidation of more cobalt with the reduction of the solid particles [99].

Oxidation need not be the only route by which metal oxide nanoparticles can be generated. Chromium salts have also been investigated as the precursor for metal oxide nanoparticles generated this way. In this method chromium(VI) is reduced by the radiolysis products to chromium(III). The reduced chromium(III) complexes to form Cr(OH)_3 sites which act as the initial nucleates of the system. From there, further reduction occurs on the surface of the nucleates to convert the Cr(OH)_3 to Cr_2O_3 . Again, once the oxidation reaction is able to compete with the continued reduction of chromium(VI), the reaction reaches steady state and growth slows. The particles can still grow by radiation assisted Ostwald ripening [100].

The iron system has been studied as well. Unlike chromium and cobalt, Iron has a variety of oxides which can readily interconvert. This thesis aims to clarify the kinetic details of the formation of metal oxide nanoparticles by radiation induced precipitation in the iron system. The effect of concentration, solution pH, scavengers, temperature, and dose rate are all explored within this thesis.

2.4. REFERENCES

- [1] R.M. Cornell, U. Schwertmann, *The iron oxides: structure, properties, reactions, occurrences and uses*, VCH, Weinheim; New York, (1996).
- [2] C.F. Baes, R.E. Mesmer, *The Hydrolysis of Cations*, Robertt E. Krieger Publishing Company, Inc., Malabar, (1976).
- [3] J. Prietzel, J. Thieme, K. Eusterhues, D. Eichert, *Eur. J. Soil Sci.*, 58 (2007) 1027-1041.
- [4] I. Mitov, D. Paneva, B. Kunev, *Thermochim. Acta*, 386 (2002) 179-188.
- [5] R. Al-Gaashani, S. Radiman, N. Tabet, A.R. Daud, *J. Alloys Compd.*, 550 (2013) 395-401.
- [6] D. Fu, P.G. Keech, X.L. Sun, J.C. Wren, *Phys. Chem. Chem. Phys.*, 13 (2011) 18523-18529.
- [7] A.-C. Senn, R. Kaegi, S.J. Hug, J.G. Hering, S. Mangold, A. Voegelin, *Geochimica Et Cosmochimica Acta*, 162 (2015) 220-246.
- [8] R.J. Winsley, N.R. Smart, A.P. Rance, P.A.H. Fennell, B. Reddy, B. Kursten, *Corrosion Engineering Science and Technology*, 46 (2011) 111-116.
- [9] N. Fujita, C. Matsuura, K. Saigo, *Radiat. Phys. Chem.*, 58 (2000) 139-147.
- [10] M.B. Lin, C.J. Wang, A.A. Volinsky, *Oxid. Met.*, 76 (2011) 161-168.
- [11] F.R. Perez, C.A. Barrero, K.E. Garcia, *Corrosion Science*, 52 (2010) 2582-2591.
- [12] A.J. McLeod, R.E. Clegg, *Mater. Corros.*, 64 (2013) 381-387.
- [13] J. Swietlik, U. Raczyk-Stanislawiak, P. Piszora, J. Nawrocki, *Water Res.*, 46 (2012) 1-10.
- [14] K. Hanna, T. Kone, C. Ruby, *Environ. Sci. Pollut. Res.*, 17 (2010) 124-134.
- [15] R.K. Kukkadapu, J.M. Zachara, J.K. Fredrickson, S.C. Smith, A.C. Dohnalkova, C.K. Russell, *Amer. Mineral.*, 88 (2003) 1903-1914.
- [16] H. Boumaiza, S. Naille, A. Renard, B. Gregoire, M. Mallet, C. Ruby, *Desalin. Water Treat.*, 53 (2015) 1031-1036.
- [17] M. Sestu, D. Carta, M.F. Casula, A. Corrias, G. Navarra, *J. Solid State Chem.*, 225 (2015) 256-260.
- [18] A. Liu, J. Liu, B. Pan, W.-x. Zhang, *RSC Adv.*, 4 (2014) 57377-57382.
- [19] Y.N. Vodyanitskii, *Eurasian Soil Science*, 43 (2010) 1244-1254.
- [20] L. Wu, D. Guo, A. Van Belois, J.J. Noël, P.G. Keech, J.C. Wren, Radiation-assisted corrosion of carbon steel nuclear waste container, in: 17th International Conference on Environmental Degradation of Materials in Nuclear Power Systems – Water Reactors, 2015.
- [21] O.P. Maksimkin, M.N. Gusev, K.V. Tsai, A.V. Yarovchuk, O.V. Rybalchenko, N.A. Enikeev, R.Z. Valiev, S.V. Dobatkin, *Phys. Met. Metall.*, 116 (2015) 1270-1278.
- [22] P. Tawema, J. Han, K.D. Vu, S. Salmieri, M. Lacroix, *LWT Food Sci. Technol.*, 65 (2016) 451-456.
- [23] V. Cuba, T. Pavelkova, J. Barta, T. Gbur, M. Vlk, A. Zavadilova, J. Indrei, Z. Docekalova, M. Pospisil, V. Mucka, *Radiat. Phys. Chem.*, 81 (2012) 1411-1416.
- [24] J. Belloni, M. Mostafavi, H. Remita, J.L. Marignier, M.O. Delcourt, *New J. Chem.*, 22 (1998) 1239-1255.
- [25] A. Henglein, M. Giersig, *J. Phys. Chem. B*, 103 (1999) 9533-9539.

- [26] C. Dispenza, N. Grimaldi, M.A. Sabatino, I.L. Soroka, M. Jonsson, *J. Nanosci. Nanotechnol.*, 15 (2015) 3445-3467.
- [27] C.R. Walker, K. Pushpavanam, D.G. Nair, T. Potta, C. Sutiyo, V.D. Kodibagkar, S. Sapareto, J. Chang, K. Rege, *Langmuir*, 29 (2013) 10166-10173.
- [28] J.W.T. Spinks, R.J. Woods, *An introduction to radiation chemistry*, Wiley, New York, (1990).
- [29] M.S. Alam, M. Kelm, B.S.M. Rao, E. Janata, *Radiat. Phys. Chem.*, 71 (2004) 1087-1093.
- [30] J.F. Yang, T. Kondoh, K. Norizawa, R. Nagaishi, M. Taguchi, K. Takahashi, R. Katoh, S.V. Anishchik, Y. Yoshida, S. Tagawa, *Radiat. Phys. Chem.*, 77 (2008) 1233-1238.
- [31] J. Ma, U. Schmidhammer, M. Mostafavi, *J. Phys. Chem. A*, 118 (2014) 4030-4037.
- [32] C.M. Stanisky, D.M. Bartels, K. Takahashi, *Radiat. Phys. Chem.*, 79 (2010) 64-65.
- [33] B.G. Ershov, A.V. Gordeev, M. Kelm, E. Janata, *Radiat. Phys. Chem.*, 67 (2003) 613-616.
- [34] T. Pálfi, L. Wojnárovits, E. Takács, *Radiat. Phys. Chem.*, 79 (2010) 1154-1158.
- [35] K. Daub, X. Zhang, J.J. Noël, J.C. Wren, *Electrochim. Acta*, 55 (2010) 2767-2776.
- [36] R.S. Glass, G.E. Overturf, R.A. Van Konynenburg, R.D. McCright, *Corros. Sci.*, 26 (1986) 577-590.
- [37] M. Domae, Y. Katsumura, K. Ishigure, V.M. Byakov, *Radiat. Phys. Chem.*, 48 (1996) 487-495.
- [38] Y. Muroya, J. Meesungnoen, J.P. Jay-Gerin, A. Filali-Mouhim, T. Goulet, Y. Katsumura, S. Mankhetkorn, *Can. J. Chem.*, 80 (2002) 1367-1374.
- [39] G. Baldacchino, V. De Waele, H. Monard, S. Sorgues, F. Gobert, J.P. Larbre, G. Vigneron, J.L. Marignier, S. Pommeret, M. Mostafavi, *Chem. Phys. Lett.*, 424 (2006) 77-81.
- [40] L. Atomic Energy of Canada, *Canada enters the nuclear age: a technical history of Atomic Energy of Canada Limited*, Published for Atomic Energy Canada Limited by McGill-Queen's University Press, Montreal, (1997).
- [41] G. Kessler, *Sustainable and Safe Nuclear Fission Energy: Technology and Safety of Fast and Thermal Nuclear Reactors*, Springer-Verlag, Dordrecht, (2012).
- [42] A. Filipovic, *Material and Fabrication Considerations for the CANDU-PHWR Heat Transport System*, Atomic Energy of Canada Limited, CANDU Operations, (1987).
- [43] M.E. Indig, J.L. Nelson, *Corrosion*, 47 (1991) 202-209.
- [44] D.M. Bartels, J. Henshaw, H.E. Sims, *Radiat. Phys. Chem.*, 82 (2013) 16-24.
- [45] S. Laurent, D. Forge, M. Port, A. Roch, C. Robic, L.V. Elst, R.N. Muller, *Chem. Rev.*, 108 (2008) 2064-2110.
- [46] D.L. Huber, *Small*, 1 (2005) 482-501.
- [47] D. Ramimoghadam, S. Bagheri, S.B.A. Hamid, *J. Magn. Magn. Mater.*, 368 (2014) 207-229.
- [48] M.A. Mohapatra, S., *IJEST*, 2 (2010) 127-146.
- [49] M.A. Willard, L.K. Kurihara, E.E. Carpenter, S. Calvin, V.G. Harris, *Int. Mater. Rev.*, 49 (2004) 125-170.
- [50] Y.S. Kang, S. Risbud, J.F. Rabolt, P. Stroeve, *Chem. Mater.*, 8 (1996) 2209-2211.
- [51] T. Fried, G. Shemer, G. Markovich, *Adv. Mater.*, 13 (2001) 1158-1161.
- [52] P. Tartaj, C.J. Serna, *Chem. Mater.*, 14 (2002) 4396-4402.

- [53] Y. Lee, J. Lee, C.J. Bae, J.G. Park, H.J. Noh, J.H. Park, T. Hyeon, *Adv. Funct. Mater.*, 15 (2005) 503-509.
- [54] K. Tao, H. Dou, K. Sun, *Chem. Mater.*, 18 (2006) 5273-5278.
- [55] T. Ahn, J.H. Kim, H.-M. Yang, J.W. Lee, J.-D. Kim, *J. Phys. Chem. C*, 116 (2012) 6069-6076.
- [56] D.K. Kim, M. Mikhaylova, Y. Zhang, M. Muhammed, *Chem. Mater.*, 15 (2003) 1617-1627.
- [57] O. Karaagac, H. Kockar, T. Tanrisever, *J. Supercond. Novel Magn.*, 24 (2011) 675-678.
- [58] K. Tao, H.J. Dou, K. Sun, *Colloids Surf., A*, 320 (2008) 115-122.
- [59] G. Salazar-Alvarez, M. Muhammed, A.A. Zagorodni, *Chem. Eng. Sci.*, 61 (2006) 4625-4633.
- [60] R. Bhandari, P. Gupta, T. Dziubla, J.Z. Hilt, *Mater. Sci. Eng., C*, 67 (2016) 59-64.
- [61] P.A. Dresco, V.S. Zaitsev, R.J. Gambino, B. Chu, *Langmuir*, 15 (1999) 1945-1951.
- [62] X. Cheng, B. Wu, Y. Yang, Y. Li, *Catal. Commun.*, 12 (2011) 431-435.
- [63] O.A. Graeve, H. Fathi, J.P. Kelly, M.S. Saterlie, K. Sinha, G. Rojas-George, R. Kanakala, D.R. Brown, E.A. Lopez, *J. Colloid Interface Sci.*, 407 (2013) 302-309.
- [64] S. Gurmen, B. Ebin, *J. Alloys Compd.*, 492 (2010) 585-589.
- [65] T. González-Carreño, M.P. Morales, M. Gracia, C.J. Serna, *Mater. Lett.*, 18 (1993) 151-155.
- [66] T. Hyeon, S.S. Lee, J. Park, Y. Chung, H.B. Na, *J. Am. Chem. Soc.*, 123 (2001) 12798-12801.
- [67] T.W. Smith, D. Wychick, *J. Phys. Chem.*, 84 (1980) 1621-1629.
- [68] M. Tadić, V. Kusigerski, D. Marković, M. Panjan, I. Milošević, V. Spasojević, *J. Alloys Compd.*, 525 (2012) 28-33.
- [69] C. Cannas, D. Gatteschi, A. Musinu, G. Piccaluga, C. Sangregorio, *J. Phys. Chem. B*, 102 (1998) 7721-7726.
- [70] G. Ennas, A. Musinu, G. Piccaluga, D. Zedda, D. Gatteschi, C. Sangregorio, J.L. Stanger, G. Concas, G. Spano, *Chem. Mater.*, 10 (1998) 495-502.
- [71] L. Durães, B.F.O. Costa, J. Vasques, J. Campos, A. Portugal, *Mater. Lett.*, 59 (2005) 859-863.
- [72] R.J. Joseyphus, K. Shinoda, D. Kodama, B. Jeyadevan, *Mater. Chem. Phys.*, 123 (2010) 487-493.
- [73] W. Cai, J. Wan, *J. Colloid Interface Sci.*, 305 (2007) 366-370.
- [74] G.B. Khomutov, I.V. Bykov, R.V. Gainutdinov, S.P. Gubin, A.Y. Obydenov, S.N. Polyakov, A.L. Tolstikhina, *Colloids Surf., A*, 198 (2002) 347-358.
- [75] R. Alexandrescu, I. Morjan, I. Voicu, F. Dumitrache, L. Albu, I. Soare, G. Prodan, *Appl. Surf. Sci.*, 248 (2005) 138-146.
- [76] F. Dumitrache, I. Morjan, R. Alexandrescu, V. Ciupina, G. Prodan, I. Voicu, C. Fleaca, L. Albu, M. Savoiu, I. Sandu, E. Popovici, I. Soare, *Appl. Surf. Sci.*, 247 (2005) 25-31.
- [77] R. Abu Mukh-Qasem, A. Gedanken, *J. Colloid Interface Sci.*, 284 (2005) 489-494.
- [78] J. Pinkas, V. Reichlova, R. Zboril, Z. Moravec, P. Bezdicka, J. Matejkova, *Ultrason. Sonochem.*, 15 (2008) 257-264.
- [79] A. Abedini, A.R. Daud, M.A.A. Hamid, N.K. Othman, E. Saion, *Nanoscale Res. Lett.*, 8 (2013).

- [80] Y. Li, Y.N. Kim, E.J. Lee, W.P. Cai, S.O. Cho, *Nucl. Instrum. Methods Phys. Res., Sect. B*, 251 (2006) 425-428.
- [81] V. Cuba, M. Nemeč, T. Gbur, J. John, M. Pospisil, V. Mucka, *Appl. Radiat. Isot.*, 68 (2010) 676-678.
- [82] S. Seino, T. Kinoshita, T. Nakagawa, T. Kojima, R. Taniguchi, S. Okuda, T.A. Yamamoto, *J. Nanopart. Res.*, 10 (2008) 1071-1076.
- [83] J.H. Park, H.W. Kim, H.S. Kang, Y.H. Koo, B.C. Lee, *Mater. Res. Innovations*, 18 (2014) 678-684.
- [84] J.V. Rojas, M.C. Molina Higgins, M. Toro Gonzalez, C.E. Castano, *Appl. Surf. Sci.*, 357, Part B (2015) 2087-2093.
- [85] R. Ferrando, J. Jellinek, R.L. Johnston, *Chem. Rev.*, 108 (2008) 845-910.
- [86] M.-L. Wu, D.-H. Chen, T.-C. Huang, *Langmuir*, 17 (2001) 3877-3883.
- [87] A. Abedini, F. Larki, E. Saion, A. Zakaria, M. Zobir Hussein, *Radiat. Phys. Chem.*, 81 (2012) 1653-1658.
- [88] M. Mirdamadi-Esfahani, M. Mostafavi, B. Keita, L. Nadjo, P. Kooyman, H. Remita, *Gold Bull.*, 43 (2010) 49-56.
- [89] A. Abedini, E. Saion, F. Larki, A. Zakaria, M. Noroozi, N. Soltani, *Int. J. Mol. Sci.*, 13 (2012).
- [90] A. Sárkány, P. Hargittai, O. Geszti, *Colloids Surf., A*, 322 (2008) 124-129.
- [91] Y.N. Rao, D. Banerjee, A. Datta, S.K. Das, R. Guin, A. Saha, *Radiat. Phys. Chem.*, 79 (2010) 1240-1246.
- [92] Q.-m. Liu, T. Yasunami, K. Kuruda, M. Okido, *Transactions of Nonferrous Metals Society of China*, 22 (2012) 2198-2203.
- [93] S.P. Ramnani, J. Biswal, S. Sabharwal, *Radiat. Phys. Chem.*, 76 (2007) 1290-1294.
- [94] R. Chadha, R. Sharma, N. Maiti, A. Ballal, S. Kapoor, *Spectrochim. Acta, Part A*, 150 (2015) 664-670.
- [95] M.Z. Kassae, A. Akhavan, N. Sheikh, R. Beteshobabrud, *Radiat. Phys. Chem.*, 77 (2008) 1074-1078.
- [96] A. Abedini, F. Larki, E.B. Saion, A. Zakaria, M.Z. Hussein, *J. Radioanal. Nucl. Chem.*, 292 (2012) 361-366.
- [97] S.W. Kim, B.J. Kwon, J.H. Park, M.G. Hur, S.D. Yang, H. Jung, *Bull. Korean Chem. Soc.*, 31 (2010) 910-914.
- [98] P.A. Yakabuskie, J.M. Joseph, P. Keech, G.A. Botton, D. Guzonas, J.C. Wren, *Phys. Chem. Chem. Phys.*, 13 (2011) 7167-7175.
- [99] L.M. Alrehaily, J.M. Joseph, M.C. Biesinger, D.A. Guzonas, J.C. Wren, *Phys. Chem. Chem. Phys.*, 15 (2013) 1014-1024.
- [100] L.M. Alrehaily, J.M. Joseph, A.Y. Musa, D.A. Guzonas, J.C. Wren, *Phys. Chem. Chem. Phys.*, 15 (2013) 98-107.

Chapter 3. Experimental Principles and Procedures

This chapter will explain the theoretical basis of all analytical methods used in this study. It will also provide a rationale for the general experimental approach.

3.1. EXPERIMENTAL PRINCIPLES

3.1.1. UV-Vis Spectroscopy

The concentration of iron species present in solution was determined using UV-Vis spectroscopy. This method relies on the electronic transitions of a molecule. This differentiates it from infrared spectroscopy that relies on rotational or vibrational transitions of a molecule. Atomic and molecular orbitals have specific energy differences between them. If the wavelength of incoming light matches this energy difference a photon may be absorbed by the molecule or atom. This behaviour can be exploited qualitatively to determine the composition of a sample, based on absorbance at a specific wavelength, and quantitatively, based on the fraction of incoming light that is absorbed. The absorbance of light by a specific species follows the Beer-Lambert Law,

$$A_{\tilde{\nu}} = \log\left(\frac{I_0}{I}\right) = \varepsilon_{\tilde{\nu}}lc \quad (3.1)$$

where $A_{\tilde{\nu}}$ is the absorbance of the solution at a specific wavelength, I_0 is the intensity of light entering the solution at the specified wavelength, I is the intensity of light exiting the solution, and $\varepsilon_{\tilde{\nu}}$ is the molar extinction coefficient at the specific wavelength, $\tilde{\nu}$, l is the length of the cell containing the solution through which the light passes, and c is the concentration of the solute in the solution. The extinction coefficient is the probability of the solute to absorb light as a function of cell distance at the specified wavelength [1].

The UV-Vis spectra obtained as a function of irradiation time contain at least two overlapping bands in range of 300 to 700 nm. An unirradiated ferric nitrate solution has

one broad absorption band with a peak at 304 nm. The measured UV-Vis spectra were deconvoluted by subtracting a band for Fe(NO₃)₃ from the measured spectra. In this process the peak in the ferric nitrate solution spectrum was scaled to match the peak intensity in the measured spectrum at 304 nm. The result is the series of ‘ferric nitrate’ and ‘ferric-nitrate subtracted’ bands.

Ferric nitrate dissolves and dissociates in aqueous solution and the ferric ion is quickly hydrolyzed [2, 3]:



The nitrate ion does not absorb light at wavelengths > 300 nm, but it has been reported that ferric hydroxides species (Fe(OH)²⁺_(aq) and Fe(OH)⁺_(aq)) have broad UV-vis absorption bands with peak intensities near 300 nm [4, 5]. Various ferric oxides, such as lepidocrocite (γ-FeOOH) and maghemite (γ-Fe₂O₃), also absorb at 290-310 nm, 360-380 nm and 430 nm [6]. The absorption band at 380 nm is absent in the spectrum of the unirradiated ferric nitrate solution. The UV absorption peak at 304 nm is an electronic transition mostly associated with the Fe^{III} – OH bonding, whereas the peak at 380 nm is mostly associated with the spinel metal-oxide bonding (such as the mixed Fe^{II} – O and Fe^{III} – O bonding in magnetite). In this way these absorbances are used as a measure of the systems iron hydration.

Some complications of using this method to directly measure the concentration of Fe³⁺ lie in the scattering of light by the nanoparticles produced during the irradiation of an iron solution. To overcome this, the ferrozine method was used. In this method a disodium salt of 3-(2-pyridyl)-5,6-bis(4-phenylsulfonic acid)-1,2,4-triazine (henceforth known as ferrozine) complexes with Fe²⁺ species in the solution to generate a coloured complex with

a maximum absorbance at 562 nm with a molar extinction coefficient of $27900 \text{ cm}^{-1}\text{M}^{-1}$. Because the solution only shows this colouration within a pH range of 4-9, a buffer solution of ammonia-ammonium acetate was also added. An aliquot of the sample solution is mixed with the ferrozine reagent to complex with the Fe^{2+} in solution and the absorbance of this complex was measured. In order to obtain the Fe^{III} concentration in solution, another aliquot of the solution was mixed with hydroxylamine hydrochloride. This reduces the Fe^{III} species present to Fe^{2+} species. Once this has been completed, the ferrozine reagent was added and the absorbance at 562 nm was measured. This yields the total iron concentration in the solution. The measured $[\text{Fe}^{2+}]$ is then subtracted from the total iron concentration to obtain the $[\text{Fe}^{\text{III}}]$ in the solution. The reducing solution reduces not only the Fe^{3+} dissolved in the solution, but also on any Fe^{III} contained in solid nanoparticles and so these value will be reported as Fe^{III} [7].

3.1.2. Gas Chromatography (GC)

Gas chromatography is an analytical technique that can be used to identify and quantify gas phase species. A gas sample is injected through an inlet port into an inert gas (N_2 in this work). The gas traverses a column internally coated with a stationary phase (a GS GasPro column was used in this work). The separation of gas species in the sample occurs due to their different affinities with the stationary phase. The separation of the species is also influenced by the flow rate of the mobile phase and the temperature of the column. With the same set of chromatograph operating parameters a species will elute off at a consistent time allowing for identification of the species. The signal strength of the species at its retention time is proportional to its concentration in the input gas sample [8].

There are several different options for the outlet gas detector and the option chosen is usually the most sensitive for the target species of interest. A thermal conductivity detector (TCD) measures the differential heat loss while the analyte plus carrier gas is passing a filament versus that of when there is only carrier gas present. For this detector option to be effective the carrier gas must have a substantially different thermal conductivity than the analyte of interest. Nitrogen has a thermal conductivity of $20.6 \text{ mW}\cdot\text{m}^{-1}\text{K}^{-1}$ [9] and this allows precise and accurate measurements of the presence of hydrogen which has a thermal conductivity of $186.6 \text{ mW}\cdot\text{m}^{-1}\text{K}^{-1}$ [9].

To effectively measure the presence of oxygen, an electron capture detector (ECD) was used. An ECD consists of a radioactive source (Ni-63) that emits beta particles. These beta particles ionize the carrier gas producing a current of thermal electrons. This detector takes advantage of oxygen's high electron affinity. Any oxygen present will capture thermal electrons causing a drop in current as it passes through the detector. In these studies, oxygen and hydrogen are the primary gaseous radiolysis products that collect in the headspace of a test vial. Thus both the TCD and ECD were used to determine the concentrations of hydrogen gas and oxygen gas respectively.

3.1.3. pH

The pH of the solution was measured as a function of irradiation time using a probe that consisted of two electrodes. A measuring electrode is made up of a silver/silver chloride electrode immersed in a potassium chloride solution buffered to a neutral pH. A reference electrode is identical in composition to the measuring probe but held at a constant pH of 7. The hydrogen ions in the measuring electrode and in the solution itself migrate

through a permeable interface. This creates a potential difference between the measuring probe and the reference probe. The potential difference is related to the solution pH through calibration with solutions with known pHs.

3.1.4. Fourier Transform Infrared Spectroscopy (FTIR)

Infrared spectroscopy is based on the absorbance of light by internal vibrations of a molecule. For light to be absorbed by the molecule, the vibration must cause a change in the dipole moment of the molecule. Dipole moment changes can be predicted by the symmetry of the molecule. Like electronic states, the vibrational and rotational states have different energies and thus the energy of light which stimulates a change from one state to a higher state will correspond to the energy difference between these states. The vibrational energies are characteristic of a molecule (determined by bond strengths and atomic masses). Hence Fourier transfer infrared spectroscopy is able to reveal details about the symmetry of the molecule and the bonds found within and can be used to qualitatively determine the chemical composition of a sample [10].

In order to obtain a full infrared spectrum in a timely manner, a Fourier transform technique is used. Instead of striking the target with one wavelength of light at a time and scanning the wavelengths until the absorbance of a spectral region is measured, the target is struck with multiple wavelengths of light simultaneously. The different wavelengths of light are periodically blocked and transmitted to the sample as a function of time. This was first accomplished using a Michelson interferometer (Figure 3.1).

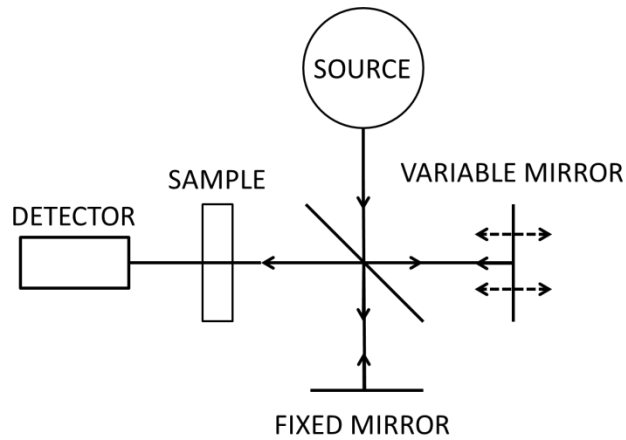


Figure 3.1: A visual representation of a Michelson Interferometer. The beam from the source is split by the mirror in the centre which transmits half of the incident beam to the fixed mirror and reflects half of the incident beam to the variable mirror. These beams both reflect off their respective mirrors and recombine before passing through the sample and into the detector.

More sophisticated devices have been developed, but they function on the same underlying principles. Instead of having the light from a source pass through a monochromator to select the wavelength the light is split into two beams. One beam travels a fixed length, while the other beam travels a length which is varied with time. Both of these beams recombine before passing through the sample, but because their path lengths are different they will interfere with each other. As the path length difference changes the interference will undergo a sinusoidal variation in intensity with path differences equal to integer multiples of the wavelength of light corresponding to total constructive interference. This process happens to all of the light passing through the sample, but because the wavelength varies, the sinusoid (more specifically a cosine function) will differ in frequency. Thus the composition of light passing through the sample is a function of the path difference between two beams. The intensity of light transmitted by the sample is the sum of all the intensities over the range of wavelengths studied, as a function of path

difference. The resulting interferogram is deconvoluted using a Fourier transform algorithm. The Fourier transform deconvolutes a sum of sinusoids into their respective amplitudes which converts the relationship between total transmittance and path difference to one of transmittance and wavelength [11].

3.1.5. Raman Spectroscopy

Raman spectroscopy is used as a qualitative characterization tool. Like infrared spectroscopy its spectrum reveals information about the bonding modes within the analyte molecule. Rather than using direct light absorbance Raman spectroscopy is based on an electronic light absorbance. When a molecule is struck by light it can absorb the energy of this light and be excited to a higher energy electronic state. From this state the molecule may elastically scatter the light which results in the molecule emitting a photon with the same energy as the incoming light (Rayleigh scattering). However the molecule may also relax to its original electronic state, but in a different vibrational and rotational state. This results in the emission of a photon with an energy that is different from the incoming light. If the energy is lower than the incident photon energy, this shift in the frequency of light is called a Stokes shift. If this results in the emission of a photon of higher energy, this shift is called an anti-Stokes shift. These processes are shown schematically in Figure 3.2.

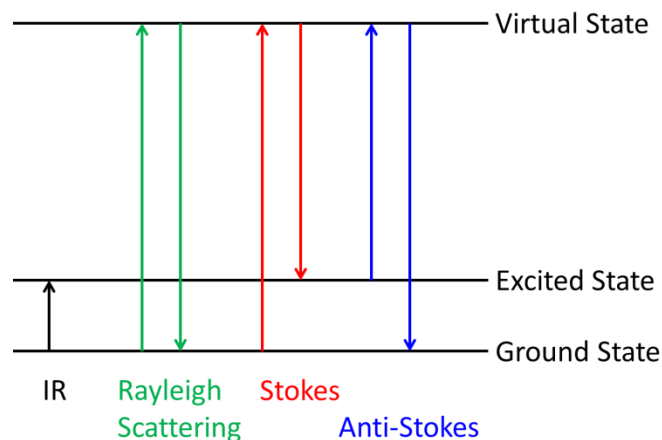


Figure 3.2: A visual illustration of the processes corresponding to IR absorption, Rayleigh scattering, Stokes shifts, and anti-Stokes shifts. Arrows pointing upward correspond to light absorption processes, while those pointing downward correspond to light emitting processes.

Inelastic scattering of light is a weak process compared to Rayleigh scattering and therefore intense incident laser light is used to get an appreciable signal of the inelastic scattering. At room temperature molecules tend to be in their ground vibrational state and so the Stokes shift photons tend to be higher in intensity than anti-Stokes shift photons as a result of the population distribution. For a particular mode, molecules mostly undergo excitations to the energy state immediately adjacent to that of initial state. Therefore, most Raman spectra show the Stokes shift photons that correspond to a change from the ground vibrational state to the first excited state of the bonds contained within a molecule. A molecule must experience a change in polarizability to scatter the light inelastically. Like a dipole moment, polarizability is dependent on the symmetry of the molecule. Because of this selection rule, asymmetric vibrational and rotational modes tend to be Raman active which makes this technique complimentary to FTIR, wherein the active modes tend to be symmetric rather than asymmetric [12].

3.1.6. Transmission Electron Microscopy (TEM)

Transmission electron microscopy is a method of imaging small features in a sample. The maximum resolution obtainable by a source of light is dependent on the wavelength of the incoming light used to image the sample. Shorter wavelengths of light are required for better resolution at higher magnifications. However there is a limit in wavelength of readily available light sources (x-rays). The de Broglie wavelength of an electron is much smaller than that of a conventional light source. Electrons can be used to overcome the limitations of light and obtain very fine images because of their wavelike properties. The wavelength of the incident electrons can be controlled by altering their kinetic energy.

Electrons for TEM are generated by thermal emission of electrons from a heated metal filament. These electrons pass through an electric field to accelerate them to the desired velocity. Electromagnetic lenses focus a narrow beam of electrons onto the sample. The sample must be under vacuum during measurements to ensure sufficient electron flux to yield appreciable results. As the electron beam passes through the sample, the intensity of the beam is attenuated. The degree of attenuation is proportional to the thickness and electron density of the matter which the electron is passing through. The result is ‘darker’ regions that correspond to thicker regions in the sample and or more heavier elements. As a result TEM is powerful tool for obtaining the morphology of a sample and gaining some information on the elemental composition of different regions [13].

3.1.7. X-ray Absorption Near Edge Structure (XANES)

When sufficiently energetic X-rays strike an atom, they can eject a core electron from an atom. In response, an electron from a higher energy orbital drops down to fill the vacancy. The atom will generally emit a photon corresponding to the energy difference between the orbitals. However, the atom may eject another electron to expel the excess energy. These processes are illustrated in Figure 3.3. The total energy of this process is divided between the energy required to ionize the atom and the kinetic energy of the emitted electron. This process is known as the Auger effect. This effect can be exploited to study the composition of a material.

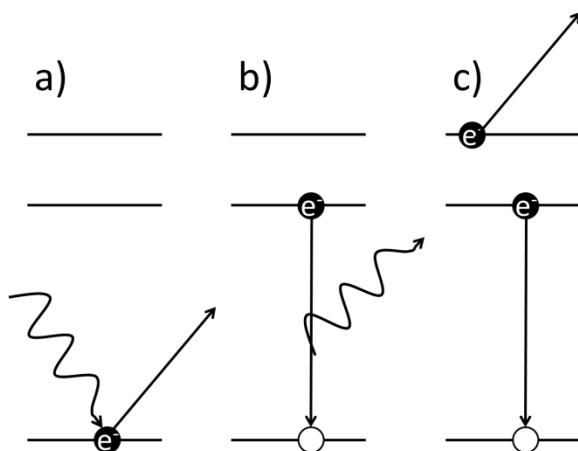


Figure 3.3: A visual representation of a) the photo-ejection of a core level electron, b) a higher level electron dropping down to fill the vacancy and emitting a photon in the process, and c) a higher energy electron dropping down to fill the hole and releasing the extra energy by ejecting another electron.

The typical energy required to ionize a core electron is high and requires soft x-rays to achieve. To obtain a measureable signal it is necessary to use an intense source of light. A synchrotron light source is the ideal source of soft x-rays for these measurements as it is able to generate intense x-ray beams with tunable energy [14].

The XANES spectra (both photon emission and Auger electron emission) display characteristic patterns to allow for fingerprint analysis. An x-ray fluorescence detector is used to capture the intensity of emitted light. A total electron yield detector is used to capture the intensity of Auger electrons generated by this process. Electrons and x-rays differ in their penetration depth through a material. X-rays, like gamma rays, have long penetration depths and thus, the x-ray fluorescence intensity will be characteristic of the bulk phase of a sample. Electrons on the other hand, have short penetration depths. Electrons generated on the surface of the sample will disproportionately reach the detector while those of from the bulk phase will be shielded. Hence, the total electron yield will generate a spectrum characteristic of the surface of a sample [14].

3.1.8. Computer Modelling

FACSIMILE software was used in order to model the water radiolysis products as a function of irradiation time. Water radiolysis involves the production of radical and molecular species that can participate in many reactions [15]. These can be divided into two sets: the processes that lead to the creation of primary radiolysis products and the chemical reactions of these primary radiolysis products. The processes that produce the primary radiolysis products are generally considered to behave as zeroth order reactions that are dependent on the radiolysis yield (or G-value) of the species in question, G_a , the dose rate of the system, D_R , and the density of water, ρ_{H_2O} , (3.3).

$$\left[\frac{d[a]}{dt} \right]_{\text{Radiolysis}} = D_R G_a \rho_{H_2O} \quad (3.3)$$

The chemical reactions can result in the removal or production of a particular species. These reactions tend to follow second order kinetics. There may be multiple reactions

leading to removal or production of a species as shown in equations 3.4 and 3.5 where a, b, c and d refer to species in solution and k_{ab} and k_{cd} are second order rate constants.

$$\left[\frac{d[a]}{dt} \right]_{Removal} = - \sum_b k_{ab}[a][b] \quad (3.4)$$

$$\left[\frac{d[a]}{dt} \right]_{Production} = \sum_{c,d} k_{cd}[c][d] \quad (3.5)$$

Combining all of the reactions together yields the total rate equation for a particular species (equation 3.6).

$$\left[\frac{d[a]}{dt} \right]_{Total} = D_R G_a \rho_{H_2O} + \sum_{c,d} k_{cd}[c][d] - \sum_b k_{ab}[a][b] \quad (3.6)$$

The rate equations for these reactions in a set of stiff differential equations which are impossible to solve analytically but can be addressed numerically using the FACSIMILE software [16]. The program uses all of the possible reactions and their rate constants to calculate the instantaneous rates of these total rate equations for all species at the starting time and applies that rate over a certain amount of time known as the time step. After the time step, the new species concentrations are used to calculate the new instantaneous rate of each reactant. This new instantaneous rate is applied over another time step. This process is repeated until the desired time is reached. The program then produces the evolution of the species in the system as a function of time.

In modelling the kinetic behaviour of a system the relevant temperature relationships are used to adjust the rate constants as a function of temperature following the Arrhenius equation (equation 3.7).

$$k = A e^{-E_a/RT} \quad (3.7)$$

Where k is the rate constant of a specific reaction, A is the pre-exponential factor specific to each reaction, E_a is the activation energy of the reaction, R is the universal gas constant, and T is the temperature. The density of water changes with temperature and this alters radiolysis production of the primary radiolysis products. This is taken into account in modelling a system. The model allows for inferences to be made regarding the dominant processes in the system. As the concentration of certain species accumulates or is diminished, different pathways will govern the behaviour of the system. This helps to understand the formation of different oxide compositions and morphologies.

3.2. EXPERIMENTAL PROCEDURES

3.2.1. Sample Preparation

All solutions were freshly prepared before each experiment with water, purified using a NANOpure Diamond UV ultrapure water system, with a resistivity of 18.2 M Ω ·cm. High-purity ferrous sulfate was obtained from Sigma-Aldrich (purity \geq 99%) and used without further purification. Sulfate is the anion of choice because it is thought to only interact minimally with the radiolysis products and oxide formation. Pure water was deaerated by purging with ultra-high purity argon (impurity 0.001%) for more than one hour before solutions were prepared in an argon-filled glove box (O_2 level $<$ 0.1 vol.%). This was done to prevent premature oxidation of iron by atmospheric oxygen. Solutions containing $Fe^{2+}_{(aq)}$ in the concentration range 0.1 mM to 10 mM were prepared with the pH adjusted using 1 N NaOH or 1 N H_2SO_4 (added dropwise). The solution pH was measured using a pH meter (Mettler Toledo) inside the glove box. Aliquots of 10 mL of a prepared

solution was then transferred into a 20 mL Pyrex vial (Agilent Technologies) and sealed using a PTFE silicon septa. To test the effect of an electron scavenger test vials were purged with 50% nitrous oxide balance argon mixture (Praxair) for fifteen minutes. The solutions in test vials used to study the effect of a hydroxyl radical scavenger had t-butanol added to a concentration in the range of 0.026 – 1 M.

3.2.2. Sample Irradiation

All samples were irradiated using a Co⁶⁰ gamma cell (MDS Nordion, model 220) with a radiation dose rate of approximately 0.8 Gy/s. The cell itself is comprised of a loading chamber, an irradiation chamber, and shielding. The loading chamber is a small compartment that sits above the irradiation chamber. Samples are loaded into this chamber and sealed before the irradiations begin. When the irradiation time starts, the loading chamber is lowered into the irradiation chamber below for a set amount of time. The irradiation chamber lies in the heart of the gamma cell. Arrayed in a circle around the irradiation chamber are pencils of Co⁶⁰ which deliver a uniform dose of radiation to the whole sample. The Co⁶⁰ undergoes spontaneous beta decay to Ni⁶⁰ (reaction 3.8).



The dose rate of the cell was determined using Frick's dosimetry (see section 3.2.2.1 below). The gamma cell is externally shielded using a combination of lead and depleted uranium. The β -particle emitted from the Co decay (with 0.31 MeV) is blocked by the shielding around the sample container and does not reach the test vials.

Room temperature samples were loaded into the gamma cell and the irradiation time started immediately. Samples which were heated were sealed inside of an autoclave

which was put into the loading chamber. Heating was initiated before the samples were lowered into the irradiation chamber. This was done to ensure that nucleation occurred under at least partial heat. The vials reached a temperature of 40 °C and were then lowered into the irradiation chamber. They reached their target temperatures, ranging from 40-80 °C, in less than ten minutes while being irradiated. Heating was promptly stopped when the irradiation stopped. The test vials were cooled to room temperature by running under cool water prior to sample analysis.

3.2.2.1. Fricke Dosimetry

The concentration of water radiolysis products is dependent on the absorbed dose of radiation. The most straightforward way of getting the absorbed dose is to determine it analytically. A Fricke dosimetry process was used for this purpose. The Fricke dosimetry uses a solution of FeSO₄ with a concentration of 1×10⁻³ M and H₂SO₄ added to make the solution acidic. The solution is aerated to ensure oxygen does not limit the reaction. Under these conditions, Fe²⁺ will be quantitatively oxidized to Fe³⁺ by the oxidizing products of water radiolysis (reactions 3.9a – 3.9c).



The rate of oxidation of Fe²⁺ to Fe³⁺ is dictated by the rate of generation of the oxidizing radiolysis products. A known volume of the Fricke solution is placed inside the gamma cell for a fixed amount of time (60 s). The amount of Fe³⁺ produced is determined by measuring the absorbance at 304 nm of the solution upon removal and the dose rate can be calculated from equation 3.10.

$$Dose \left(\frac{Gy}{s} \right) = \frac{9.648 * 10^6 * \Delta A_{304}}{\varepsilon_{304} l \rho G(products) * t} \quad (3.10)$$

where ΔA_{304} is the difference in absorbance of the irradiated sample of solution and a sample which was not irradiated, ε_{304} is the molar extinction coefficient of Fe^{3+} at 304 nm, l is the length of the UV-Vis cuvette which the light passes through, ρ is the density of the dosimeter solution (1.024 g/cm^3), $G(products)$ is the known dose required to generate the species necessary to produce the observed $[Fe^{3+}_{(aq)}]$ (15.5), t is time, and 9.648×10^6 is a proportionality constant [17, 18].

3.2.3. Sample Analysis

Samples were removed from test vials at specific times ranging from one minute to five hours. Once samples were removed from radiation and cooled to room temperature (where applicable), the samples were analyzed by using the methods described above. First, ten millilitre samples of the gas in the headspace of the vial were extracted using an air-tight syringe with Luer lock and analyzed by gas chromatography (6890 N Agilent Technologies) to determine the oxygen and hydrogen content using a GS-GasPro column (J&W Scientific). Nitrogen was used as the carrier gas at a flow rate of 4.6 ml/min. The TCD detector used for H_2 analysis was calibrated using certified gas mixtures of H_2 in Ar (0.1 %, 1%, 3% and 5%) (Praxair). The ECD detector was calibrated using different concentrations of O_2 (2%, 5%, 10% and 35%) in argon. These concentrations of gas in the head space were used to determine the concentrations of gas dissolved in the aqueous phase using Henry's Law [19].

Aliquots of the liquid from a test vial had their UV-Vis spectra measured using a UV spectrophotometer (Biologic Science Instruments) equipped with a diode array

detector. Aliquots were also diluted and analyzed using the ferrozine method to determine the iron speciation in the sample. The pH of the test vial liquid was measured next. Copper grids for transmission electron microscopy were dipped into the samples and allowed to dry in air. The TEM imaging was done using a Philips CM10 Transmission Electron Microscope operating at 80 keV. Test vials with the longest irradiation times for a given set of initial conditions (five hours for room temperature studies and one hour for heated studies) were centrifuged and the solid collected was deposited onto glass slides. These slides were dried in air. The dried samples had their Raman, FTIR, XRD and XANES spectra measured to determine their composition. The Raman scattering measurements were carried out using a Renishaw model 2000 Raman Spectrometer with a laser excitation wavelength of 633 nm. The FTIR measurements were performed using a Bruker Vertex 70v FT-IR spectrometer. XANES was performed using the Soft X-Ray Microcharacterization Beam (SXRMB) at the Canadian Light Source.

3.3. REFERENCES

- [1] H.-H. Perkampus, *UV-VIS spectroscopy and its applications*, Springer-Verlag, New York, Berlin, (1992).
- [2] D. Fu, P.G. Keech, X.L. Sun, J.C. Wren, *Phys. Chem. Chem. Phys.*, 13 (2011) 18523-18529.
- [3] C.F. Baes, R.E. Mesmer, *The Hydrolysis of cations*, Wiley, New York, (1976).
- [4] R.J. Knight, R.N. Sylva, *Journal of Inorganic and Nuclear Chemistry*, 37 (1975) 779-783.
- [5] B.C. Faust, J. Hoigné, *Atmos. Environ. Part A*, 24 (1990) 79-89.
- [6] D.M. Sherman, D. Waite, *Amer. Mineral.*, 70 (1985) 1262-1269.
- [7] L.L. Stookey, *Anal. Chem.*, 42 (1970) 779-781.
- [8] D.A. Skoog, F.J. Holler, S.R. Crouch, *Principles of instrumental analysis*, 6th Ed., Thomson Brooks/Cole, Belmont, CA, (2007).
- [9] CRC Handbook of Chemistry and Physics: 61st ed. CRC Press: Boca Raton, FL, 1980.
- [10] B. Stuart, *Infrared spectroscopy: fundamentals and applications*, J. Wiley, Hoboken, NJ, Chichester, West Sussex, England, (2004).

- [11] B.C. Smith, *Fundamentals of Fourier transform infrared spectroscopy*, CRC Press, Boca Raton, FL, (2011).
- [12] E. Smith, G. Dent, *Modern Raman spectroscopy: a practical approach*, J. Wiley, Hoboken, NJ, Chichester, UK, (2005).
- [13] R.F. Egerton, I. Books24x, *Physical principles of electron microscopy: an introduction to TEM, SEM, and AEM*, Springer Science+Business Media, New York, (2005).
- [14] S. Mobilio, F. Boscherini, C. Meneghini, SpringerLink, *Synchrotron Radiation: Basics, Methods and Applications*, Springer Berlin Heidelberg, Berlin, Heidelberg, (2015).
- [15] G.V. Buxton, C.L. Greenstock, W.P. Helman, A.B. Ross, *J. Phys. Chem. Ref. Data*, 17 (1988) 513-886.
- [16] FACSIMILE Kinetic Modelling Software, in, MCPA Software Ltd., 2003.
- [17] J.W.T. Spinks, R.J. Woods, *An introduction to radiation chemistry*, Wiley, New York, (1990).
- [18] J. Hefhe, *J. Nucl. Sci. Technol.*, 37 (2000) 402-405.
- [19] R. Sander, *Atmos. Chem. Phys.*, 15 (2015) 4399-4981.

Chapter 4. The Effect of Ferrous Ion Concentration on the Kinetics of Radiation-Induced Iron-Oxide Nanoparticle Formation and Growth

4.1. INTRODUCTION

This chapter examines the effect of initial Fe^{2+} concentration on the kinetics of particle formation, size, morphology, and final composition of the particles formed under gamma irradiation. An increased Fe^{2+} concentration impacts the rates of nucleation and growth. The final particle characteristics are controlled by the position of the redox equilibrium between Fe^{II} species and Fe^{III} species. An increased concentration of Fe^{2+} in the bulk solution shifts the redox potential of the system and thus influences the final particles size.

This work limits its study to the effect of initial Fe^{2+} concentrations in the range of 0.1 to 10 mM at an initial pH of 6. This range lies below the solubility limit of Fe^{II} species, but above the solubility limit of Fe^{III} species. A similar study is reported in Chapter 5 which analyzes the impact of changing the initial pH of the system.

4.2. EXPERIMENTAL

All solutions were freshly prepared before each experiment with water, purified using a NANOpure Diamond UV ultrapure water system, with a resistivity of 18.2 $\text{M}\Omega\text{-cm}$. High-purity ferrous sulfate was obtained from Sigma-Aldrich (purity $\geq 99\%$) and used without further purification. The water was deaerated by purging with ultra-high purity argon (impurity 0.001%) for more than one hour before solutions were prepared in an

argon-filled glove box (O_2 level < 0.1 vol.%). Solutions containing Fe^{2+} in the concentration range 0.1 mM to 10 mM were prepared with the pH adjusted to 6.0 using 1 M NaOH (added dropwise). The solution pH was measured using a pH meter (Mettler Toledo) inside the glove box. The prepared solution, 10 mL in volume, was then transferred into a 20-mL Pyrex vial (Agilent Technologies) leaving 10 mL headspace, and the vial was sealed using a PTFE silicon septum. The vials were irradiated in a ^{60}Co gamma cell (MDS Nordion) as discussed in detail in Chapter 3. The gamma source provided a uniform absorption dose rate of 0.8 Gy/s in the water samples at the time of this study.

Following irradiation, the headspace gases were extracted using an air-tight syringe with Luer lock and analyzed for oxygen and hydrogen by the gas chromatography equipped with a thermal conductivity detector and electron capture detector. The solutions were analyzed using two different methods, UV-Vis absorbance spectroscopic analysis and ferrozine colorimetry analysis. The UV-Vis absorption spectrum of an irradiated solution showed two broad overlapping bands with peak intensities at 304 nm and 380 nm. The deconvolution of the spectrum to the two absorption bands is described in Section 4.3.1. All of the spectrophotometric measurements were carried out using a diode array detector (BioLogic Science Instruments).

The ferrous and ferric concentrations in the solution were determined using the ferrozine method [1, 2]. In this method ferrozine was added to an aliquot of the test solution. The ferrozine reacts with Fe^{2+} to form a coloured complex that absorbs light at 563 nm with a molar extinction coefficient of $27900\text{ M}^{-1}\cdot\text{cm}^{-1}$ [2]. To a second aliquot of test solution hydroxylamine hydrochloride ($1.4\text{ mol}\cdot\text{dm}^{-3}$ in concentration) was added. This additive reduced all Fe^{III} (ferric ions either as dissolved, adsorbed or solid species) present to Fe^{2+} .

Ferrozine was then added to this solution to determine the Fe^{2+} concentration which now corresponds to the total iron concentration of the solution. The $[\text{Fe}^{\text{III}}]$ was determined from the difference in $[\text{Fe}^{2+}]$ measured before and after the reduction of Fe^{III} to Fe^{2+} . A calibration curve for $[\text{Fe}^{2+}]$ was obtained by adding ferrozine to solutions prepared with FeSO_4 concentrations ranging from 0.05 mM to 0.005 M. The possibility that the water radiolysis product H_2O_2 could affect the ferrozine analysis was investigated. Hydrogen peroxide can oxidize ferrous species to ferric species, but this should not affect the determination of the total iron content (i.e., the sum of $[\text{Fe}^{2+}]$ and $[\text{Fe}^{\text{III}}]$ determined using the ferrozine method). We tested this by adding H_2O_2 to a ferrous solution. The total iron content was found to be the same as the initial Fe^{2+} content.

The evolution of particle morphology was investigated by transmission electron microscopy (TEM). For the TEM imaging, the particles were collected by dipping a carbon-coated copper grid into the irradiated test solution and drying the sample grid in air. The TEM images were obtained with the electron microscope operated at 80 keV (Philips Electronics).

The chemical compositions of the oxide particles were analyzed by Fourier transform infrared (FTIR), Raman and X-ray absorption near edge structure (XANES) spectroscopy. For the spectroscopic analyses the solution was centrifuged, and the collected particles were placed onto a glass slide, and allowed to air dry. For FTIR spectroscopy the dried particles were incorporated into the KBr pellet and the spectra of the particles were taken using a Bruker model Vertex 70v with Fourier transformation (Bruker) in the 4000 to 400 cm^{-1} frequency range. The Raman spectroscopy was performed using a Renishaw model 2000 Raman Spectrometer with a laser excitation wavelength of

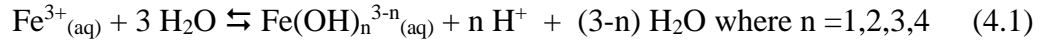
633 nm. The XANES spectroscopy was performed using the Soft X-Ray Microcharacterization Beam (SXRMB) at the Canadian Light Source (CLS). The resulting fluorescent X-ray emission spectra were collected for bulk sample analysis, while the ejected electron spectra were collected for surface composition analysis. The light source was set in the range of 7100 – 7180 eV which corresponds to the range over which the characteristic Fe K-edge absorption occurs.

4.3. RESULTS

4.3.1. Analysis of the UV-Vis Absorption Spectrum

Figure 4.1 shows the UV-Vis spectra obtained as a function of irradiation time for 0.5 mM $[\text{Fe}^{2+}]_0$. These spectra appear to contain at least two overlapping bands in range of 300 to 700 nm. An unirradiated ferric nitrate solution has one broad absorption band with a peak at 304 nm. The measured UV-Vis spectra were deconvoluted by subtracting a band for $\text{Fe}(\text{NO}_3)_3$ from the measured spectra. In this process the peak in the ferric nitrate solution spectrum was scaled to match the peak intensity in the measured spectrum at 304 nm. The result is the series of ‘ferric nitrate’ and ‘ferric-nitrate subtracted’ bands shown in Figure 4.1b. The time dependences of the peak absorbances at 304 nm and 380 nm of the deconvoluted bands are shown in Figure 4.1c. Both absorbances increase with time while their ratio remains nearly constant. The rates of increases in both absorbances slow down with time, eventually approaching zero when the absorbances reach near steady state values after ~ 100 min. These observations indicate that the two absorption bands correspond to two electronic transitions of a same species.

Ferric nitrate dissolves and dissociates in aqueous solution and the ferric ion is quickly hydrolyzed [3, 4]:



The nitrate ion does not absorb light at wavelengths > 300 nm, but it has been reported that ferric hydroxides species ($\text{Fe}(\text{OH})^{2+}_{(\text{aq})}$ and $\text{Fe}(\text{OH})_2^+_{(\text{aq})}$) have broad UV-vis absorption bands with peak intensities near 300 nm [5, 6]. Various ferric oxyhydroxides/oxides, such as lepidocrocite ($\gamma\text{-FeOOH}$) and maghemite ($\gamma\text{-Fe}_2\text{O}_3$), also absorb at 290-310 nm, 360-380 nm and 430 nm [7]. The absorption band at 380 nm is absent in the spectrum of the unirradiated ferric nitrate solution. Thus, we have tentatively assigned the UV absorption peak at 304 nm to an electronic transition mostly associated with the $\text{Fe}^{\text{III}} - \text{OH}$ bonding, whereas the peak at 380 nm to that mostly associated with $\text{Fe}^{\text{III}} - \text{O}$ bonding. The ratio of the peak absorbances provide qualitative information on the extent of dehydration or conversion from hydroxide to spinel oxide.

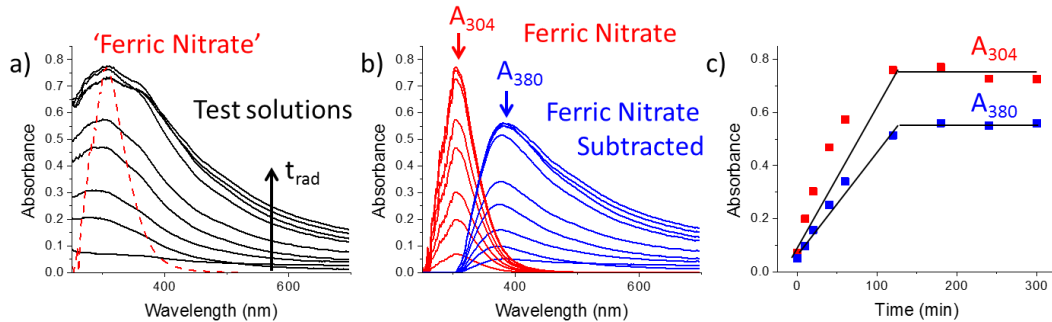


Figure 4.1: (a) UV-Vis absorption spectra of solutions containing 0.5 mM $[\text{Fe}^{2+}]_0$ irradiated for different durations, and the spectrum of ferric nitrate solution, (b) the corresponding deconvoluted spectra of ‘ferric nitrate’ and ferric-nitrate subtracted’, and (c) the absorbances at 304 and 380 nm as a function of irradiation time.

4.3.2. Kinetics of Iron-Oxide Particle Formation and Growth

The kinetics of iron-oxide nanoparticle formation and growth under γ -radiation were followed by TEM imaging of the particles and by performing four different sets of solution and gas analyses as a function of time. The solution and gas analyses include $[\text{Fe}^{2+}]$ and $[\text{Fe}^{\text{III}}]$ in solution by the ferrozine method, UV-vis absorbances of solution at 304 nm and 380 nm (A_{304} and A_{380}), H_2 concentration in the headspace ($[\text{H}_{2(\text{g})}]$), and solution pH. The effect of initial ferrous ion concentration ($[\text{Fe}^{2+}]_0$) on the kinetics were studied in the concentration range of 0.1 mM to 10 mM in deaerated water with its pH initially adjusted to 6.0. Some examples of the solution and gas analysis results are shown in Figure 4.2.

For a given $[\text{Fe}^{2+}]_0$ the time dependent behaviours of solution and gas analyses collectively show three distinct kinetic stages. The durations of these stages are indicated on tops of the kinetic plots. The characteristics of the kinetic stages are:

Stage 1 has a very short duration. Over this short stage the total concentration of the Fe^{2+} species that is converted to the Fe^{III} species ($-\Delta[\text{Fe}^{2+}]$ or $\Delta[\text{Fe}^{\text{III}}]$) is $\sim 0.15 \pm 0.05$ mM, nearly independent of $[\text{Fe}^{2+}]_0$. The changes, $-\Delta[\text{Fe}^{2+}]$ and $\Delta[\text{Fe}^{\text{III}}]$, accompany increases in both A_{304} and A_{380} , while $[\text{H}_{2(\text{g})}]$ is negligible. The pH shows the most rapid change in this stage compared to later stages, decreasing to a value below 3.5 with a slightly lower value in a lower $[\text{Fe}^{2+}]_0$ solution. The transition between Stage 1 and Stage 2 coincides with the small increase in pH before it decreases again.

In Stage 2, the rate of conversion from Fe^{2+} to Fe^{III} ($-\Delta[\text{Fe}^{2+}]/\text{dt}$ or $\Delta[\text{Fe}^{\text{III}}]/\text{dt}$) is nearly proportional to $[\text{Fe}^{2+}]_0$. The absorbances at 304 nm and 380 nm both increase logarithmically, but their ratio remains nearly constant with time for a given $[\text{Fe}^{2+}]_0$. The

absorbance at 380 nm increases to a final steady-state value at the end of Stage 2 of ~ 0.5 at the end of Stage 2 and this final absorbance at 380 nm is nearly independent of $[\text{Fe}^{2+}]_0$. The rate of production of $\text{H}_{2(\text{g})}$ ($\Delta[\text{H}_{2(\text{g})}]/\text{dt}$) in Stage 2 is now measurable. The pH fluctuates near 3.0 and 3.5 initially but decreases at later times in Stage 2. The duration of Stage 2 decreases with $[\text{Fe}^{2+}]_0$.

In Stage 3, the net conversion of Fe^{2+} to Fe^{III} is very slow and consequently $[\text{Fe}^{2+}]$ and $[\text{Fe}^{\text{III}}]$ are near steady state. The rate of conversion has a small dependence on $[\text{Fe}^{2+}]_0$, it is slightly higher at a higher $[\text{Fe}^{2+}]_0$. In Stage 3, A_{380} is constant with time while A_{304} increases. The A_{304} increases at a faster rate in a higher $[\text{Fe}^{2+}]_0$ solution. The $\text{H}_{2(\text{g})}$ production in Stage 3 is negligible when $[\text{Fe}^{2+}]_0$ is less than 5 mM. The pH does not change with time in Stage 3.

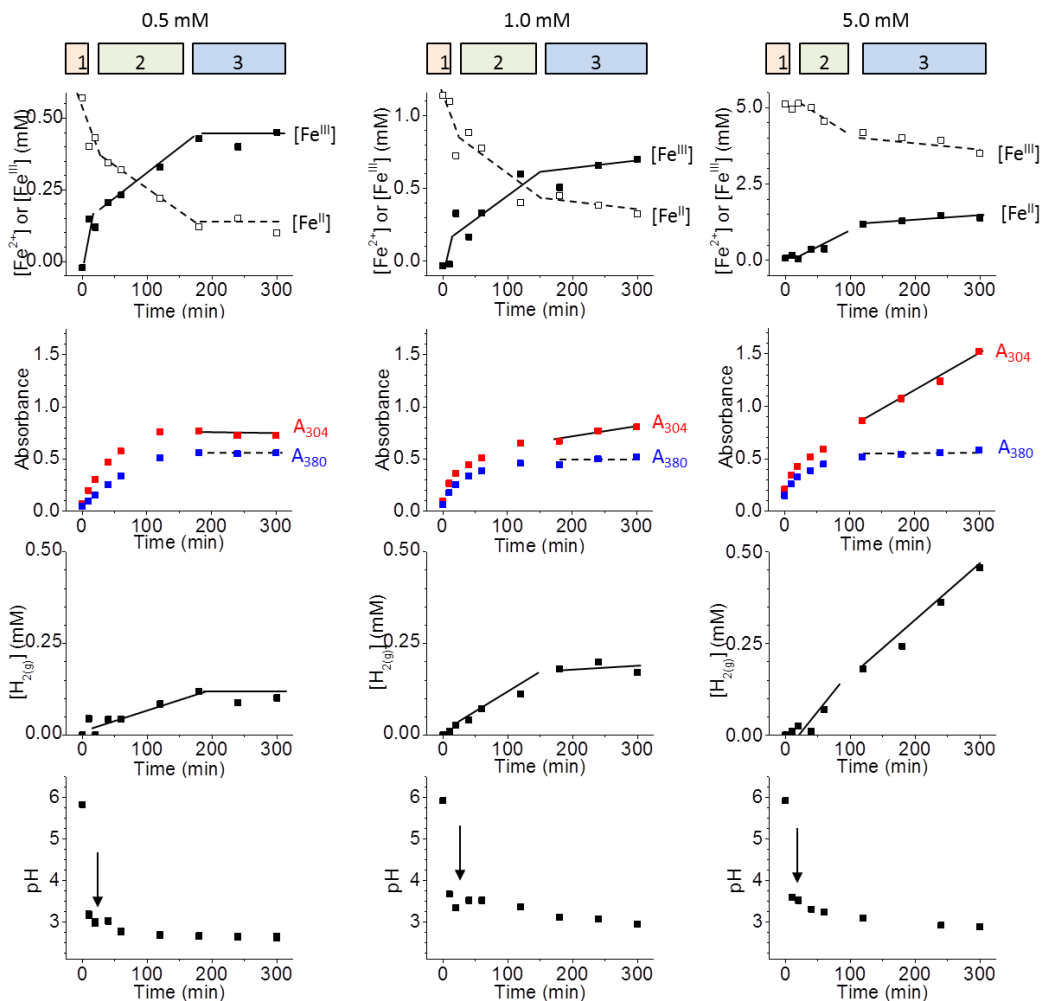


Figure 4.2: Kinetic behaviours observed during radiolytic conversion of dissolved ferrous ions to iron oxide/hydroxide nanoparticles for three different $[\text{Fe}^{2+}]_0$, (a) 0.5 mM, (b) 1 mM and (c) 5 mM, at pH 6.0. Four different sets of kinetic data are shown from the top to bottom: $[\text{Fe}^{2+}]$ and $[\text{Fe}^{\text{III}}]$ determined by the ferrozine method, the UV-vis absorbances at 304 nm and 380 nm, $[\text{H}_{2(\text{g})}]$ in the headspace and pH. The three kinetics stages are indicated by the bars at the top of each data set. The lines are drawn to guide the eyes.

The TEM images of the particles formed in 0.5 mM $[\text{Fe}^{2+}]_0$ solutions as a function of irradiation time are presented in Figure 4.3. The changes in particle morphology also show different kinetic stages. The TEM images of the particles formed in Stage 1 show two areas with different shades. The darker areas contain well-defined, denser particles of 20-30 nm in size. The lighter areas are made up of less dense particles which appear to

have aggregated during collection on the TEM grids. Initially the well-defined, denser particles are nearly absent and only the light particles are present. The number of the denser particles increases with increasing irradiation time in Stage 1. In Stage 2, the lighter particles are nearly absent, indicating that the lighter particles are growing into denser particles. In Stage 3, the small denser particles appear to have undergone coarsening or Ostwald ripening to form even larger dendritic particles of 80-100 nm in size. Interestingly, the dendritic particles as well as the small denser particles formed at a given time have very narrow size distributions.

The XANES, Raman, and FTIR spectroscopic analyses of the particles formed after 5-h irradiation are described in more details in Section 4.3.4. The spectroscopic analyses suggest that the particles are magnetite or mixed Fe^{II}/Fe^{III} particles with the outer layers in varying degrees of hydrated or hydroxide forms.

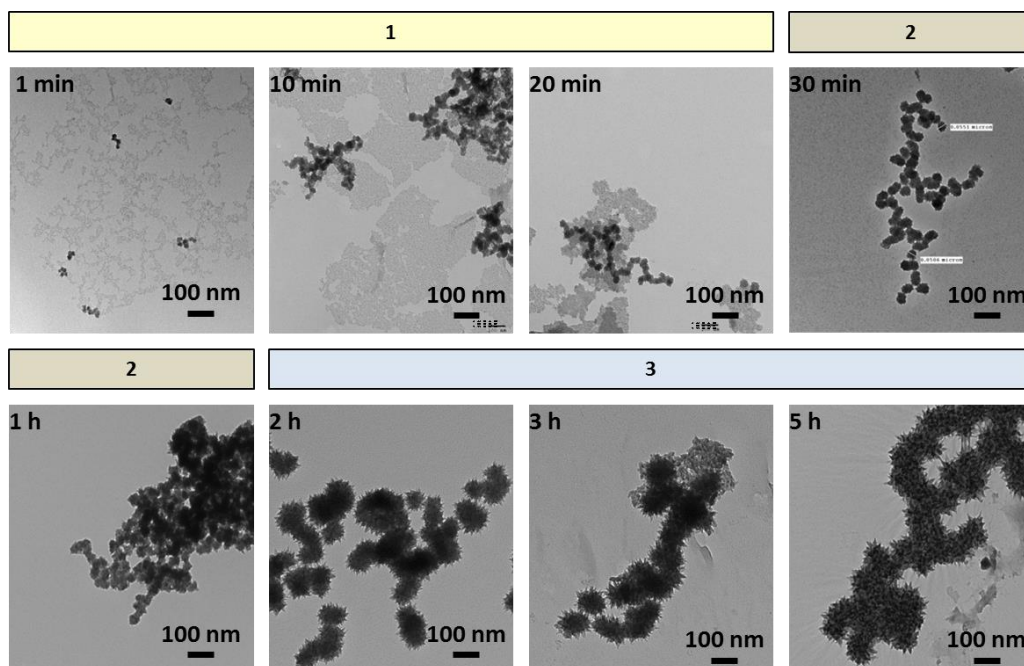


Figure 4.3: TEM images of the particles formed by γ -irradiation of 0.5 mM $[\text{Fe}^{2+}]_0$ solutions at pH 6.0 as a function of irradiation time (indicated on the images). The bars above the images indicate the kinetic stages.

The reaction mechanism that can explain the observed kinetic behaviour is described here briefly. The main process involved in Stage 1 is attributed to solution-phase oxidation of soluble ferrous ions to less soluble ferric ions by radiolytically-produced $\bullet\text{OH}$, followed by hydrolysis of ferric ions, which triggers co-precipitation of Fe^{II} and Fe^{III} species as mixed hydroxide nucleate particles. In Stage 2 particle nucleation continues, but the dominant process is the continued adsorption of Fe^{2+} onto existing particles followed by oxidation of the adsorbed $\text{Fe}^{2+}_{(\text{ad})}$ to $\text{Fe}^{3+}_{(\text{ad})}$ on the particle surfaces. As formed, $\text{Fe}^{3+}_{(\text{ad})}$ is incorporated with $\text{Fe}^{2+}_{(\text{ad})}$ into the solid oxide phase, growing as mixed $\text{Fe}^{\text{II}}/\text{Fe}^{\text{III}}$ (spinel) oxide particles. In Stage 3, negligible net oxidation of ferrous to ferric species occurs, but Ostwald ripening or coarsening of the particles by continuous dissolution and precipitation (see further discussion in Section 4.3.5).

4.3.3. Effect of $[\text{Fe}^{2+}]_0$ on Reaction Yields at 5-h Irradiation at $0.8 \text{ Gy}\cdot\text{s}^{-1}$

The TEM images of the particles formed after 5-h irradiation of solutions containing different $[\text{Fe}^{2+}]_0$ are presented in Figure 4.4. They show that the average size of the dendritic particles increases with $[\text{Fe}^{2+}]_0$, but for a given $[\text{Fe}^{2+}]_0$ the particles have a narrow size distribution. The average and the standard deviation of the size of the particles determined from the TEM images are listed in Table 4.1.

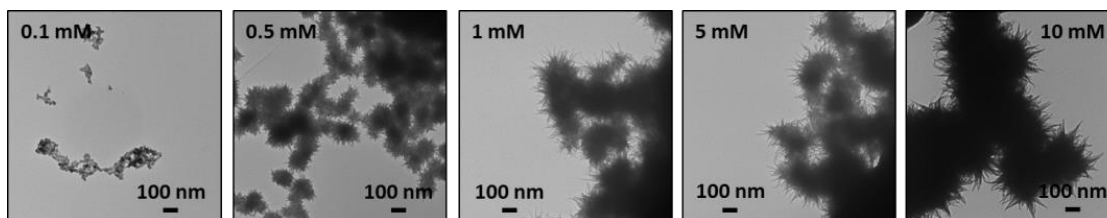


Figure 4.4: TEM images of the particles collected after 5-h irradiation at $0.8 \text{ Gy}\cdot\text{s}^{-1}$ of deaerated solutions containing different $[\text{Fe}^{2+}]_0$.

Table 4.1: Averages and standard deviations of the sizes of particles formed after 5-h irradiation of solutions containing different $[\text{Fe}^{2+}]_0$ at $3.0 \text{ kGy}\cdot\text{h}^{-1}$.

Concentration (mM)	Sample Population Size ^a	Average Diameter ^a (nm)	Standard Deviation ^a (nm)
0.1	6	23	2
0.5	9	94	6
1	8	140	30
5	4	180	20
10	5	300	40

^a Determined from TEM images.

The yields after 5-h irradiation of $[\text{Fe}^{\text{III}}]_{5\text{h}}$ and $[\text{H}_{2(\text{g})}]_{5\text{h}}$, and the average diameter of the particles ($d_{5\text{h}}$) are presented as a function of $[\text{Fe}^{2+}]_0$ in log-log plots in Figure 4.5. The

slope of 1.0 in the $\log [\text{Fe}^{\text{III}}]_{5\text{h}}$ vs $\log [\text{Fe}^{2+}]_0$ plot means that the product yield is linearly proportional to the initial reactant concentration. The line representing the slope of 1.0 is also shown in Figure 4.5a. In the $[\text{Fe}^{2+}]_0$ range below 1 mM, the data for $[\text{Fe}^{\text{III}}]_{5\text{h}}$ closely follows the line of slope of 1.0, but shows progressively more deviation from the slope as $[\text{Fe}^{2+}]_0$ increases. This agrees with the kinetic data for $[\text{Fe}^{\text{III}}]_{5\text{h}}$ presented in Figure 4.2, which show that each kinetic stage, particularly Stage 2, has a different oxidation rate and duration depending on $[\text{Fe}^{2+}]_0$. On the other hand, the data for $[\text{H}_{2(\text{g})}]_{5\text{h}}$ closely follow the slope of $\frac{1}{2}$ in the $[\text{Fe}^{2+}]_0$ range < 1 mM, indicating that one H_2 molecule is produced for every oxidation of two Fe^{2+} atoms to two Fe^{III} atoms, maintaining the overall redox balance. The line representing the slope of $\frac{1}{2}$ is also shown in Figure 4.5b. The data for $d_{5\text{h}}$ closely follow the slope of $\frac{1}{3}$ except for the lowest $[\text{Fe}^{2+}]_0$ case. A slope of $\frac{1}{3}$ in the $\log d_{5\text{h}}$ vs $\log [\text{Fe}^{2+}]_0$ plot is expected if the average volume of the particles ($\propto d_{5\text{h}}^3$) increases linearly with $[\text{Fe}^{2+}]_0$. The observed dependences of the yields, $[\text{Fe}^{\text{III}}]_{5\text{h}}$, $[\text{H}_{2(\text{g})}]_{5\text{h}}$ and $d_{5\text{h}}$, on $[\text{Fe}^{2+}]_0$ are consistent with the kinetic data.

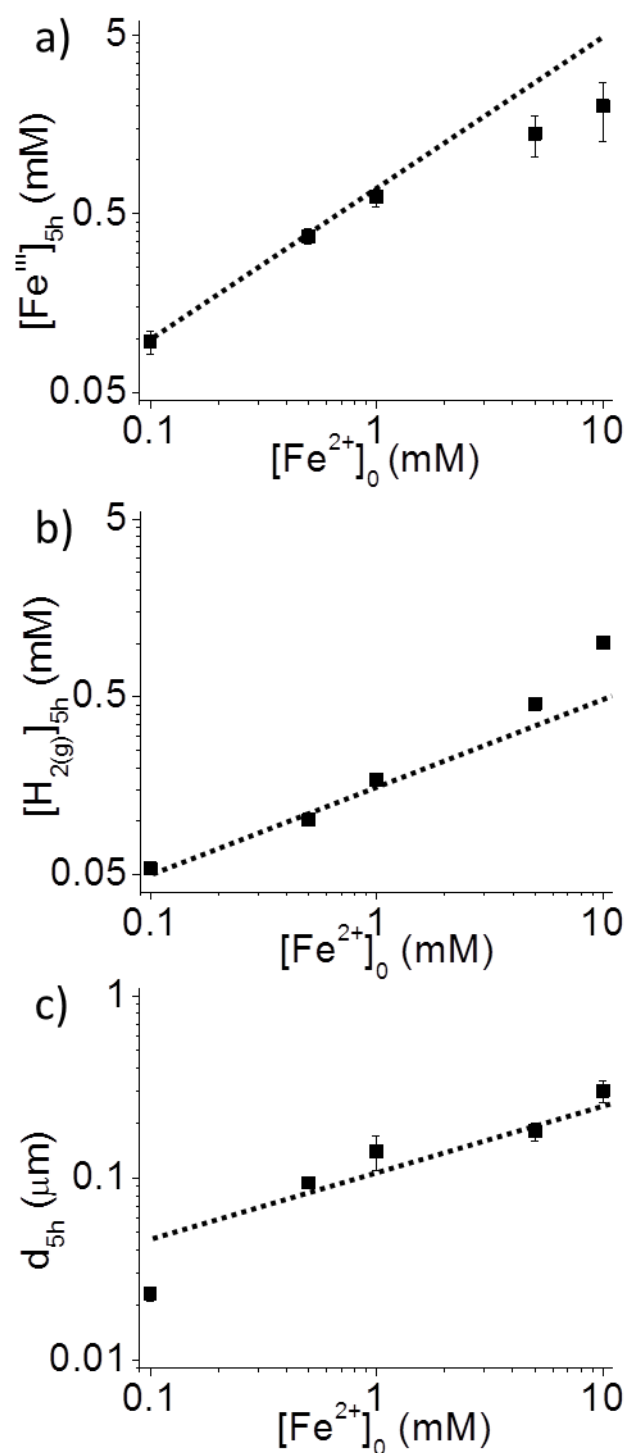


Figure 4.5: Product yields after 5-h irradiation of deaerated solutions containing different $[\text{Fe}^{2+}]_0$ at an initial pH of 6.0, (a) $[\text{Fe}^{\text{III}}]$, (b) $[\text{H}_{2(\text{g})}]$ in the headspace and (c) the average size of particles. The lines representing slopes of 1.0, 1/2 and 1/3 are also shown in respective plots.

4.3.4. Spectroscopic Characterization of the Particles

The iron-oxide particles formed after 5-h irradiation were examined by XANES, Raman and FTIR spectroscopy to obtain the chemical and phase composition of the particles. For XANES, both the Fe K-edge total electron yield (TEY) and the X-ray fluorescence yield (FLY) spectra were taken. The FLY XANES is more sensitive to the bulk composition while the TEY is more sensitive to the surface composition. The TEY and FLY spectra of the particles formed in solutions containing different $[\text{Fe}^{2+}]_0$ are shown in Figure 4.6. Also shown in the figure are the reference spectra of standard magnetite (Fe_3O_4) particles. The reference XANES spectra of other iron-oxide particles have been reported [8, 9] and have been used to characterize the particles.

The XANES spectra of the particles formed in different $[\text{Fe}^{2+}]_0$ solutions all show similar spectroscopic features, most closely resembling those of magnetite. Compared to the reference magnetite spectrum, the TEY spectra of the particles show broader features that could be attributed to poor crystallinity or aggregation of small crystal particles. The pre-edge peak in the TEY spectra of the particles also coincides with that of Fe_3O_4 . The FLY spectra of the particles are similar to that of Fe_3O_4 , consistent with the TEY results. The FLY spectra also nearly identical to the TEY spectra, indicating that there's no significant difference between the surface and bulk phases of the particles or, if present, a different surface layer is very thin.

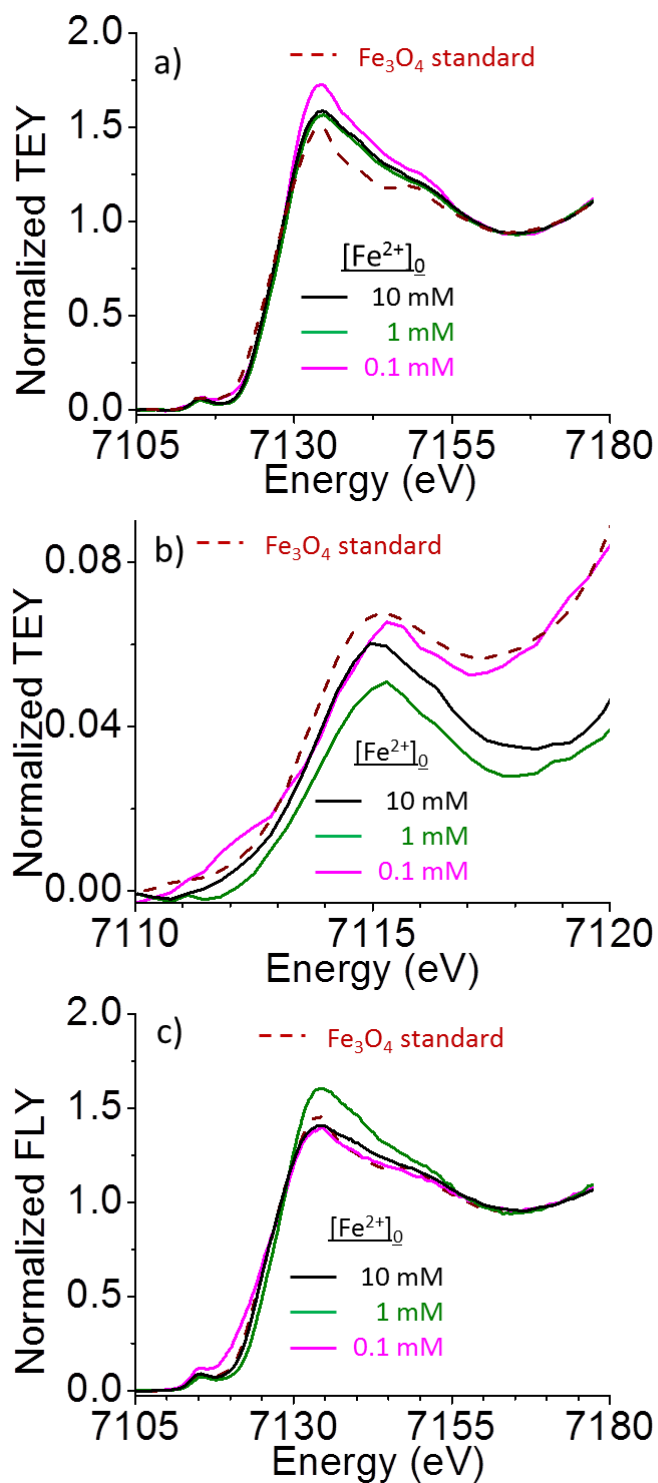


Figure 4.6: XANES Fe K-edge spectra of the particles formed after 5-h irradiation of solutions containing different $[\text{Fe}^{2+}]_0$ at an initial pH of 6.0, (a) the full TEY, (b) the pre-edge TEY, (c) the FLY. The XANES spectra of a standard magnetite sample are also shown for comparison.

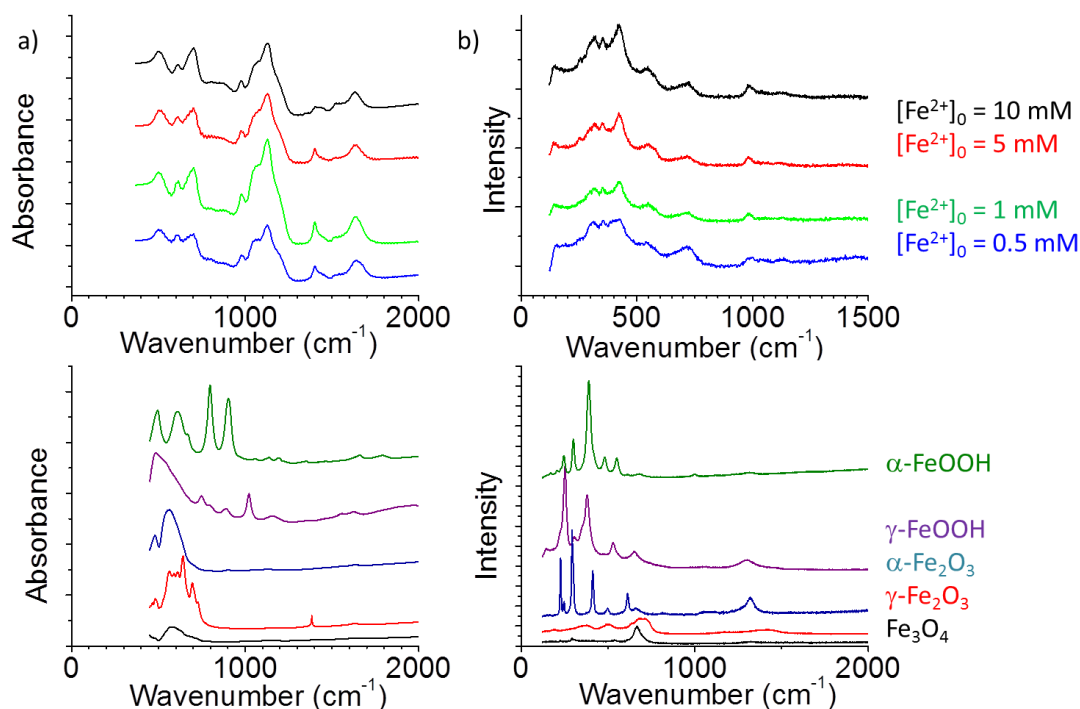


Figure 4.7: (a) Fourier transform infrared spectra and (b) Raman spectra of the particles formed after 5-h irradiation of deaerated solutions containing different $[\text{Fe}^{2+}]_0$ at an initial pH of 6. The reference spectra taken from standard powder samples are shown

The FTIR and Raman spectra of the particles are presented in Figure 4.7 along with the reference spectra taken with standard powder samples of different iron oxides. The FTIR and Raman spectra of the particles formed in different $[\text{Fe}^{2+}]_0$ solutions are nearly the same, the combination of the FTIR and Raman spectra indicates that the rotational-vibrational frequencies of the oxide particles are $\sim 300, 350, 420, 500, 600$ and 700 cm^{-1} . The large peaks at wavenumbers $> 1000 \text{ cm}^{-1}$ in the FTIR are attributed to those belong to adsorbed sulfate [10]. The spectral intensities of the vibrational modes at 500 and 700 cm^{-1} that are both IR and Raman active most closely resemble those of magnetite. The Raman peaks at wavenumbers smaller than 420 cm^{-1} are present as the main peaks in the reference spectra of $\alpha\text{-FeOOH}$ and $\gamma\text{-FeOOH}$. Green rust II, which is an $\text{Fe}^{\text{II}}/\text{Fe}^{\text{III}}$ mixed hydroxide

with SO_4^{2-} occupying some of the anionic positions within the hydroxide structure, also has a main Raman peak at 420 cm^{-1} [11]. Hence, we have tentatively assigned the Raman peaks at wavenumbers below 420 cm^{-1} to a vibrational mode associated with the $\text{Fe}^{\text{III}} - \text{OH}$ (or $-\text{OOH}$) bond, and the FTIR and Raman peaks at 700 cm^{-1} to a vibrational mode of Fe_3O_4 . The Raman intensity at 420 cm^{-1} relative to that of 700 cm^{-1} increases slightly with $[\text{Fe}^{2+}]_0$.

Based on the XANES, FTIR, and Raman analyses the particles can be best characterized as mostly Fe_3O_4 (magnetite) in the core while their outer surfaces are in varying hydrated and hydrolyzed forms, i.e., mixed $\text{Fe}^{\text{II}}/\text{Fe}^{\text{III}}$ oxyhydroxide and hydroxide:



The fraction of the hydrated or hydroxide layer on the particles increases with $[\text{Fe}^{2+}]_0$. The formation of magnetite in the core with a hydroxide/oxyhydroxide outer layer is consistent with the observed time evolutions of A_{304} and A_{380} (Figure 4.1 and Figure 4.2). In Section 4.3.1 we attributed the two UV-Vis absorption bands centred at 304 and 380 nm to an electronic transition associated mostly of the $\text{Fe}^{\text{III}} - \text{OH}$ bonding and that of the spinel $\text{Fe}^{\text{II}}/\text{Fe}^{\text{III}} - \text{O}$ bonding, respectively. The ratio of the absorbances is nearly constant in Stage 1 and Stage 2, but increases with time in Stage 3. These time-dependent behaviours are consistent with particles that grow as magnetite in the core and an outer layer of $\text{Fe}^{\text{II}}/\text{Fe}^{\text{III}}$ that is hydrated and hydrolysed and increases in thickness with increasing $[\text{Fe}^{2+}]_0$.

4.3.5. Radiolysis Kinetics Calculations

Gamma-radiation decomposes water molecules and forms primary radiolysis products homogeneously in a bulk solution phase (see section 2.2.2). The time from the

collision of a γ -photon and a water molecule to the homogenous distribution of the primary radiolysis products is nearly instantaneous (on a chemical reaction time scale). Once homogeneously distributed in the solution the primary radiolysis products can undergo aqueous chemical reactions. To determine the time dependence of the concentrations of the key oxidants and reductants that are important for oxide particle formation we have performed the kinetic calculations of the radiolysis products under continuous irradiation conditions.

We used a γ -radiolysis kinetic model that solves the rate equations of strongly coupled processes for the calculations. The processes that are considered in this model include (a) the primary radiolysis process that produces radiolysis product i and (b) the chemical reactions of i with itself and other chemical species, j , including other radiolysis products, and dissolved chemical or reactive surface species present in the corresponding water phase. For modeling the radiolysis product concentrations on the time scale of solute oxidation and oxide particle formation, modeling of the detailed kinetics of the primary radiolysis processes occurring within ~ 100 ns is not necessary. Thus, the production rates of water decomposition products by primary radiolysis processes are simplified by assuming that a radiolysis product, i , is created at a rate proportional to its g -value (g_i), D_R , and the density of the medium, ρ_{H_2O} [12-14].

The primary radiolysis products rapidly undergo chemical reactions with each other, water and its acid and base ions, and solute species present. About 45 elementary reactions involving more than 10 chemical species are considered in the model for water species alone. The rate equation for the concentration of species, i , is set up in the model as follows:

$$\left. \frac{d[i]_t}{dt} \right|_{net} \approx 10^{-6} \cdot G_i \cdot D_R \cdot \rho_{H_2O} - \left(\sum_j k_{ij} \cdot [j]_t \right) \cdot [i]_t \quad (4.3)$$

where $[i]$ is the concentration of species, i , in units of M ($\text{mol} \cdot \text{dm}^{-3}$), k_{ij} represents the rate constant of the chemical reaction between species i and j . The complex kinetics involving strongly coupled reactions are solved using commercially available software FACSIMILE [13]. The model and its kinetic predictions have been validated against experimental data obtained under a wide range of solution conditions [12, 15].

Results obtained using the γ -radiolysis model are presented in Figure 4.8. In deaerated solutions free of iron species the concentrations of the water primary radiolysis products at very short times after the start of irradiation (< 1 ms) increase linearly with time (i.e., the slope of the log-log plot is 1). These times are too short for solution reactions to occur at a substantial rate and the production of a primary radiolysis product at shorter times can be approximated by the radiation dose rate and the species g-value, e.g.

$$\frac{d[\bullet\text{OH}]_t}{dt} \approx G_{\bullet\text{OH}} \cdot D_R \cdot \rho_{H_2O} \quad (4.4a)$$

$$[\bullet\text{OH}]_t \approx G_{\bullet\text{OH}} \cdot D_R \cdot \rho_{H_2O} \cdot t \quad (4.4b)$$

where $G_{\bullet\text{OH}}$ is the g-value for $\bullet\text{OH}$, D_R is the radiation dose rate in units of $\text{Gy} \cdot \text{s}^{-1}$ ($\text{J} \cdot \text{kg}^{-1} \cdot \text{s}^{-1}$), and ρ_{H_2O} is the density of water ($\text{kg} \cdot \text{L}^{-1}$).

The more chemically reactive a radiolysis product is, the faster its concentration reaches steady state. For example, the concentration of the hydroxyl radical, $\bullet\text{OH}$, reaches steady state within about 10 ms in pure water, while the less reactive molecular species such as $[\text{H}_2\text{O}_2]$ reach steady state at longer times. At times < 1 s, the concentrations of the radiolysis products (except for $\bullet e_{aq}^-$) are not affected by pH (results not shown) because

their main removal reactions do not involve H^+ or OH^- . At longer times, secondary radiolysis products such as H_2O_2 start influencing the radiolysis kinetics. The steady-state concentrations reached at longer times (> 100 s) depend on the production rates of the secondary products. More detailed discussion on the kinetics of continuous γ -radiolysis of water can be found elsewhere [12-14, 16].

In modelling the radiolysis of solutions initially containing Fe^{2+} two additional iron reactions were included in the model:



The main objective of these calculations was to determine the rate of net radiolytic production of Fe^{3+} in solution and the effect of $[Fe^{2+}]_0$ on that rate. These results provide information on how fast the irradiated solutions become supersaturated in Fe^{3+} species and hence the time at which particle nucleation can begin. The slower oxidation of Fe^{2+} by H_2O_2 does not contribute significantly to the production of Fe^{3+} at early times because the $[H_2O_2]$ is low then and hence was not included in these calculations. Hydrolysis reactions of the iron species, their precipitation as hydroxide particulates and further oxidation of the solid particles were also not included in these calculations.

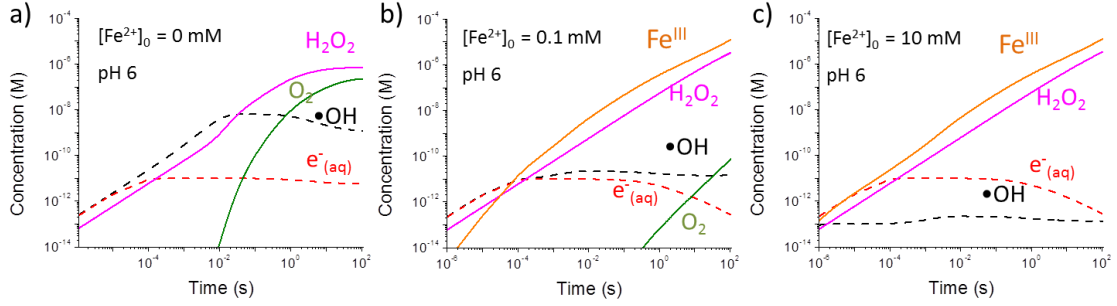


Figure 4.8: Calculated concentrations of radiolysis products as a function of irradiation time for deaerated solutions containing different $[\text{Fe}^{2+}]_0$ at an initial pH of 6.0. Only the key radiolysis products critical to the formation of the iron nanoparticles are illustrated here, though many others are present.

Because reaction (4.5) occurs faster with increasing $[\text{Fe}^{2+}]_0$, $[\bullet\text{OH}]$ reaches a steady-state value faster, within 0.1 ms to 1 μs when $[\text{Fe}^{2+}]_0$ increases from 0.1 mM to 10 mM. On the other hand, reaction (4.6) cannot compete with the reaction of H^+ for $\bullet\text{e}_{\text{aq}}^-$ especially at low pHs, and hence $[\text{Fe}^{2+}]_0$ has a negligible effect on $[\bullet\text{e}_{\text{aq}}^-]$ at short times (< 0.1 s). Under these conditions $[\bullet\text{OH}]_{\text{SS}}$ and $[\text{Fe}^{3+}]_t$ can be approximated as:

$$[\bullet\text{OH}]_{\text{SS}} \approx \frac{G_{\bullet\text{OH}} \cdot D_R \cdot \rho_{\text{H}_2\text{O}}}{k_{4.5} \cdot [\text{Fe}^{2+}]_0} \quad (4.7)$$

$$-\frac{d[\text{Fe}^{2+}]_t}{dt} = \frac{d[\text{Fe}^{3+}]_t}{dt} \approx k_{4.5} \cdot [\bullet\text{OH}] \cdot [\text{Fe}^{2+}]_0 \approx G_{\bullet\text{OH}} \cdot D_R \cdot \rho_{\text{H}_2\text{O}} \quad (4.8)$$

$$[\text{Fe}^{3+}]_t \approx G_{\bullet\text{OH}} \cdot D_R \cdot \rho_{\text{H}_2\text{O}} \cdot t \quad (4.9)$$

The approximated analytical solution (4.9) predicts that (except for very short times) $[\text{Fe}^{3+}]_t$ would increase linearly with time at the same rate as the rate of primary radiolysis production of $\bullet\text{OH}$. This rate is $\sim 0.22 \mu\text{M}\cdot\text{s}^{-1}$ at the studied dose rate of $0.8 \text{ Gy}\cdot\text{s}^{-1}$, independent of $[\text{Fe}^{2+}]_0$. The computational calculations yielded the same results, nearly the same rate of increase in $[\text{Fe}^{3+}]_t$ at times longer than 0.1 ms independent of $[\text{Fe}^{2+}]_0$.

The model calculation analysis indicates that the radiolytic production of $\bullet\text{OH}$ controls the rate of production of Fe^{3+} in the solution phase over a short irradiation period and that this rate will be independent of $[\text{Fe}^{2+}]_0$.

4.4. DISCUSSION

The formation and growth of metal-oxide particles from dissolved metal ions is a complex process that involves many elementary steps including (1) the production or supply of oxide-particle constituent atoms, metal cations and oxygen or hydroxide anions, (2) hydrolysis of metal cations, (3) particle nucleation, (4) diffusion to and adsorption of the particle constituent atoms on the surface of a growing particle and (5) oxide lattice formation.

For iron-oxide/hydroxide particles, one of the main particle constituent atoms is Fe^{III} . (Ferrous oxides/hydroxides cannot form stable nanoparticles under normal solution environments). The production of Fe^{III} can be accomplished by oxidizing soluble ferrous ions, with the oxidation being accomplished by an added chemical oxidant or by a radiolytically produced oxidant. Homogeneous solution oxidation of ferrous to ferric ions by a chemical oxidant at room temperature is rather slow and consequently the particle nucleation is difficult to control. Thus, many common routes for making iron-oxide nanoparticles start with ferric ions in solution. In this case particle nucleation can be accomplished by changing the solvation properties of the solution (e.g., by changing pH or temperature) to promote the precipitation of ferric ions [3, 17, 18]. The alternative explored here is radiolytic oxidation of ferrous ions. The kinetics of iron-oxide nanoparticle

formation and growth driven by γ -radiation occur in three distinct stages. The main processes in these three stages are schematically shown in Figure 4.9.

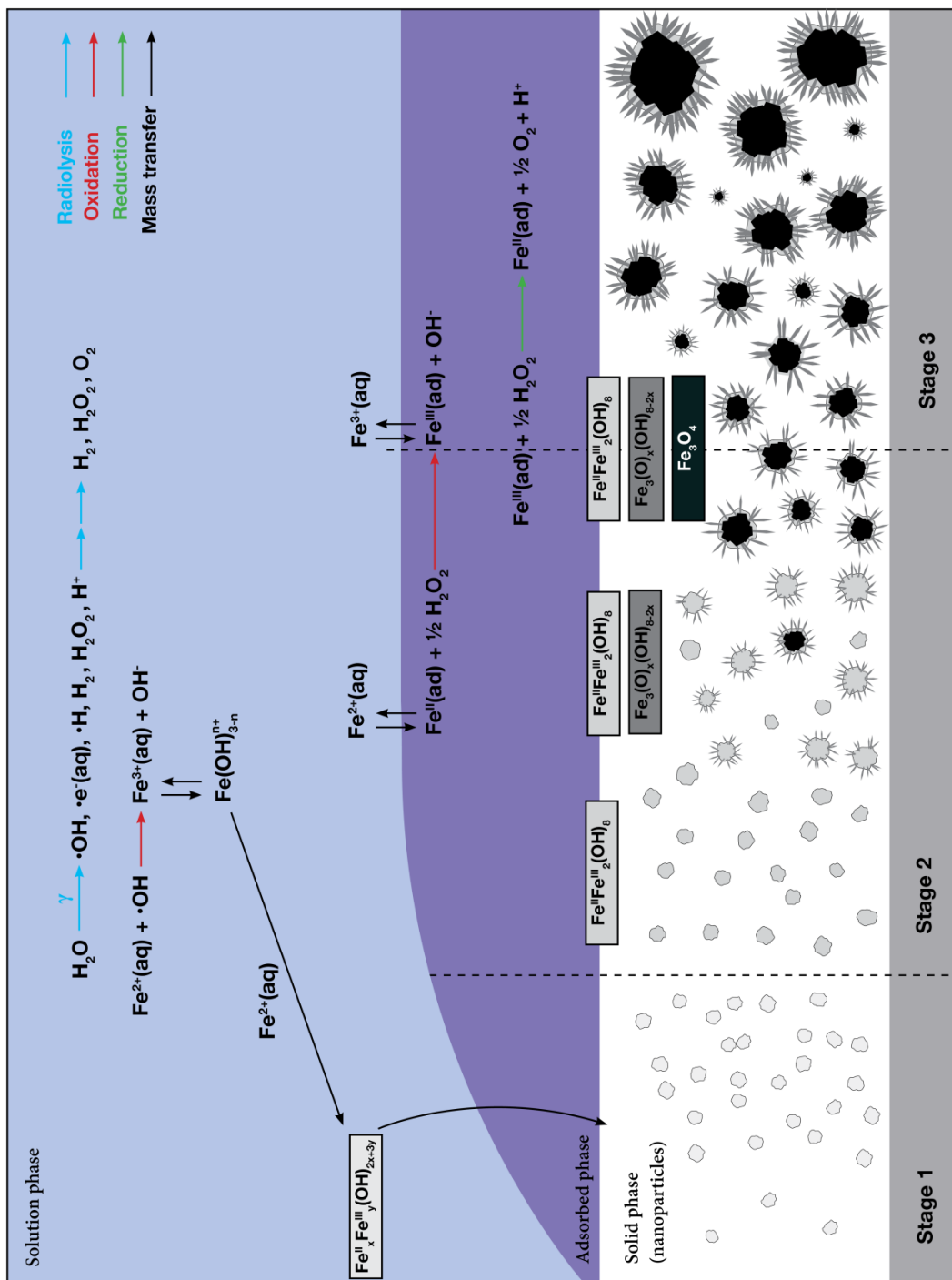
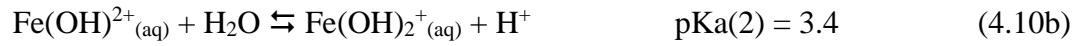
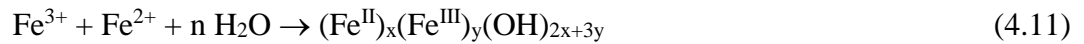


Figure 4.9: Schematic of the main processes occurring in different kinetic stages to form mixed Fe^{II}/Fe^{III} nanoparticles.

Stage 1 involves the aqueous-phase oxidation of Fe^{2+} to Fe^{3+} by radiolytically-produced $\bullet\text{OH}$ (reaction 4.5), followed by hydrolysis of Fe^{3+} (reactions 4.10a to 4.10d) [19]:



The formation of the Fe^{III} hydroxide species triggers co-precipitation of Fe^{II} and Fe^{III} species as mixed hydroxide nucleate particles:



where Fe^{3+} represents all of hydrated ferric species ($\text{Fe}^{3+}_{(\text{aq})}$, $\text{Fe}(\text{OH})^{2+}_{(\text{aq})}$, $\text{Fe}(\text{OH})_2^{+}_{(\text{aq})}$, and $\text{Fe}(\text{OH})_3^{-}_{(\text{aq})}$) and Fe^{2+} represents all of hydrated ferrous species ($\text{Fe}^{2+}_{(\text{aq})}$, $\text{Fe}(\text{OH})^{+}_{(\text{aq})}$, and $\text{Fe}(\text{OH})_2^{0}_{(\text{aq})}$). In a pH range between 3.0 and 6.0 the predominant form of ferric species is $\text{Fe}(\text{OH})^{2+}_{(\text{aq})}$ and/or $\text{Fe}(\text{OH})_2^{+}_{(\text{aq})}$ [4, 19].

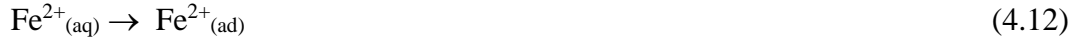
The water radiolysis calculations (Figure 4.8) predict that the rate of radiolytic production of Fe^{3+} will be linearly proportional to the radiation dose rate but independent of $[\text{Fe}^{2+}]_0$. This rate is calculated to be $\sim 0.24 \mu\text{M}\cdot\text{s}^{-1}$ at the studied dose rate of $0.8 \text{ Gy}\cdot\text{s}^{-1}$. At this rate the concentration of ferric ions quickly (in less than 10 ms) reaches its saturation limit ($\sim 4.0 \times 10^{-12} \text{ M}$ at pH 6.0 [20]) under all of the conditions studied.

The ferric ions are quickly hydrolyzed (reaction 4.10). This hydrolysis releases a proton and this process is responsible for the pH drop seen in Stage 1. The overall production of Fe^{III} during Stage 1 is $\sim 0.15 \text{ mM}$ (Figure 4.8). The proton production associated with this amount of Fe^{III} is sufficient to lower the solution pH from 6.0 to ~ 3.8

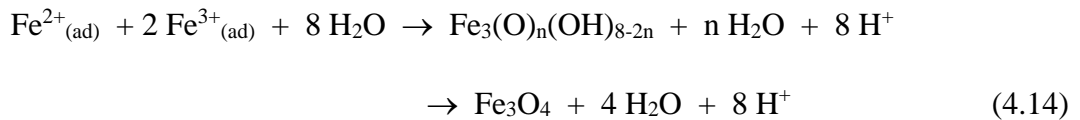
or 3.5 before the system reaches the hydrolysis equilibria. This is consistent with the observed pH change shown in Figure 4.2.

As the Fe^{III} hydroxide species are formed, they can condense by polymerization of Fe_x(OH)_y^{3x-y} [4], which triggers co-precipitation of Fe²⁺ and Fe³⁺ species as mixed hydroxide nucleate particles (process 4.11). Compared to oxidation by a chemical additive, the radiolytic oxidation promotes faster and more uniform particle nucleation because of the rapid, homogenous and constant production of the aggressive oxidant (•OH). As nucleates are formed the main oxidation mechanism changes and the reaction kinetics moves to Stage 2.

Stage 2 mainly involves the adsorption of ferrous ions on the particles formed in Stage 1 (process 4.12), followed by surface oxidation of Fe²⁺_(ad) to Fe³⁺_(ad) by H₂O₂ (reaction 4.13):



The adsorbed Fe²⁺_(ad) and Fe³⁺_(ad) are then incorporated into the growing oxide lattice:



A surface redox reaction typically has a lower activation energy than the corresponding solution reaction and hydrogen peroxide is known to be a significant redox active species [21]. Thus, a less oxidizing species than •OH can contribute more effectively to the oxidation of adsorbed species. In irradiated water this species is H₂O₂. There is very little H₂O₂ present when irradiation is initiated, but the concentration of this species quickly rises to a steady state level that is much higher than that of the •OH that is present. As a result,

oxidation of Fe^{2+} by $\bullet\text{OH}$, either in solution or on a particle surface, is not significant compared to the rate of surface oxidation by H_2O_2 in Stage 2.

The overall iron oxidation kinetics in Stage 2 are controlled by the rate of the surface oxidation of $\text{Fe}^{2+}_{(\text{ad})}$. This rate depends on two processes that occur in series, processes (4.12) and (4.13). The rate of adsorption (process 4.12) depends on the adsorption surface area (A) and $[\text{Fe}^{2+}]_t$ while the rate of oxidation (reaction 4.13) depends on $[\text{Fe}^{2+}_{(\text{ad})}]_t$ and $[\text{H}_2\text{O}_2]_t$. The rate of the two processes in series is controlled by the slower of the two processes. In this case the slower process is the mass transport limited process (4.12). This can explain the observed linear dependence of the net rate of oxidation of Fe^{2+} to Fe^{III} on $[\text{Fe}^{2+}]_0$ in Stage 2 (see Figure 4.2).

The combination of mass transport processes and reactions 4.12 to 4.14 that occur in Stage 2 do not induce significant changes in the proton concentration in solution. This is consistent with the negligible changes in pH observed for Stage 2 (Figure 4.2). The net effect of consumption of radiolytically produced oxidants during the oxidation of Fe^{2+} to Fe^{III} is a decrease in the rates of the reactions of those oxidants with H_2 produced by the water radiolysis. Hence, there is an increase in the production of $\text{H}_{2(\text{g})}$ in Stage 2 (again see Figure 4.2).

With time the $[\text{Fe}^{2+}]_t$ in solution decreases, slowing the rates of surface oxidation of $\text{Fe}^{2+}_{(\text{ad})}$ to $\text{Fe}^{3+}_{(\text{ad})}$ (reaction 4.13) and mixed oxide formation (reaction 4.14). In addition, as $\text{Fe}^{3+}_{(\text{ad})}$ accumulates, the back reduction of $\text{Fe}^{3+}_{(\text{ad})}$ to $\text{Fe}^{2+}_{(\text{ad})}$ by a radiolytic reductant becomes a significant process. The combined effect of these changes is a gradual decrease in rate of oxidation with time. Although the number of particles formed in Stage 1 is nearly independent of $[\text{Fe}^{2+}]_0$, the particles grow faster and the overall particle surface area

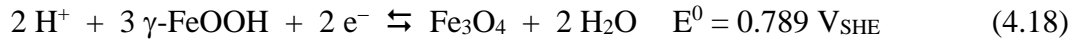
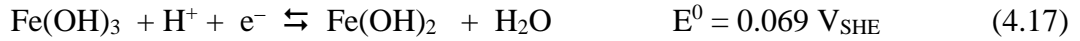
increases faster with more Fe^{2+} in the solution. As a result, Stage 3 is reached faster and the duration of Stage 2 is shorter in a solution with a higher $[\text{Fe}^{2+}]_0$.

Stage 3 mainly involves cyclic Fe^{II} and Fe^{III} redox reactions with a small or negligible net oxidation rate while the particles undergo coarsening or agglomeration. Hence, the $[\text{Fe}^{\text{III}}]$ does not change significantly with time (Figure 4.2) while some particles continue to grow larger (Figure 4.3).

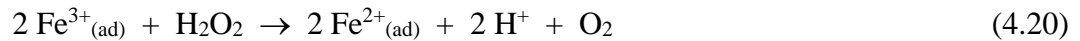
Although the net rate of Fe^{2+} to Fe^{III} oxidation is zero the redox system is dynamic, powered by a continuous radiation flux. In particular, radiolytically-produced H_2O_2 can act as an oxidant for Fe^{II} and as a reductant for Fe^{III} . The standard redox potentials for H_2O_2 reduction to OH^- and its oxidation to O_2 are known [20]:



The standard redox potentials for various Fe^{II} and Fe^{III} redox pairs are also well established [20]. For example:



Thus, depending on the surface activities of $\text{Fe}^{2+}_{(\text{ad})}$ and $\text{Fe}^{3+}_{(\text{ad})}$, $[\text{H}_2\text{O}_2]$, $[\text{O}_2]$ and pH the iron redox system can establish a catalytic cycle such as,



While the redox cycle continues the ferrous and ferric ions also continuously desorb and adsorb on particles and are in dynamic equilibrium as well:





Agglomeration or coarsening of particles occurs through the continuous dissolution-reprecipitation of particle constituent atoms because larger particles are in general energetically more stable than smaller particles, known as Ostwald ripening [22]. In Stage 3, the rates of the forward and reverse reactions of these equilibria are high in the presence of radiation and this will accelerate the Ostwald ripening process. The rates of the redox reactions (4.19) and (4.20) are constant with time under continuous irradiation and this leads to a narrow size distribution of the particles formed in Stage 3.

4.5. CONCLUSION

Magnetite nanoparticles were formed by γ -radiolysis of solutions initially containing different concentrations of FeSO_4 without any other chemical additives. The particles formed in a given $[\text{Fe}^{2+}]_0$ solution had a narrow size distribution, while the average size increased with $[\text{Fe}^{2+}]_0$. Five-hour irradiation at $0.8 \text{ kGy}\cdot\text{s}^{-1}$ produced particles with average size ranging from $23 \pm 2 \text{ nm}$ to $300 \pm 40 \text{ nm}$ when $[\text{Fe}^{2+}]_0$ changed from 0.1 mM to a 10 mM .

The kinetics of γ -radiation-induced formation and growth of magnetite nanoparticles from dissolved ferrous ions were investigated by simultaneously analyzing $[\text{H}_2(\text{g})]$ in the headspace, the $[\text{Fe}^{2+}]$ and $[\text{Fe}^{\text{III}}]$ dispersed in solution, the UV-Vis absorbances at 304 nm and 380 nm and the pH of solution, and examining the particles by TEM imaging and various spectroscopic analyses. The effect of the $[\text{Fe}^{2+}]_0$ on the kinetics was also determined. For a given $[\text{Fe}^{2+}]_0$ the time dependent measured parameters collectively show three distinct stages of iron oxidation kinetics. The $[\text{Fe}^{2+}]_0$ affects the oxidation kinetics of

the different stages differently and hence, the oxidation yields and the size of particles formed after 5-h irradiation.

A reaction mechanism that is consistent with the observations is proposed. The main processes that control the kinetics in Stage 1 are the oxidation of Fe^{2+} to Fe^{3+} in the solution phase by radiolytically-produced $\bullet\text{OH}$, followed by hydrolysis of Fe^{3+} to form Fe^{III} hydroxide species. The formation of less soluble Fe^{III} hydroxides triggers co-precipitation of Fe^{II} and Fe^{III} species as mixed hydroxide nucleate particles. In Stage 2, the dominant process is the adsorption of ferrous ions on the existing particles, followed by surface oxidation to the $\text{Fe}^{2+}_{(\text{ad})}$ to $\text{Fe}^{3+}_{(\text{ad})}$. The $\text{Fe}^{2+}_{(\text{ad})}$ and $\text{Fe}^{3+}_{(\text{ad})}$ are then incorporated into the growing particle oxide lattice. In this stage surface reactions with radiolytically-produced H_2O_2 control the net oxidation rate. Stage 3 involves a redox cycle between Fe^{II} and Fe^{III} driven by reduction and oxidation by H_2O_2 . This results in negligible net oxidation but coarsening of particles.

The initial ferrous ion concentration has a negligible effect on the radiolytic oxidation of Fe^{2+} to Fe^{3+} in solution in Stage 1, but it does increase the rate of surface oxidation on growing particles in Stage 2. Thus, the final oxidation yield of Fe^{III} increases approximately linearly with the $[\text{Fe}^{2+}]_0$ and this results in the average size of the final particles increasing with $([\text{Fe}^{2+}]_0)^{1/3}$.

4.6. REFERENCES

- [1] L.L. Stookey, *Anal. Chem.*, 42 (1970) 779-781.
- [2] E. Viollier, P.W. Inglett, K. Hunter, A.N. Roychoudhury, P. Van Cappellen, *Appl. Geochem.*, 15 (2000) 785-790.
- [3] D. Fu, P.G. Keech, X.L. Sun, J.C. Wren, *Phys. Chem. Chem. Phys.*, 13 (2011) 18523-18529.
- [4] C.F. Baes, R.E. Mesmer, *The Hydrolysis of cations*, Wiley, New York, (1976).
- [5] R.J. Knight, R.N. Sylva, *J. Inorg. Nucl. Chem.*, 37 (1975) 779-783.
- [6] B.C. Faust, J. Hoigné, *Atmos. Environ. Part A*, 24 (1990) 79-89.
- [7] D.M. Sherman, D. Waite, *Amer. Mineral.*, 70 (1985) 1262-1269.
- [8] A.J. Davenport, J.A. Bardwell, C.M. Vitus, *J. Electrochem. Soc.*, 142 (1995) 721-724.
- [9] J. Prietzel, J. Thieme, K. Eusterhues, D. Eichert, *Eur. J. Soil Sci.*, 58 (2007) 1027-1041.
- [10] J.F. Boily, P.L. Gassman, T. Peretyazhko, J. Szanyi, J.M. Zachara, *Environ. Sci. Technol.*, 44 (2010) 1185-1190.
- [11] J. Bessiere, M. Perdicakis, B. Humbert, *C.R. Acad. Sci., Ser. IIC: Chim.*, 2 (1999) 101-105.
- [12] J.M. Joseph, B.S. Choi, P. Yakabuskie, J.C. Wren, *Radiat. Phys. Chem.*, 77 (2008) 1009-1020.
- [13] P.A. Yakabuskie, J.M. Joseph, J.C. Wren, *Radiat. Phys. Chem.*, 79 (2010) 777-785.
- [14] P.A. Yakabuskie, J.M. Joseph, C.R. Stuart, J.C. Wren, *J. Phys. Chem. A*, 115 (2011) 4270-4278.
- [15] G.V. Buxton, C.L. Greenstock, W.P. Helman, A.B. Ross, *J. Phys. Chem. Ref. Data*, 17 (1988) 513-886.
- [16] J.C. Wren, in proceedings of ACS Symposium Series, Washington, DC, (2010).
- [17] E.V. Shevchenko, D.V. Talapin, H. Schnablegger, A. Kornowski, Ö. Festin, P. Svedlindh, M. Haase, H. Weller, *J. Am. Chem. Soc.*, 125 (2003) 9090-9101.
- [18] S. Sun, C.B. Murray, D. Weller, L. Folks, A. Moser, *Science*, 287 (2000) 1989-1992.
- [19] L.D. Benefield, J.F. Judkins, B.L. Weand, *Process chemistry for water and wastewater treatment*, Prentice-Hall, Englewood Cliffs, N.J, (1982).
- [20] CRC Handbook of Chemistry and Physics: 61st ed. CRC Press: Boca Raton, FL, 1980.
- [21] E. Ekeröth, O. Roth, M. Jonsson, *J. Nucl. Mater.*, 355 (2006) 38-46.
- [22] R. Boistelle, J.P. Astier, *J. Cryst. Growth*, 90 (1988) 14-30.

Chapter 5. The Effect of pH on the Formation of Iron Oxide Nanoparticles by Radiation

5.1. INTRODUCTION

This chapter examines the effect that the initial solution pH has on the kinetics of iron oxide nanoparticle formation by gamma radiation as well as the final size, morphology, and composition of the resultant particles. The particles form in part due to the difference in the solubility of Fe^{II} and Fe^{III} species. Their solubilities though are also a function of solution pH. Altering the pH changes the threshold for particle nucleation.

This work limits its study to the effect of initial solution pH in the range of 4 to 8 all with different initial iron concentrations to ensure that Fe^{II} species were soluble at that pH, but that Fe^{III} would none the less form precipitate. A similar study was performed and is reported in Chapter 4 which analyzes the impact of changing the $[Fe^{2+}]_0$ of the system which found that the initial concentration has a strong impact on the particle size, not its composition.

5.2. EXPERIMENTAL

5.2.1. Sample Preparation

All solutions were freshly prepared before each experiment with water, purified using a NANOpure Diamond UV ultrapure water system, with a resistivity of 18.2 M Ω -cm. High-purity ferrous sulfate was obtained from Sigma-Aldrich (purity \geq 99%) and used without further purification. Borate buffer solution (0.01 M) was prepared using sodium borate decahydrate (Na₂B₄O₇) with their pH adjusted to 6 and 8.4. Pure water and aqueous

solutions were deaerated by purging with ultra-high purity argon (impurity 0.001%) for more than an hour before solutions were prepared in an argon-filled glove box (O_2 level < 0.1 vol.%). The initial Fe^{2+} concentrations were chosen to ensure solubility at the pH in question and ranged from 0.1 mM to 10 mM. These were prepared with the pH adjusted to 4-8 using 1 N NaOH or 1 N H_2SO_4 (added dropwise). The solution pH was measured using a pH meter (Mettler Toledo) inside the glove box. Aliquots of 10 mL of the prepared solutions were then transferred into 20 mL Pyrex vials (Agilent Technologies) and sealed using PTFE silicon septa.

5.2.2. Sample Irradiation

The vials were irradiated in a ^{60}Co gamma cell (MDS Nordion) as discussed in Chapter 3. The gamma source provided a uniform absorption dose rate of 0.8 Gy/s in the water samples at the time of this study. The samples were all irradiated at room temperature. Samples were irradiated for up to 300 minutes in order to study the kinetics of the reaction. Time between sample irradiation and analysis was minimized to limit the escape of some of the irradiation products such as hydrogen and oxygen.

5.2.3. Sample Analysis

5.2.3.1. Gas Chromatography

After irradiation the headspace in the vials were sampled using an air-tight syringe with Luer lock. This was done in order to get the concentrations of both gaseous oxygen and hydrogen which are generated by water radiolysis.

5.2.3.2. *UV-Vis Spectroscopy*

All of the spectrophotometric measurements were carried out using a diode array detector (BioLogic Science Instruments). The ferrozine method was used to determine the iron speciation of the sample. In this method, an aliquot of the sample at all time points was mixed with a ferrozine reagent. The volume of the aliquot varied with the initial concentration of iron used. Ferrozine complexes with any Fe^{2+} in the solution to produce a complex with an absorbance at 563 nm which has a molar extinction coefficient of $27900 \text{ M}^{-1}\text{cm}^{-1}$. Beer-Lambert's law is then used to determine the $[\text{Fe}^{2+}]$ in the solution. Following this, another aliquot is reduced using hydroxylamine which reduces the Fe^{III} species (both solids and in solution) to Fe^{2+} . This is then mixed with the Ferrozine reagent in order to determine the total concentration of iron in the system. The $[\text{Fe}^{\text{III}}]$ was determined from the difference in $[\text{Fe}^{2+}]$ measured before and after the reduction of Fe^{III} to Fe^{2+} .

5.2.3.3. *pH*

Samples irradiated for all time points had their pHs taken using a pH meter (Mettler Toledo).

5.2.3.4. *Transmission Electron Microscopy*

For TEM analysis, the particles were collected by dipping a carbon-coated copper grid into the irradiated test solution and drying the sample grid in air. The TEM images were obtained with the electron microscope (Philips Electronics) with electrons accelerated to 80 keV.

5.2.3.5. *Fourier Transform Infrared Spectroscopy (FTIR)*

Particles were collected for FTIR analysis from samples irradiated for 300 minutes. The samples were centrifuged and the collected nanoparticles were then left on a glass slide to dry. Once dry, the resultant particles were incorporated into the KBr pellet for the FTIR measurement. FTIR spectroscopy measurements of the iron nanoparticles were performed using an IR spectrophotometer (Bruker Vertex 70v) with Fourier transformation (Bruker) in the 4000 to 400 cm^{-1} frequency range.

5.2.3.6. *Raman Spectroscopy*

Raman spectroscopy was performed to determine the composition of the nanoparticles formed by gamma radiation. The particles were collected from samples irradiated for 300 minutes. The samples were centrifuged and the collected particles were then left on a glass slide to dry. Raman scattering measurements were performed using a Renishaw model 2000 Raman Spectrometer with a laser excitation wavelength of 633 nm.

5.3. RESULTS AND DISCUSSION

The effect of pH on iron oxide nanoparticle formation was investigated over the pH range 4 to 8. The $[\text{Fe}^{2+}]_0$ used at a given pH was chosen to keep the iron concentration below the solubility limit of Fe^{II} at that pH, but well above the solubility limit of Fe^{III} . The range of $[\text{Fe}^{2+}]_0$ and pH used is indicated on the solubility-pH diagram for the iron species in Figure 5.1.

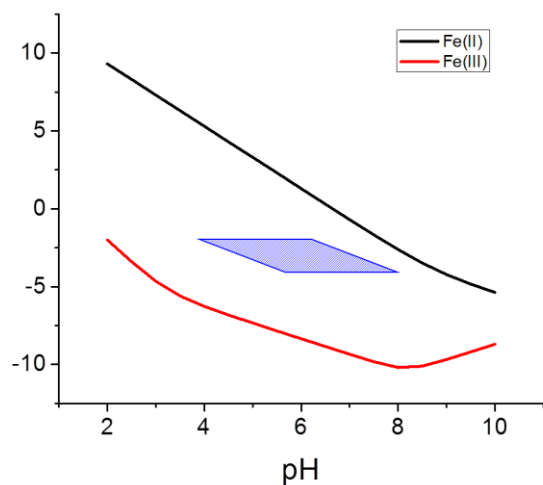


Figure 5.1: The solubilities of ferrous and ferric ions (as hydroxides) at 25 °C (taken from Baes and Mesmer [1]). The blue diamond box indicates the span of the variables used in this study.

The change in pH is related to the hydroxide/oxide formation from dissolved ferrous ion [2]:



The same relationship exists for the ferric ion in aqueous solutions:



These dissolved species can go on to form a solid phase from the neutral species generated ($\text{Fe}(\text{OH})_2$ and $\text{Fe}(\text{OH})_3$). Throughout this thesis, Fe^{2+} will be used to denote any of the soluble species in reactions 5.1 and 5.2, $\text{Fe}^{2+}_{(\text{ad})}$ will be used to denote adsorbed onto the surface, but not quite incorporated into the growing oxide, and finally Fe^{II} indicates that

the species discussed is in one of the solid forms. Similar nomenclature will be used for Fe^{3+} , $\text{Fe}^{3+}_{(\text{ad})}$, and Fe^{III} .

The discussion of the particle formation is divided between two pH ranges. The acidic region will refer to experiments performed at pH values of 4-6. The basic region will refer to experiments performed at pH values of 7-8. The reason for this distinction is that these regions exhibit different oxide compositions and undergo slightly different mechanistic pathways (further discussed in section 5.3.4).

5.3.1. Particles prepared at pH 4 - 6

The general reaction proceeded by the same general three stage mechanism observed previously [3]. The hydrogen evolution and pH of the solution were monitored as a function of irradiation time and can be found in Figure 5.2. The pH of the solution was found to drop to the acidic region within the first ten minutes of irradiation irrespective of initial solution pH. This is because when Fe^{2+} is oxidized to Fe^{3+} it will generate protons as per reactions 5.3-5.5 before going into the solid phase. The sulphate and the $\text{Fe}^{3+}_{(\text{aq})}$ generated in the solution both have pKa values at 1.99 and 2.43 respectively [4-6]. Thus both of these species act as buffers in this region and prevent the pH from dropping much further.

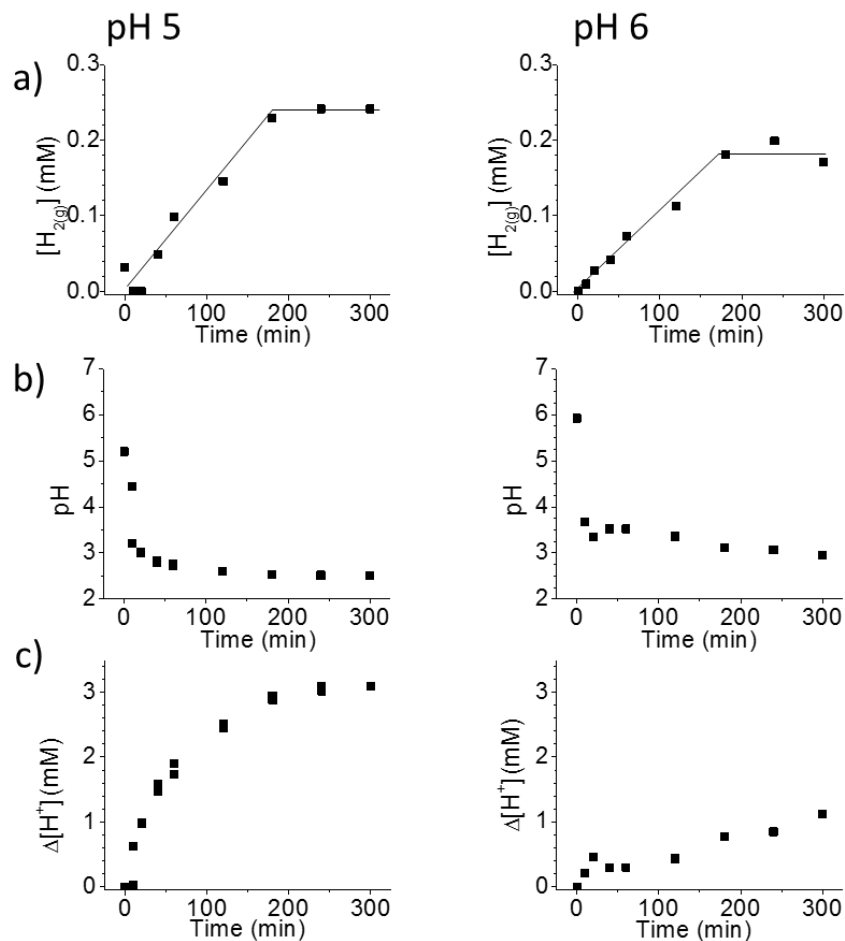


Figure 5.2: Kinetic data for solutions containing $[Fe^{2+}]_0 = 1$ mM and a pH of either 5 or 6. Plots a) compares the hydrogen evolution above the reaction solution as a function of irradiation time, b) shows the pH in the reaction vessel measured as a function of irradiation time, and c) the change in proton concentration.

Chapter 4 established that concentration does not significantly impact the pH of the solution as the reaction progresses. Figure 5.2 shows the pH drop of two solutions with different initial pH values. Changes in pH do not affect the radiolytic oxidation of Fe^{2+} to Fe^{III} because the production rates of radiolysis products are independent of the pH in this range. However, it is clear that a drop in the pH will have a considerable impact on the solubility of ferrous and ferric ions and this will affect the rates of dissolution and re-precipitation during Oswald ripening of oxide particles. The kinetics of oxidation proceeds

in the same fashion when acidic pH values were used. The final oxidation yield is independent of the initial pH. This is unsurprising given that the radiolysis speciation is not expected to change with pH and thus the extent of oxidation should be consistent across a wide range of pH values.

The hydrogen evolution was examined as a function of pH. Generally, the trends were dependent more on the initial iron concentration of the solution rather than the pH. Given that the pH drops to the same value over the course of the experiment regardless of initial pH this is intuitive. Further, the primary source of hydrogen in solution is from the net reduction of water. This rate will be dependent on two factors, the radiolysis environment and the rate of oxidation of iron. The radiolysis environment doesn't change significantly with pH range studied in this chapter (see Section 5.3.3) while the oxidation rate also doesn't change with pH.

The transmission electron images show the morphology of particles formed after 20 minutes and 5 hours of irradiation for samples studied with initial pH 4-6 (Figure 5.3). The TEM images of particles formed after 20-min irradiation show that spherical particles are formed in solutions with an initial pH of 4 to 6. The spherical particles aggregate and grow into a dendritic structure. The TEM images at 20 min show areas with two different shades. The darker areas are well-defined, denser particles of 20-30 nm in size. The lighter areas are made up of very small particles (a few nm in diameter) which appear to have aggregated during collection on the TEM grids. The shading becomes darker and the number of the denser particles increases with increasing irradiation time, 300 min, suggesting that the smaller particles are combining and growing into the larger and denser oxide particles. At longer irradiation time (300 min), the larger particles appear to have undergone coarsening or Ostwald ripening to form even larger dendritic particles. After 5

hours of irradiation they have grown to their pseudo steady state size still maintaining the dendritic structure.

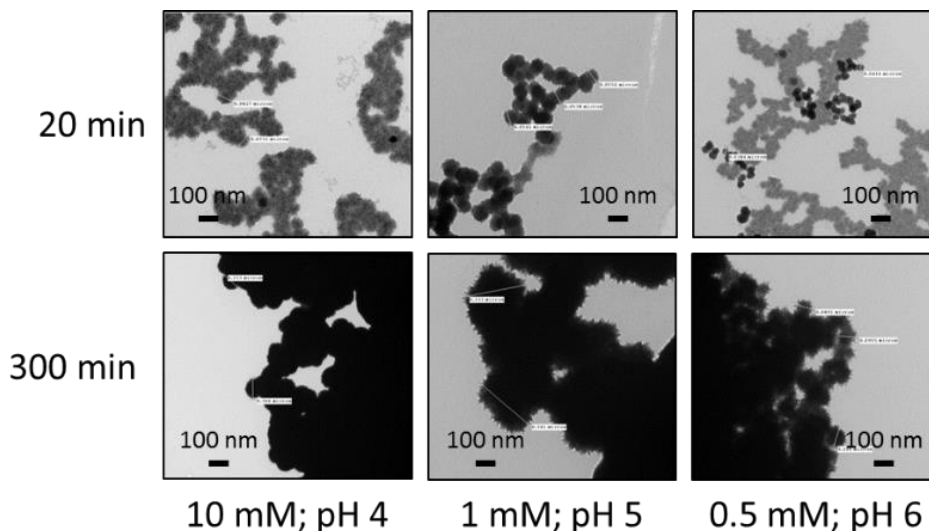


Figure 5.3 Transmission electron micrographs of particles formed with initial conditions indicated after 20 minutes and 5 h of irradiation.

The average sizes and standard deviations of the particles synthesized are shown in Table 5.1. Generally, it seems that size increases with a decreased initial pH coupled with an increase in variability in the particle size. At lower pH values, iron species would be more soluble and thus the rapid oxidation events would produce fewer nucleates on which particles can grow. Net oxidation of iron was consistent despite a change in initial pH thus, the same amount of Fe^{III} is consequently spread amongst fewer nucleates.

Table 5.1: Average particle sizes and standard deviation determined at the $[\text{Fe}^{2+}_{(\text{aq})}]_0$ and pH studied.

Concentration (mM)	pH	Population Size	Average Size (nm)	Standard Deviation (nm)
1	6	8	140	30
	5	4	280	70
10	6	5	300	40
	4	10	390	70

The FTIR spectra (Figure 5.4) show that at pH 6 the sample has broad peaks at 450-550, 600, 650-750, 1350-1500, 1600-1750 cm^{-1} . The peak cluster just above 1000 cm^{-1} is the result of sulfate absorbance [7]. The broad peak within the range of 2500-4000 cm^{-1} is the result of the O-H stretch in water which was present in the sample [8]. Because of the broadness of the peaks and the inability to effectively see the range blocked by sulfate and water, it is impossible to definitively identify an oxide. The relative peak intensities of the visible peaks do not correspond to any one oxide and is thus a mixture. Ferrihydrite seems to be the dominant species as it has broad peaks at 450-550, and 650-750 cm^{-1} . The pH 4 sample produced a much weaker signal and as such it is impossible to make any firm analyses from the FTIR alone.

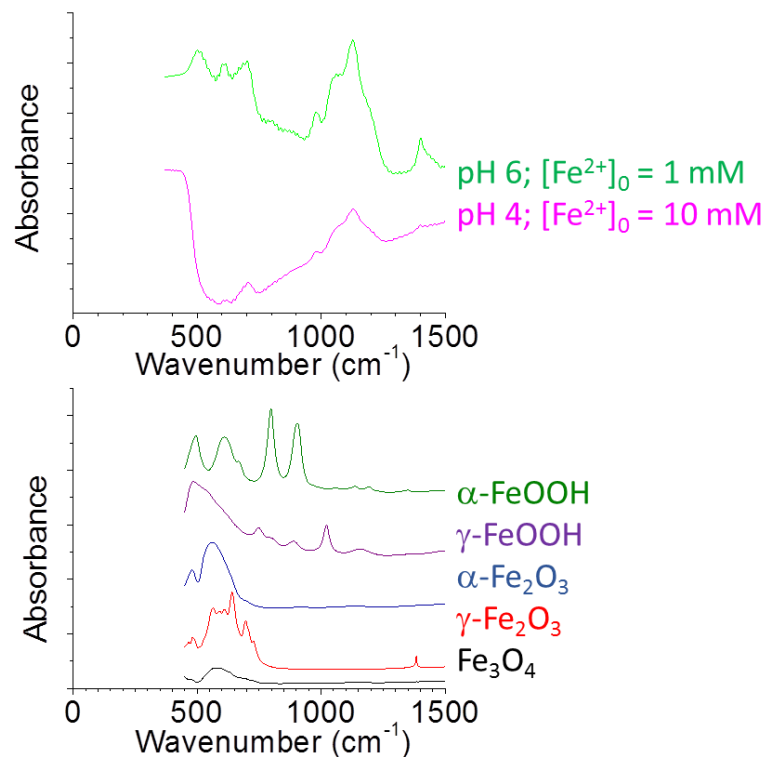


Figure 5.4: FTIR spectra of samples obtained after five hours of irradiation under conditions indicated on the graph. Standard are displayed underneath for reference.

The Raman spectra obtained for solutions with different initial pH values are shown in Figure 5.5. The Raman spectra of the particles formed at initial pH 5 and 6 are similar, having the peaks at 300, 350, 420, 560 and 720 cm^{-1} that are consistent with the mixed $\text{Fe}^{\text{II}}/\text{Fe}^{\text{III}}$ oxyhydroxide mixture reported in Chapter 4. The peaks at 420 and 560 cm^{-1} correspond to green rust II an $\text{Fe}^{\text{II}}/\text{Fe}^{\text{III}}$ mixed oxide with SO_4^{2-} occupying some of the anionic positions within the oxide structure [9]. The peaks at 350, 560 and 720 cm^{-1} correspond to ferrihydrite [10]. The peak at 700 cm^{-1} can also be attributed to magnetite (Fe_3O_4), which is only weakly Raman active in comparison to the other oxides. Finally, the modest peak at 300 cm^{-1} corresponds to goethite ($\alpha\text{-FeOOH}$) or haematite ($\alpha\text{-Fe}_2\text{O}_3$) though because of its low absorbance, it is difficult to say definitively as the other characterization peaks overlap with the other oxides present [10]. Analysis of the peak at 1000 cm^{-1} is omitted because it corresponds to a sulphate peak which is present in the sample [11].

These results are consistent with those determined from Chapter 4, therefore the oxide formed is most likely magnetite which is not very Raman active. The oxides observed above were also observed at pH 6, but upon analysis with XANES it was deduced that the particles were predominantly magnetite. The oxides observed herein are primarily small contributions to the overall composition. However, there are minor variations in the intensities of the peaks, suggesting that the ratios of Fe^{II} and Fe^{III} in the mixed oxyhydroxide are different for particles formed at different initial pHs with slight increases in the green rust character of the oxides produced in lower pH solutions.

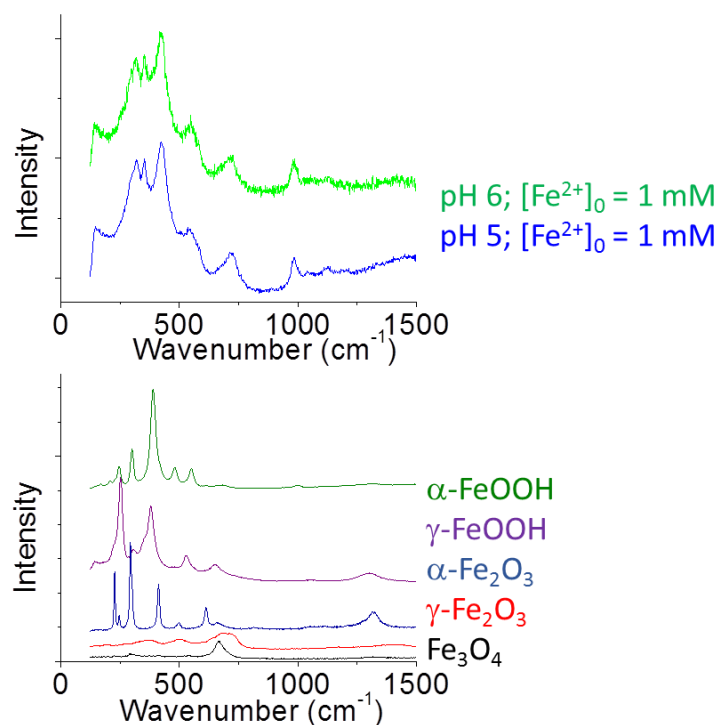


Figure 5.5: The Raman spectra of samples prepared from solutions with different pH values which were irradiated for five hours. Standards are displayed underneath for reference.

5.3.1.1. Particles Prepared in pH 6 Buffered Solutions

In order to examine the effect of pH while isolating the pH change with irradiation time, analogous samples in the presence of borate buffers were irradiated. The pH was monitored with irradiation time and there was no change in pH indicating that the buffer solution was stable. The Raman spectra are shown in Figure 5.6. The composition of the nanoparticles formed remained similar to the one obtained without buffer, but the buffered solution has enhanced peaks at 420 and 320 cm^{-1} which correspond to an higher contribution from goethite ($\alpha\text{-FeOOH}$) though still a mixed oxide.

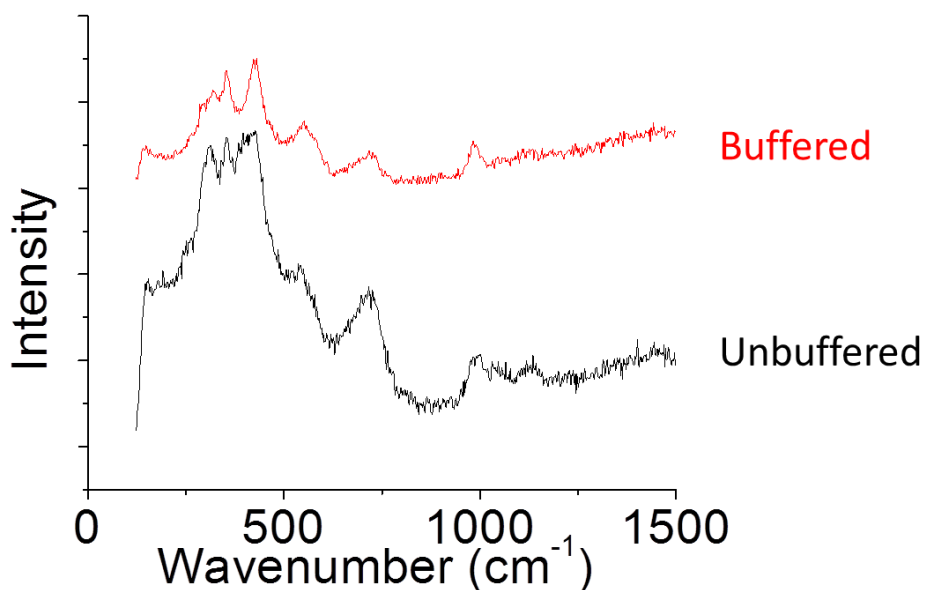


Figure 5.6 Raman spectra of two solutions with initial pH of 6 and $[\text{Fe}^{2+}_{(\text{aq})}]_0 = 0.5 \text{ mM}$. The top spectrum was buffered with borate and its pH did not change during the experiment. The bottom spectrum was not buffered and its pH dropped into the acidic region over the course of the reaction.

The TEM images (Figure 5.7) shows that the particles produced in a buffered solution have different morphologies consisting of smaller circular particles embedded in a slightly lighter mesh. The long-term kinetics of a solution with pH of 6 favours the formation of goethite ($\alpha\text{-FeOOH}$) to an extent in the solution. It was incredibly difficult to obtain images of particles generated from this solution. At an increased pH, the particles are much more insoluble and therefore likely much larger making them difficult to capture in the TEM grid.

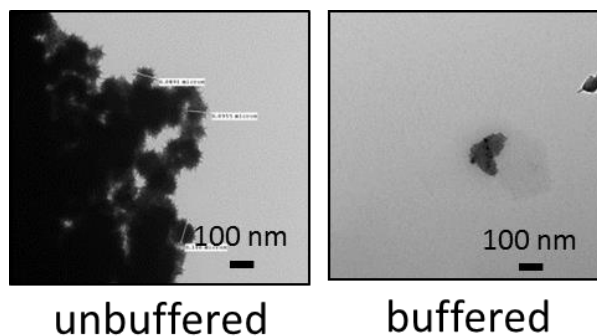


Figure 5.7: TEM images obtained after five hours of irradiation. Both systems were $[\text{Fe}^{2+}]_0 = 0.5 \text{ mM}$ and $\text{pH}_0 = 6$. The ‘buffered’ solution contained 0.01 M borate.

5.3.2. Particles Prepared at pH 7 & 8

Initial solution pH values of 7 & 8 were examined, but are separated because the results were sufficiently unique to merit its own discussion. The pH of the solution was monitored over the course of the reaction and shown in Figure 5.8. No change is expected in many of the water radiolysis reactions, including that of the hydroxyl radical. They are not significantly pH dependant in the range studied in this chapter (discussed in greater detail in 5.3.3. Computational Analysis).

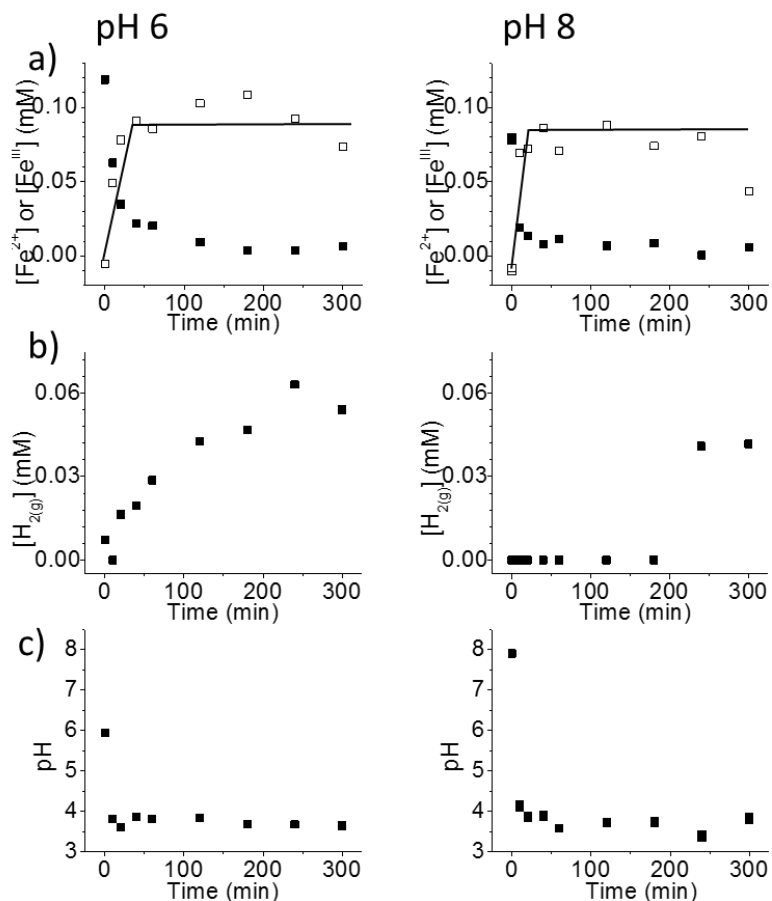


Figure 5.8: Kinetic data for solutions containing $[\text{Fe}^{2+}]_0 = 0.1 \text{ mM}$ and a pH of either 6 or 8. a) shows the concentration of Fe^{II} (black squares) Fe^{III} (white squares) measured in the reaction solution as a function of irradiation time, b) compares the hydrogen evolution above the reaction solution as a function of irradiation time, and c) shows the pH in the reaction vessel measured as a function of irradiation time.

The kinetics of oxidation of Fe^{2+} to Fe^{III} is consistent between the different pH values. The rate at which Fe^{3+} was generated would have remained the same. One key difference though is that at the pH of 7 and up, the dominant Fe^{3+} species would be $\text{Fe}(\text{OH})_{3(\text{aq})}$. Because of the rapid pH drop this would only be true of the earliest particle growth, but it is sufficient to alter the nature of the nucleate.

The evolution of hydrogen seems most influenced by the concentration of $[\text{Fe}^{2+}]_0$ rather than the pH. The oxidation rate, again, doesn't seem to change with pH thus the

similarity between the hydrogen generation rates is unsurprising. The pH experienced a dramatic drop upon irradiation settling at just under 4 in both cases. Though in both cases, the detected hydrogen is near the detection limit of 3 μM .

At pH 7, after twenty minutes of irradiation fewer number of particles were observed and after five hours there is a large contribution from different oxides given with two apparent particle densities. At pH 8, sharp crystals are observed after twenty minutes of irradiation. At higher pHs, the particles begin to show different morphological features even at early times (Figure 5.9). At pH 8, the particles grow in a rod shape. This is the crystal morphology generally associated with $\gamma\text{-FeOOH}$ (lepidocrocite) [12]. The rod shaped crystals grow in size and also become denser with increasing time.

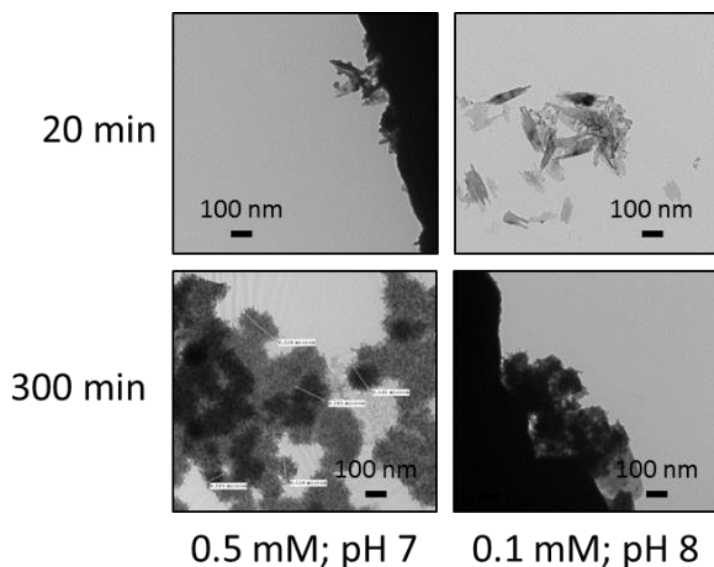


Figure 5.9: TEM images of particles formed with initial conditions indicated after 20 minutes of irradiation and 5 h of irradiation.

Figure 5.10 shows the TEM images of the particle formed at pH 8 with $[\text{Fe}^{2+}]_0 = 0.1 \text{ mM}$ before irradiation and after twenty and sixty minutes of irradiation. When comparing the particle generated under radiation to those produced without radiation, it

becomes evident that oxidation took place prior to radiation and despite the unique system conditions produced by radiation induced no significant structural changes in the resultant product. Despite this, it does appear that increased irradiation time may have caused some cross linking in the lepidocrocite (γ -FeOOH) networks causing the particles to cascade together. There was also considerable difficulty in obtaining images of particles from this system for five hours of irradiation. This is attributed to the enhanced network reducing particle uptake by the TEM grid.

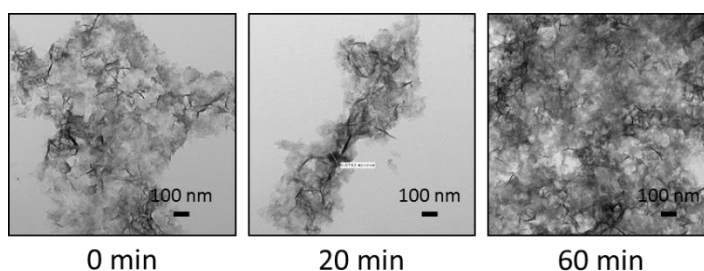


Figure 5.10: TEM images of particles from a solution with $[\text{Fe}^{2+}]_0 = 0.1 \text{ mM}$, and a pH_0 of 8. The images were obtained prior to irradiation and after 20 and 60 minutes of irradiation time.

Figure 5.11 shows the Raman data for solutions with different pH and initial concentrations after 5 hour of irradiation. The change in composition of the oxide becomes evident at initial pH 7 where we begin to see clear contributions to the spectrum from peaks characteristic of lepidocrocite at 250, 348, 528, and 650 cm^{-1} . These peaks become the dominant feature of the spectra of particles formed at pH 8 though there are still contributions from the magnetite peak at 700 cm^{-1} . The increase in pH leads to a unique initial growth phase. At alkaline pH values, the nucleation process occurs through a different mechanism where iron is prematurely oxidized to Fe^{3+} forming the nucleate prior to irradiation. Upon irradiation the water radiolysis products would continue to reduce and

oxidize the particles resulting in differing morphology from those formed purely from oxidation in an alkaline medium, but similar composition. These pH differences are only of great importance during the earliest stages of the particle formation. Therefore it seems likely that the composition of the particle depends greatly on the kinetics of the nucleation and early growth of the particles. These early particles have unique coordination sites to one another when formed at different pH values which favour the continued growth of either the mixed oxide composition at pH 6 or lower or lepidocrocite (γ -FeOOH) at a higher pH even after the bulk solution pH drops into the acidic range. However, at the longest time points, the particles look more like those formed in the acidic region suggesting that the composition is converting from the lepidocrocite mixed oxide intermediate to the final magnetite composition.

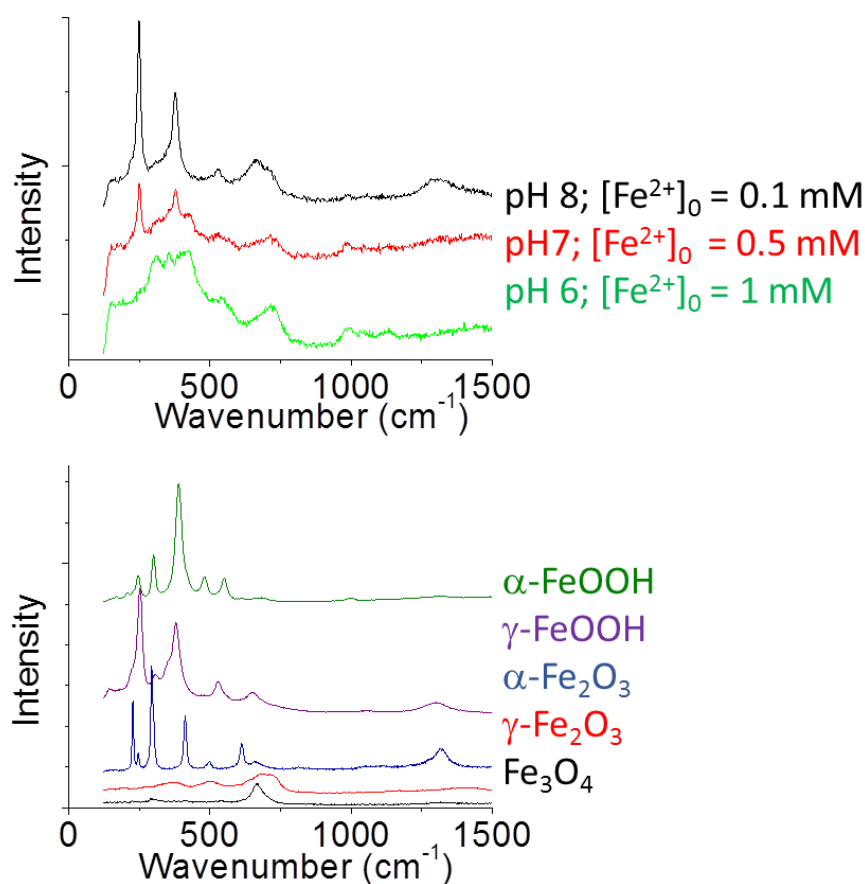


Figure 5.11: The Raman spectra of samples prepared from solutions with different pH values and different concentrations which were irradiated for five hours. Standards are displayed underneath for reference.

5.3.2.1. Particles Prepared in pH 8 Buffered Solutions

A similar buffered experiment was performed at pH 8. It was found that there was a slight shoulder produced in the Raman spectrum (Figure 5.12) at 340 cm^{-1} , a new peak at 560 cm^{-1} and an enhancement of the peak already present at 720 cm^{-1} . This may indicate that when the solution is held at pH 8 rather than being allowed to drop into the acidic region, the preference towards lepidocrocite isn't maintained to the same degree allowing other oxides to persist. The new peaks are most consistent with ferrihydrite indicating that the oxide is incapable of fully oxidizing to the more stable lepidocrocite product. This is

attributed to the solubility, at pH 8, the oxides would be incredibly insoluble and thus once an oxide is formed, it is incapable of solubilizing and reprecipitating as a more stable oxide.

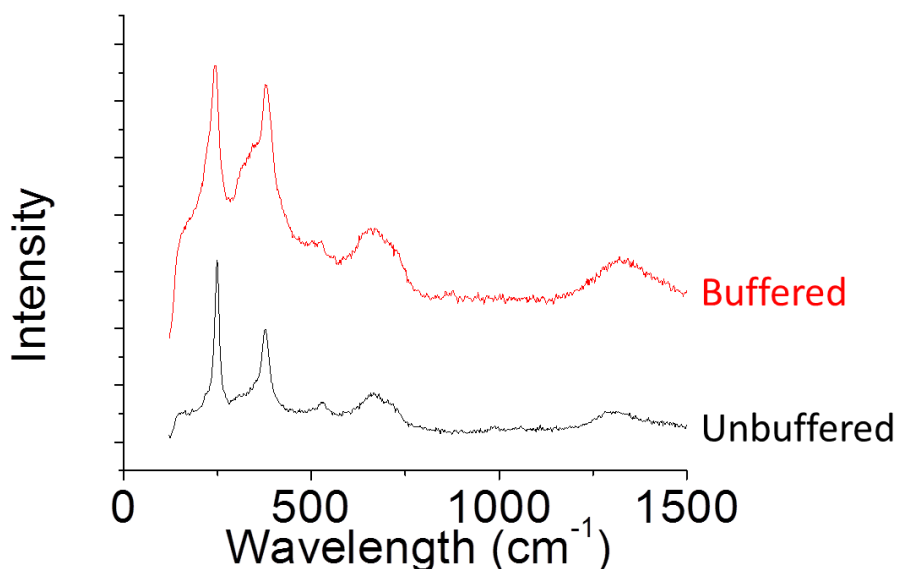


Figure 5.12: Raman spectra of two particle samples grown in solution. The `unbuffered` with an initial pH of 8 and $[\text{Fe}^{2+}]_0$ of 0.1 mM. The `buffered` with an initial pH of 8 and $[\text{Fe}^{2+}]_0$ of 0.1 mM. The top spectrum was buffered with borate and its pH did not change during the experiment. The bottom spectrum was not buffered and its pH dropped into the acidic region over the course of the reaction.

The TEM (Figure 5.13) shows a complex network grown in the buffer solution. This is different to the product formed without the addition of a buffer (Figure 5.9), but similar to the products produced without a buffer at shorter time points (Figure 5.10). This indicates that since the system was maintained at a more insoluble pH, the networks did not crosslink as effectively and therefore were able to be captured in the TEM grid. The structure itself seems less needle like and embedded with larger dark areas which are attributed to the presence of ferrihydrite.

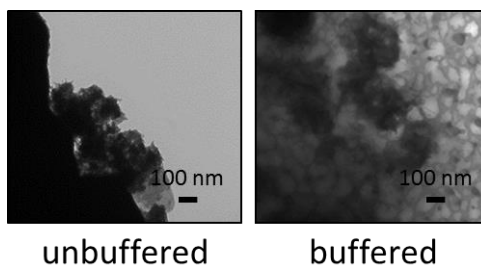


Figure 5.13: TEM images obtained after five hours of irradiation. Both systems were $[\text{Fe}^{2+}]_0 = 0.1 \text{ mM}$ and $\text{pH}_0 = 8$. The ‘buffered’ solution contained 0.01 M borate.

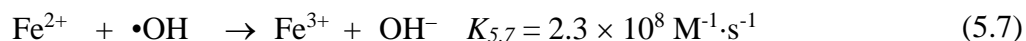
5.3.3. Computational Analysis

Gamma-radiation decomposes water molecules and forms primary radiolysis products homogeneously and nearly instantaneously (in a chemical reaction time scale). To determine the time dependence of the concentrations of the key oxidants and reductants produced by radiolysis we have modelled the water radiolysis chemistry. The model consists of about 45 water radiolysis reactions involving more than 10 chemical species and has been validated against experimental data obtained under a wide range of solution conditions [13, 14]. A set of calculations was performed to model deaerated solutions containing different $[\text{Fe}^{2+}]_0$ at different pH values.

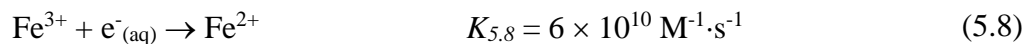
Modelling was performed to simulate the radiolysis speciation with and without iron at a variety of conditions. Though there are a number of water radiolysis reactions to consider, only one of the key reactions is actually pH dependant (reaction 5.6).



These models included the following iron reactions (reactions 5.7 & 5.8) in addition to the numerous radiolysis reactions.



$$k_{10} = 2.3 \times 10^8 \text{ M}^{-1}\cdot\text{s}^{-1} \quad (6)$$



Because the model does not take into account heterogeneous oxidation of iron and the complex relationship between the many phases of iron oxides, it is only presumed to be effective in the earliest time points, those which correspond to the nucleation events. First, the pure water radiolysis of pH 4, 6, and 8 were performed (Figure 5.14). As expected, as the pH is decreased, and thus $[\text{H}^+]$ increased, the concentration of solvated electrons dropped while those of the molecular products increased slightly. Beyond this though, the radiolysis products remained more or less consistent at all pH values.

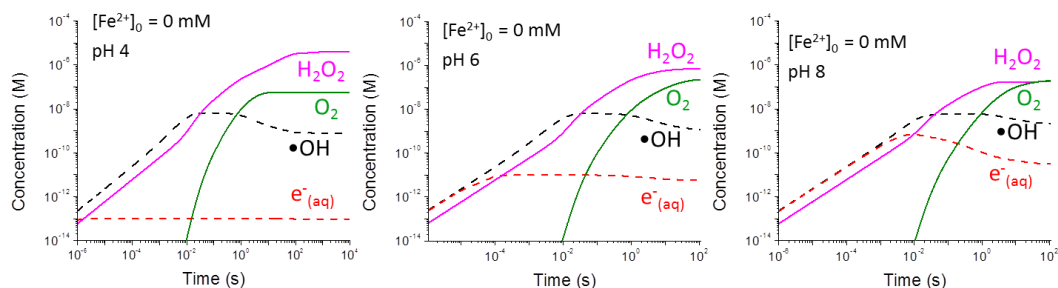


Figure 5.14: Computer modelling performed to simulate the key radiolysis products generated in pure water solutions held at constant pH.

When an initial iron concentration is taken into account, the modelling in Figure 5.15 is produced. Generally, the presence of hydroxyl radicals is enhanced at lower concentrations of ferrous iron as it is not consumed in the oxidation of iron. The solvated electron concentration also follows the same pH dependant trend observed in pure water. The model predicts that the concentration and pH of the system are largely irrelevant to the rate at which Fe^{III} accumulates in the system.

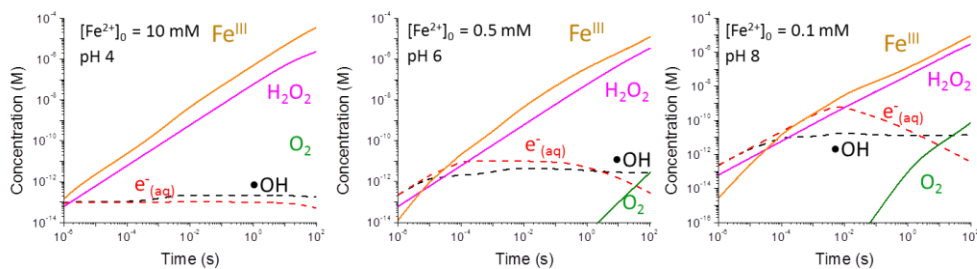


Figure 5.15: Computer modelling performed to simulate the key radiolysis products generated in Fe^{2+} solutions held at constant pH.

5.3.4. Mechanism

Generally speaking the mechanism proceeds through the same mechanism at all pH values, though pH does have significant impacts on how the size and composition evolve through these stages.

5.3.4.1. Stage 1: Nucleation

In Stage 1, the particles are nucleated by the hydroxyl radical. These are generated by water radiolysis and are produced at the same rate for all pH values. What does change with pH is the solubility limit of Fe^{III} . The solubility limit of Fe^{III} is reached at the order of 1 s for a pH of 4, 10^{-2} s for a pH of 6. These moments are all reached on a timescale short enough to ensure that the pH drop experienced by the system has not taken effect yet. The faster the solubility limit is reached the higher the degree of saturation and the greater the number of nucleates produced. For the acidic pH values, this results in fewer nucleates at lower pH. The results described above found little change in the way of oxidation yields or kinetics. The same amount of Fe^{III} is generated after five hours, but at lower pH values is divided between fewer nucleates and so generates larger particles. The pH 6 buffered solution nucleates in the same way as the unbuffered solution.

At pH 8 the concentration of Fe^{2+} is theoretically below the solubility limit however TEM images found particulate matter with no irradiation time. This is characteristic behaviour of Ferrihydrite and Green Rust [15] which obscures the actual solubility limit in iron systems. As such, the pH 8 system is prematurely nucleated independent of irradiation. The pH 8.4 buffered solution nucleates in the same way as the unbuffered solution.

5.3.4.2. Stage 2: Growth

In Stage 2, the Fe^{2+} adsorbs on existing particles and oxidizes, thereby growing a mixed $\text{Fe}^{\text{II}}/\text{Fe}^{\text{III}}$ oxyhydroxide ($\text{Fe}_3(\text{O})_n(\text{OH})_{8-2n}$) at low pHs or lepidocrocite at pHs > 7 . The conversion of $\text{Fe}^{2+}_{(\text{ad})}$ to Fe^{III} in Stage 2 is controlled by the rates of oxidation and reduction of the adsorbed species on the growing particles. The dominant oxidant at this stage is the hydrogen peroxide molecule which accumulates to appreciable values. Growth in this phase follows an adsorption, oxidation mechanism. As such, the composition of the growing oxide is influenced by the adsorption sites on the growing particles. The oxidation within the system occurs at similar rates across pH values. The composition of the oxide converts from the transient nucleate to FeOOH intermediates and finally to magnetite. The particles grown in acidic media grow on the circular nucleates to form dendritic mixed oxide particles as more and more iron is added into the structure. Iron begins to cycle between Fe^{2+} and Fe^{III} . In a pH 6 buffered solution, the growing particles will be less soluble. Thus the particles have less $\text{Fe}^{3+}_{(\text{ad})}$ on the structure and convert to magnetite much more slowly, leaving more of the intermediate, goethite, in its composition (as seen in the Raman spectrum Figure 5.6). Though both buffered and unbuffered contain contributions from both haematite and magnetite.

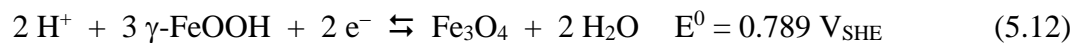
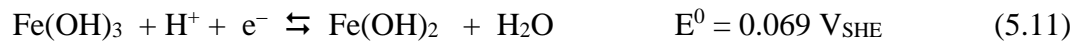
The particles grown in basic media grow on the prematurely formed nucleates, these nucleates have different coordination sites on the surfaces and initially high pH both promote the growth of lepidocrocite (γ -FeOOH). This explains the sharp rod like networks that existed in the shorter timeframes for pH 8. Looking to the buffered pH 8.4 system, the system remains at an insoluble pH for the duration. The lepidocrocite is still grown, however with such a high pH, thermodynamically unstable ferrihydrites are capable of persisting on the particle surface because they are not converting to lepidocrocite via dissolution-precipitation.

5.3.4.3. Stage 3: Pseudo Steady-State

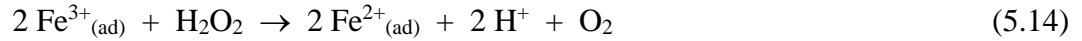
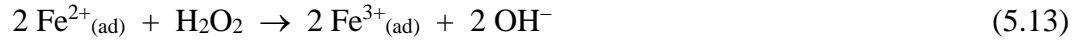
Stage 3, mainly involves cyclic Fe^{II} and Fe^{III} redox reactions with a small or negligible net oxidation rate while the particles undergo coarsening or agglomeration. Hence, the [Fe^{III}] does not change significantly with time. Although the net rate of Fe²⁺ to Fe^{III} oxidation is zero the redox system is dynamic, powered by a continuous radiation flux. In particular, radiolytically-produced H₂O₂ can act as an oxidant for Fe^{II} and as a reductant for Fe^{III}. The standard redox potentials for H₂O₂ reduction to OH⁻ and its oxidation to O₂ are known:



The standard redox potentials for various Fe^{II} and Fe^{III} redox pairs are also well established [5]. For example:



Thus, depending on the surface activities of $\text{Fe}^{2+}_{(\text{ad})}$ and $\text{Fe}^{3+}_{(\text{ad})}$, $[\text{H}_2\text{O}_2]$, $[\text{O}_2]$ and pH the iron redox system can establish a catalytic cycle such as,



While the redox cycle continues the ferrous and ferric ions also continuously desorb and adsorb on particles and are in dynamic equilibrium as well:



Agglomeration or coarsening of particles occurs through the continuous dissolution-precipitation of particle constituent atoms because larger particles are in general energetically more stable than smaller particles, known as Ostwald ripening [16]. In Stage 3, the rates of the forward and reverse reactions of these equilibria are high in the presence of radiation and this will accelerate the Ostwald ripening process. These processes are responsible for the conversion of the intermediate (α -FeOOH for acidic media and γ -FeOOH for basic) to the final magnetite form. The final composition will bear the marks of the intermediate through which it grew. The particles grown in acidic media show mixed oxides and goethite peaks, while that of particles grown in basic media exhibit strong peaks of lepidocrocite though both convert to magnetite.

In buffered cases, these conversions occur more slowly. High pH solutions are more intolerant of soluble Fe^{2+} and Fe^{3+} and therefore these are less available to undergo dissolution-precipitation conversions. With solutions buffered at 6, this results in the persistence of the goethite intermediate. With solutions buffered at pH 8.4, the ferrihydrite is capable of persisting without being converted to lepidocrocite.

5.4. SUMMARY

The effects of pH on the kinetics of γ -radiation induced formation and growth of iron oxyhydroxide nanoparticles from dissolved ferrous ions were investigated. The initial pH affects the rates of the elementary reaction steps. The initial pH has negligible influence on the radiolytic oxidation rates. The pH of solution has a negligible effect on the oxidation yield. However, it can affect the adsorption and dissolution rates of ferrous and ferric species. For a given pH the radiolytic oxidation of ferrous to ferric species shows three distinct kinetic stages. In Stage 1, solution-phase oxidation of Fe^{2+} to Fe^{3+} by radiolytically-produced $\bullet\text{OH}$ occurs almost instantaneously. This is followed by rapid hydrolysis of the Fe^{3+} to $\text{Fe}(\text{OH})_{3(\text{s})}$ which triggers precipitation to form nucleate particles. In Stage 2 the dissolve Fe^{2+} can precipitate on the nucleate particles to form mixed oxyhydroxides intermediates on which the $\text{Fe}^{2+}_{(\text{ad})}$ is oxidized to Fe^{III} on the growing particle surfaces by H_2O_2 . These intermediates differ depending on the initial pH of the solution with goethite being favoured with acidic solutions and lepidocrocite favoured in basic solutions. As $\text{Fe}^{3+}_{(\text{ad})}$ is formed on the surface, it is incorporated into the solid oxide phase and slowly grows into the iron oxyhydroxide particles. Depending on the rates of adsorption of Fe^{2+} and its oxidation to Fe^{III} the particles grow into a mixed $\text{Fe}^{\text{II}}/\text{Fe}^{\text{III}}$ consisting predominantly of magnetite. Increased pH values suppress the conversion to the mixed $\text{Fe}^{\text{II}}/\text{Fe}^{\text{III}}$. In Stage 3, no net oxidation of Fe^{2+} to Fe^{III} occurs, but the irradiated system is in dynamic steady state. Coarsening of the particles by continuous dissolution and precipitation occurs while the surface redox reactions of ferrous and ferric species continue. The particles grow into a dendritic structure. As long as the particles are formed by similar intermediates, their size

increases with decreasing pH. Fewer nucleates are generated at lower pH values, but oxidation yield remain the same and so more iron is divided amongst fewer nucleates resulting in larger particles at lower pH values.

5.5. REFERENCES

- [1] C.F. Baes, R.E. Mesmer, *The Hydrolysis of cations*, Wiley, New York, (1976).
- [2] L.D. Benefield, J.F. Judkins, B.L. Weand, *Process chemistry for water and wastewater treatment*, Prentice-Hall, Englewood Cliffs, N.J, (1982).
- [3] P.A. Yakabuskie, J.M. Joseph, P. Keech, G.A. Botton, D. Guzonas, J.C. Wren, *Phys. Chem. Chem. Phys.*, 13 (2011) 7167-7175.
- [4] D.L. Leussing, I.M. Kolthoff, *J. Am. Chem. Soc.*, 75 (1953) 2476-2479.
- [5] CRC Handbook of Chemistry and Physics: 61st ed. CRC Press: Boca Raton, FL, 1980.
- [6] J.G. Hem, W.H. Cropper, Survey of Ferrous-Ferric Chemical Equilibria and Redox Potentials, in: Interior (Ed.), United States Government Printing Office, Washington, 1959.
- [7] J.F. Boily, P.L. Gassman, T. Peretyazhko, J. Szanyi, J.M. Zachara, *Environ. Sci. Technol.*, 44 (2010) 1185-1190.
- [8] F. Cheng, Q. Cao, Y. Guan, H. Cheng, X. Wang, J.D. Miller, *Int. J. Miner. Process.*, 122 (2013) 36-42.
- [9] J. Bessiere, M. Perdicakis, B. Humbert, *C.R. Acad. Sci., Ser. IIC: Chim.*, 2 (1999) 101-105.
- [10] S. Das, M.J. Hendry, *Chem. Geol.*, 290 (2011) 101-108.
- [11] W. Martens, R.L. Frost, J.T. Kloprogge, P.A. Williams, *J. Raman Spectrosc.*, 34 (2003) 145-151.
- [12] D.G. Lewis, V.C. Farmer, *Clay Miner.*, 21 (1986) 93-100.
- [13] J.M. Joseph, B.S. Choi, P. Yakabuskie, J.C. Wren, *Radiat. Phys. Chem.*, 77 (2008) 1009-1020.
- [14] G.V. Buxton, C.L. Greenstock, W.P. Helman, A.B. Ross, *J. Phys. Chem. Ref. Data*, 17 (1988) 513-886.
- [15] R.M. Cornell, U. Schwertmann, *The iron oxides: structure, properties, reactions, occurrences and uses*, VCH, Weinheim; New York, (1996).
- [16] R. Boistelle, J.P. Astier, *J. Cryst. Growth*, 90 (1988) 14-30.

Chapter 6. The Effect of Radical Scavengers on the Formation of Iron Nanoparticles

6.1. INTRODUCTION

This chapter examines the effect different free radical scavengers have on the size and composition of iron oxide nanoparticles formed by gamma radiolysis. Scavengers are powerful tools in examining reaction mechanisms. In this study, nitrous oxide was used to scavenge the solvated electron. The solvated electron is a powerful reducing agent and critically important at the shorter time scale of the reaction. Tert-butanol was used to scavenge the hydroxyl radical. Hydroxyl radicals are powerful oxidizing agents and assumed to be the primary oxidizer at short time scales involved in the conversion of Fe^{2+} to Fe^{3+} . Computer modelling was also performed to analyze the speciation in solution when these scavengers are present. The results of these studies were then rationalized in terms of the existing reaction mechanism.

6.2. EXPERIMENTAL

6.2.1. Sample Preparation

All solutions were freshly prepared before each experiment with water, purified using a NANOpure Diamond UV ultrapure water system, with a resistivity of 18.2 $\text{M}\Omega\cdot\text{cm}$. High-purity ferrous sulfate was obtained from Sigma-Aldrich (purity $\geq 99\%$) and used without further purification. The tertiary butanol obtained from Sigma-Aldrich was of high purity (purity $\geq 99\%$). Gas containing 50% N_2O in Ar (purchased from Praxair (impurities $< 0.001\%$)) was used for performing experiments requiring N_2O addition. Pure water and

aqueous solutions were deaerated by purging with ultra-high purity argon (impurity 0.001%) for more than one hour before solutions were prepared in an argon-filled glove box (O_2 level < 0.1 vol.%). Solutions containing Fe^{2+} in the concentration range 0.1 mM and 1 mM were prepared with the pH adjusted to 6 using 1 N H_2SO_4 (added dropwise). The solution pH was measured using a pH meter (Mettler Toledo) inside the glove box. Aliquots of 10 mL of the prepared solutions were then transferred into 20 mL Pyrex vials (Agilent Technologies) and sealed using PTFE silicon septa. For experiments performed with N_2O each of the capped vial were purged with N_2O/Ar gas mixture for 15 minutes prior to irradiation. Based on Henry's law this achieves a concentration of N_2O in solution of 0.012 M. For experiments using t-butanol, each capped vial was injected separately with the appropriate volume of t-butanol to get the desired concentration (0.026 M).

6.2.2. Sample Irradiation

The vials were irradiated in a ^{60}Co gamma cell (MDS Nordion) as discussed in Chapter 3. The gamma source provided a uniform absorption dose rate of 0.8 Gy/s in the water samples at the time of this study. The samples were all irradiated at room temperature. Samples were irradiated for 10, 20, 40, 60, 120, 180, 240, and 300 minutes in order to study the kinetics of the reaction. The time after the samples were irradiated, but before they were analyzed was minimized to control for the escape of some of the irradiation products such as hydrogen and oxygen.

6.2.3. Sample Analysis

6.2.3.1. Gas Chromatography

After irradiation the headspace in the vials were sampled using an air-tight syringe with Luer lock at all time points. This was done in order to get the concentrations of both gaseous oxygen and hydrogen which are generated by water radiolysis.

6.2.3.2. UV Vis Spectroscopy

At all-time points, a direct UV absorption spectra was obtained for the irradiated solution with no preparation. In addition to this the Ferrozine method was used to determine the iron speciation of the sample. In this method, an aliquot of the sample at all time points was mixed with a Ferrozine reagent. The volume of the aliquot varied with the initial iron concentration used. Ferrozine complexes with any $\text{Fe}^{2+}_{(\text{aq})}$ in the solution to produce a complex with an absorbance at 563 nm which has a molar extinction coefficient of $27900 \text{ M}^{-1}\text{cm}^{-1}$. Beer-Lambert's law is then used to determine the $[\text{Fe}^{2+}]$ in the solution. Following this, another aliquot is reduced using hydroxylamine which reduces the Fe^{III} species (both solids and in solution) to $\text{Fe}^{2+}_{(\text{aq})}$. This is then mixed with the Ferrozine reagent in order to determine the total concentration of iron in the system. The $[\text{Fe}^{\text{III}}]$ is then determined by taking the difference between these [1].

6.2.3.3. pH

Samples irradiated for all time points had their pHs taken using a pH meter (Mettler Toledo).

6.2.3.4. Transmission Electron Microscopy

The particles were collected by dipping a carbon-coated copper grid into the irradiated test solution and drying the sample grid in air. The TEM images were obtained with the electron microscope with electrons accelerated to 80 keV.

6.2.3.5. Fourier Transform Infrared Spectroscopy (FTIR)

Particles were collected from samples irradiated for 300 minutes. The samples were collected and centrifuged. This was then left on a glass slide to dry. Once dry, the resultant particles were incorporated into the KBr pellet for the FTIR measurement. FTIR spectroscopy measurements of the iron nanoparticles were performed using an IR spectrophotometer (Bruker Vertex 70v) with Fourier transformation (Bruker) in the 4000 to 400 cm^{-1} frequency range.

6.2.3.6. Raman Spectroscopy

Particles were collected from samples irradiated for 300 minutes. The samples were collected and centrifuged. This was then left on a glass slide to dry. Raman scattering measurements to determine the particle oxide composition were performed using a Renishaw model 2000 Raman Spectrometer with a laser excitation wavelength of 633 nm.

6.2.3.7. Computer Modelling

Modelling was performed as discussed in Chapter 3. All relevant water radiolysis reactions were modelled as well as the oxidation of ferrous iron by hydroxyl radicals (6.1) and the reduction of ferric iron by the solvated electron (R 6.2) [2, 3].



In order to effectively model the data, the reactions of nitrous oxide with the solvated electron (R 6.3) and t-butanol with the hydroxyl radical (6.4) were input into the model.



These reactions were necessary to input because even in the presence of the scavengers, trace amounts of the redox active species will remain in the system [4].

The model is designed specifically to understand in detail the homogenous kinetics of the system occurring in the initial stage of the nanoparticle formation. Once the particles nucleate, heterogeneous oxidation is expected to become significant which this model does not effectively simulate.

6.3. RESULTS

6.3.1. Observed Kinetic Behaviour in Different Scavenging Solution Environments

The kinetics of iron-oxide particle formation and growth were followed by simultaneously analyzing: (1) the concentrations of Fe^{2+} and Fe^{III} dispersed in the solution using the ferrozine method ($[\text{Fe}^{2+}]$ and $[\text{Fe}^{\text{III}}]$), (2) the UV-Vis absorbances at 304 nm and 380 nm of the solution, (3) the pH of solution, (4) the gaseous concentration of H_2 in the headspace ($[\text{H}_{2(\text{g})}]$), and (5) the size and shape of the particles formed by TEM imaging. In addition, the Raman spectra of the particles formed after 5-h irradiation were also obtained.

The kinetic data obtained for the 0.5 mM $[\text{Fe}^{2+}]_0$ solutions with different scavengers are compared for the solution and gas analysis data in Figure 6.1, and for the TEM images

and the Raman spectra of the particles in and Figure 6.2 and Figure 6.3, respectively. The results for the scavenger-free solutions presented here are from replicated experiments and their kinetic behaviors are consistent with those previously reported in Chapter 4.

In a given scavenging solution environment, the time dependent behaviours of the solution and gas analyses collectively show three distinct kinetic stages. The durations of these stages are indicated by bars on the tops of the kinetic plots. In each stage, the conversion of Fe^{2+} to Fe^{III} species is accompanied by increases in A_{304} and A_{380} , a decrease in pH (or increase in $\Delta[\text{H}^+]$) and an increase in $[\text{H}_{2(\text{g})}]$. However, the rates of changes in the measured quantities are different in different kinetic stages.

Stage 1 has a very short duration and, compared to other stages, is characterized by the fastest increases in $[\text{Fe}^{\text{III}}]$, A_{304} and A_{380} , and $\Delta[\text{H}^+]$ but a negligible production of $[\text{H}_{2(\text{g})}]$. The changes in $[\text{Fe}^{\text{III}}]$, A_{304} and A_{380} , and $\Delta[\text{H}^+]$ in Stage 1 all become faster as the scavenging environment changes from a t-butanol to a scavenger-free and to a N_2O saturated solution. The scavenging environment also affects the duration of Stage 1, shortest in a N_2O saturated solution and longest in a t-butanol solution.

As the reaction kinetics moves to Stage 2, the conversion of Fe^{2+} to Fe^{III} occurs at a slower rate. The decrease in the conversion rate coincides with the slower increases in A_{304} and A_{380} and $\Delta[\text{H}^+]$. On the other hand, the $\text{H}_{2(\text{g})}$ production rate is higher in Stage 2 than in Stage 1. As observed for Stage 1, the rates of increases in $[\text{Fe}^{\text{III}}]$, A_{304} and A_{380} , and $\Delta[\text{H}^+]$ in Stage 2 all become faster as the scavenging environment changes from a t-butanol, a scavenger-free to a N_2O saturated solution. Stage 3 begins after ~130-min irradiation, independent of scavenging environment. The rates of changes in $[\text{Fe}^{\text{III}}]$, A_{304} , $[\text{H}^+]$ and $[\text{H}_{2(\text{g})}]$ are much slower in Stage 3 than in the two earlier stages.

The Fe^{2+} to Fe^{III} conversion yields at the end of Stage 2 are less than 20% in a *t*-butanol solution and 60-65% in a scavenger-free solution. In a N_2O solution, nearly 100% conversion is achieved within 25 min, after which no significant changes in $[\text{Fe}^{\text{III}}]$, A_{304} and A_{380} , $[\text{H}^+]$ and $[\text{H}_{2(\text{g})}]$ occur until Stage 3 begins. Interestingly, in a N_2O solution the $[\text{Fe}^{\text{III}}]$ also slowly decreases with time in Stage 3. The final yields for Fe^{III} at 300 min in a scavenger-free and a N_2O solution appears to approach the same value of ~80%. These observations may suggest that the redox reactions between Fe^{2+} and Fe^{III} species approach quasi-equilibrium states at long times, and that the steady-state concentrations of Fe^{2+} and Fe^{III} depend mainly on $[\text{Fe}^{2+}]_0$ in Stage 3, see discussion in Section 6.4.2.

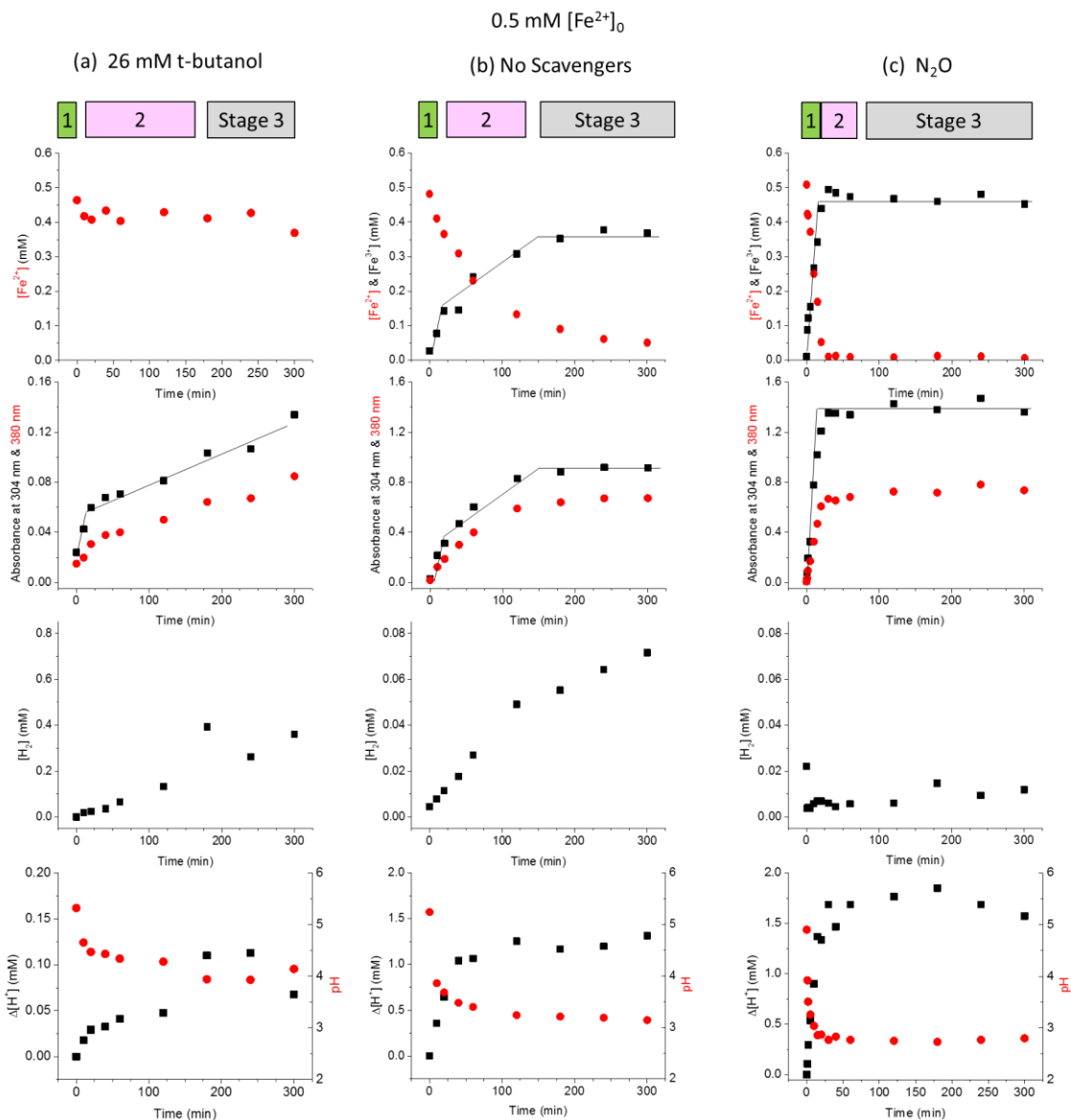


Figure 6.1: Kinetic behaviours observed during radiolytic conversion of dissolved ferrous ions to iron oxide/hydroxide nanoparticles for 0.5 mM $[\text{Fe}^{2+}]_0$ solutions containing different scavengers, (a) 26 mM t-butanol, (b) free of scavenger and (c) N_2O . Four different sets of kinetic data are shown from the top to bottom: $[\text{Fe}^{2+}]$ and $[\text{Fe}^{\text{III}}]$ determined by the ferrozine method, the UV-vis absorbances at 304 nm and 380 nm, pH (or $\Delta[\text{H}^+]$) and $[\text{H}_{2(\text{g})}]$ in the headspace. The three kinetics stages are indicated by the bars at the top of each data set.

The TEM images of the particles formed as a function of irradiation time in 0.5 mM $[\text{Fe}^{2+}]_0$ solutions with different scavengers are compared in Figure 6.2. The changes in particle morphology also reflect different kinetic stages observed from the solution and gas

analyses. The TEM images of the particles formed after 10-min irradiation show two areas with different shades. The darker areas contain well-defined, denser particles of 20-30 nm in size. The lighter areas are made up of small spherical particles which appear to have aggregated. The light particles are nearly absent after 10-min irradiation of a N₂O solution whose solution and gas kinetic data show the duration of Stage 1 shorter than 3 min.

The individual lighter spherical particles that form the gel-like aggregates become denser with time. They also appear to lose the tendency to aggregate with time and the TEM images show more of denser individual particles. The particles become denser earlier as the scavenging environment changes from a t-butanol, to a scavenger-free and a N₂O solution. The densest or the darkest particles grow into size of 25 ± 5 nm with a narrow size distribution by the end of Stage 2. The average size of these particles is independent of scavenging environment, and it was also observed independent of $[\text{Fe}^{2+}]_0$ in scavenger-free solutions.

Scavenging environment has the most effect on the size of particles that form in Stage 3. In a t-butanol solution the aggregates made of lighter particles are persistent even at 300 min. In a scavenger-free solution, the small denser particles appear to have undergone Ostwald ripening to form larger dendritic particles of 80-100 nm in size at 300 min. In a N₂O solution the sign of Ostwald ripening occurring can be seen in the TEM image taken at 60 min (near the end of Stage 2) but the contribution of Ostwald ripening in controlling particle size appears to be small.

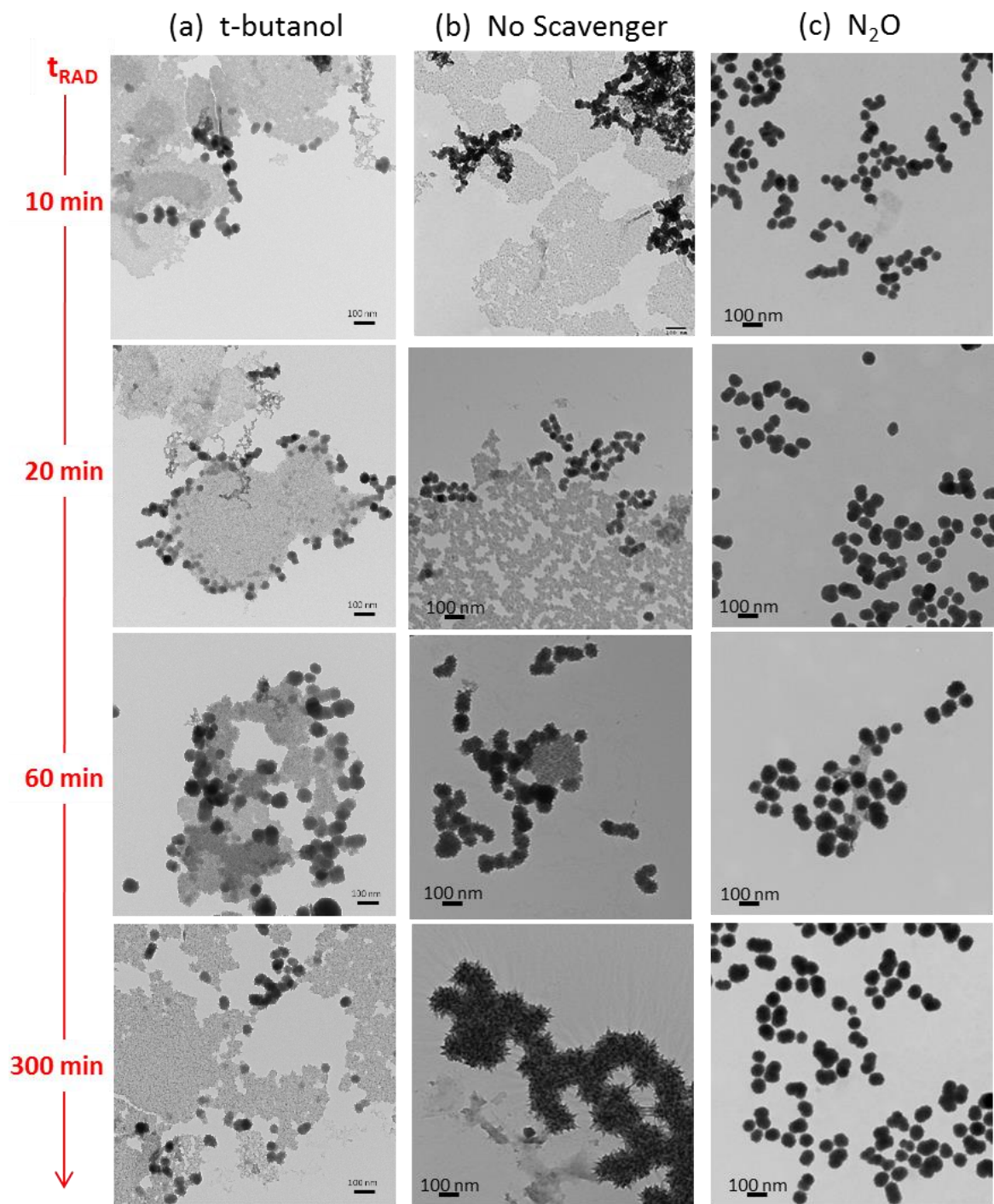


Figure 6.2: TEM images of the particles formed as a function of irradiation time in solutions containing 0.5 mM $[\text{Fe}^{2+}]_0$ with a different scavenger, (a) 26 mM t-butanol, (b) free of scavenger and (c) N₂O.

The Raman spectra of the particles formed after 5-h irradiation in 0.5 mM $[\text{Fe}^{2+}]_0$ solutions with different scavengers are presented in Figure 6.3 along with reference spectra taken with standard powder samples of different iron oxides. The spectra of the particles show Raman shifts at $\sim 250, 350, 420, 500, 600$ and 700 cm^{-1} whose relative intensities vary depending on scavenging environment. We have previously reported on the Fe K-edge total electron yield (TEY) and the X-ray fluorescence yield (FLY) XANES (x-ray absorption near edge spectroscopy) and the FTIR spectra in addition to the Raman spectra of the particles formed after 5-h irradiation in scavenger-free solutions containing different $[\text{Fe}^{2+}]_0$ (Chapter 4). By comparing with the XANES and FTIR as well as with the reference spectra of iron hydroxides/oxides we assign the Raman peaks as follows. The Raman peaks contributing the broad band over $250\text{-}500 \text{ cm}^{-1}$ to the vibrational modes associated with the $\text{Fe}^{\text{III}} - \text{OH}$ and $\text{Fe}^{\text{III}} - \text{O}$ bonds, while those over 600 to 800 cm^{-1} to the vibrational modes of a mixed $\text{Fe}^{\text{II}}/\text{Fe}^{\text{III}} - \text{O}$ in spinel oxides ($\text{Fe}_3\text{O}_4/\gamma\text{-Fe}_2\text{O}_3$) [5, 6].

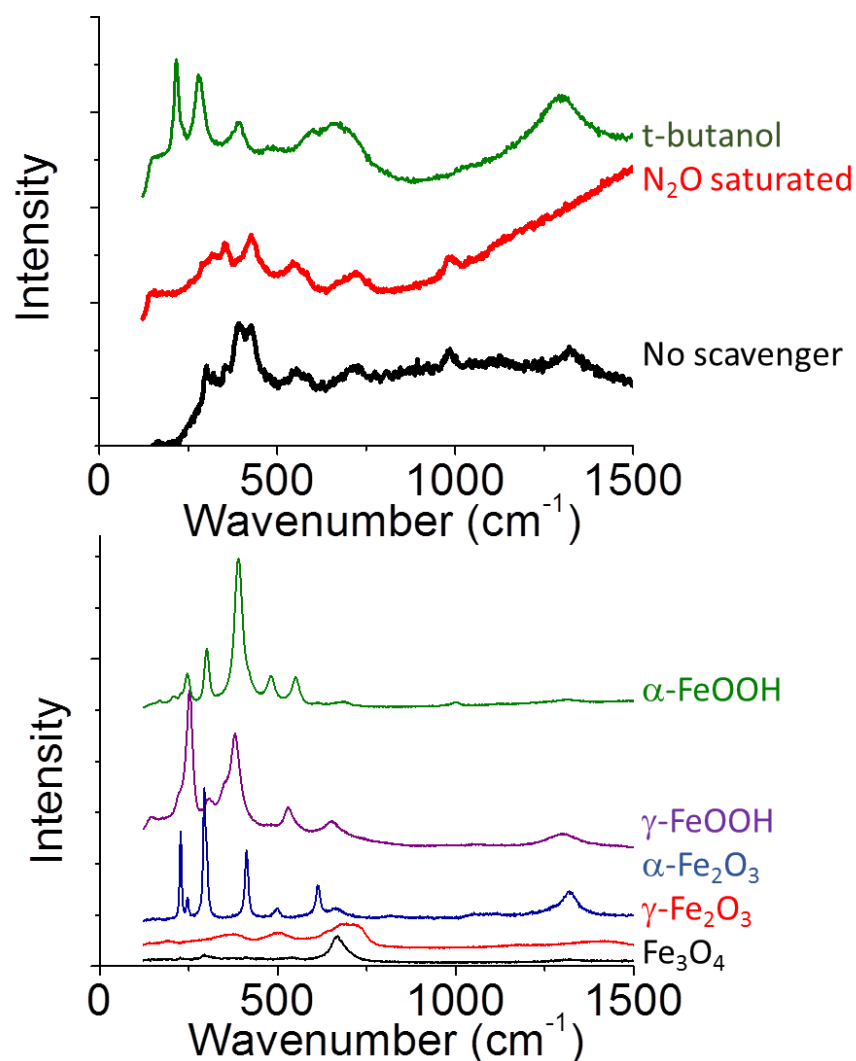


Figure 6.3: Raman spectra of the particles formed after 5-h irradiation in 0.5 mM $[\text{Fe}^{2+}]_0$ solutions with different scavengers. Shown below are the reference spectra taken with standard powder samples of different iron oxides.

The relative intensities of the peaks associated with the spinel oxides to those associated with ferric hydroxides and oxides are the largest for the particles formed in a N_2O solution and the smallest in a t-butanol solution. The Raman intensity at 420 cm^{-1} relative to that of 700 cm^{-1} was also observed to increase with $[\text{Fe}^{2+}]_0$ in a scavenger-free solution. These observations are consistent with the particle growth mechanism that the

mixed Fe^{II}/Fe^{III} hydroxides formed on the surfaces of growing particles are slowly dehydrated and transformed into oxyhydroxides and then to oxides, and the particles grow as Fe₃O₄ (magnetite) in the core with their surfaces hydrated and hydrolyzed in varying degrees:



The irradiated solution environment becomes more oxidizing from a t-butanol, scavenger-free to a N₂O saturated solution. The observation that the higher intensities of the peaks associated with the spinel oxides relative to those associated with ferric hydroxides in a more oxidizing solution is consistent with the expectation that the mixed Fe^{II}/Fe^{III} hydroxide and oxyhydroxide will be formed faster and they will convert to magnetite faster in a more oxidizing environment, see Section 6.4.1.

The faster formation of magnetite in the core with an hydroxide/oxyhydroxide outer layer in a more oxidizing environment is consistent with the observed time evolutions of A₃₀₄ and A₃₈₀ (Figure 6.1). In the previous study we attributed the two UV-Vis absorption bands centred at 304 and 380 nm to electronic transitions associated mostly with the Fe^{III} – OH bonding and the spinel Fe^{II}/Fe^{III} – O bonding, respectively (Chapter 3 for full discussion). The ratio of the absorbances is nearly constant in Stage 1 and Stage 2, but increases with time in Stage 3. These time-dependent behaviours are consistent with particles that grow as spinel oxide in the core and an outer layer of Fe^{II}/Fe^{III} that is hydrated and hydrolysed, and the ratio of A₃₈₀ to A₃₀₄ increases with time. The ratio will also be higher for the particles having a higher fraction of inner spinel oxide. This is consistent with the observations that the ratio is higher in a higher [Fe²⁺]₀ solution and is higher in a more oxidizing solution (Figure 6.1).

6.3.2. Effect of $[\text{Fe}^{2+}]_0$ on Particle Growth in N_2O Saturated Solutions

The solution and gas analysis kinetic measurements obtained for the N_2O saturated solutions containing different $[\text{Fe}^{2+}]_0$ are compared in Figure 6.4, and the TEM images of the particles in Figure 6.5 and Figure 6.6. At all $[\text{Fe}^{2+}]_0$, the three kinetic stages described above are present. In Stage 1 the rate of conversion from Fe^{II} to Fe^{III} ($\Delta[\text{Fe}^{\text{III}}]/\Delta t$) is very fast. Due to the fast rate the near 100% conversion is reached in Stage 1 in a 0.1 mM $[\text{Fe}^{2+}]_0$ solution.

In Stage 2, the rates, $\Delta[\text{Fe}^{\text{III}}]/\Delta t$ and $\Delta[\text{H}^+]/\Delta t$, are nearly proportional to $[\text{Fe}^{2+}]_0$ (except for 0.1 mM $[\text{Fe}^{2+}]_0$ due the near 100% conversion in Stage 1). The rate of production of $\text{H}_{2(\text{g})}$ also increases with $[\text{Fe}^{2+}]_0$. Because the rate of conversion of Fe^{2+} to Fe^{III} is faster in a N_2O solution than in a scavenger-free solution, near 100% conversion of $[\text{Fe}^{2+}]_0$ to Fe^{III} occurs early before Stage 3 begins in N_2O solutions. The onset of Stage 3 occurs approximately same time (~ 130 min), independent of $[\text{Fe}^{2+}]_0$. In Stage 3 Fe^{III} reduces back to Fe^{II} and the ratio of $[\text{Fe}^{\text{III}}]$ to $[\text{Fe}^{2+}]$ reaches a steady state value. The steady state ratio, or the final oxidation yield, decreases with increasing $[\text{Fe}^{2+}]_0$.

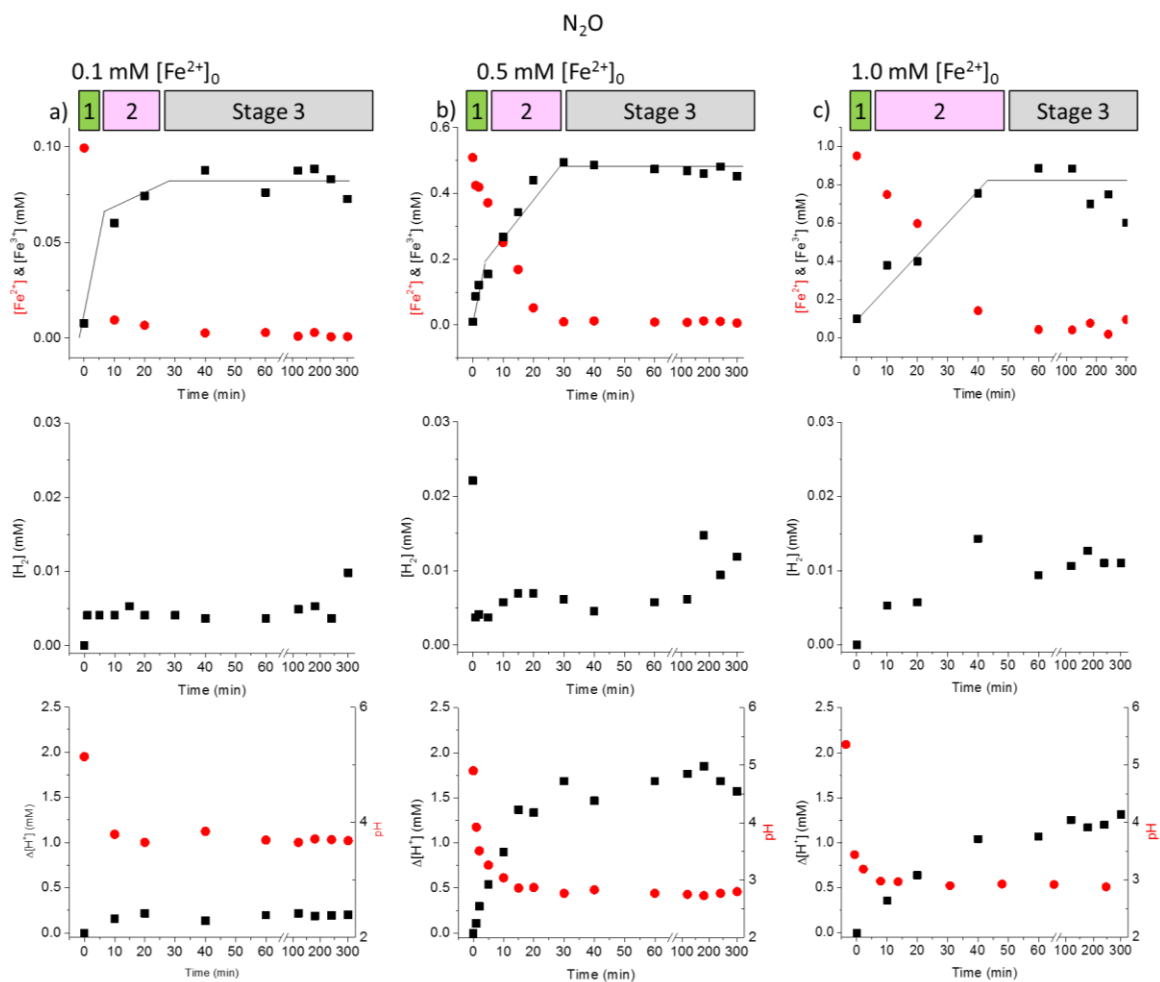


Figure 6.4: Kinetic behaviours observed during radiolytic conversion of dissolved ferrous ions to iron oxide/hydroxide nanoparticles in N₂O saturated solutions containing (a) 0.1 mM [Fe²⁺]₀, (b) 0.5 mM [Fe²⁺]₀ and (c) 1.0 mM [Fe²⁺]₀. Three different sets of kinetic data are shown from the top to bottom: [Fe^{II}] and [Fe^{III}] determined by the ferrozine method, [H_{2(g)}] in the headspace, and pH (or Δ[H⁺]). The three kinetics stages are indicated by the bars at the top of each data set. Note that the data are presented in two different time scales to show the changes observed in Stages 1 and 2 more clearly.

The TEM images of the particles formed after different irradiation times for 0.1 mM and 1.0 mM [Fe^{2+(aq)}]₀ with or without N₂O are presented in Figure 6.5 and Figure 6.6 respectively. In a 0.1 mM [Fe^{2+(aq)}]₀ solution both the aggregates made of very light spherical particles and the well-defined, denser particles of ~10 nm in size are present after 20-min irradiation. The aggregates made of the light particles disappears and the individual

particles become denser with longer irradiation. The particles become denser faster in a N_2O solution, and the densest particles of 25 ± 5 nm in size were formed only in a N_2O solution.

The particles that forms aggregates after 20-min irradiation are denser in a 1.0 mM $[\text{Fe}^{2+}]_0$ solution than in the lower $[\text{Fe}^{2+}(\text{aq})]_0$ solutions. As observed in a 0.5 mM $[\text{Fe}^{2+}]_0$ solution, the individual particles become denser and lose the tendency to aggregate with time, and these changes in short times (Stage 1 and 2) are faster in a N_2O solution than in a scavenger-free solution. However, in a N_2O solution the duration of Stage 2 is shorter, and in Stage 3 the particles do not grow as large as those observed in the absence of N_2O .

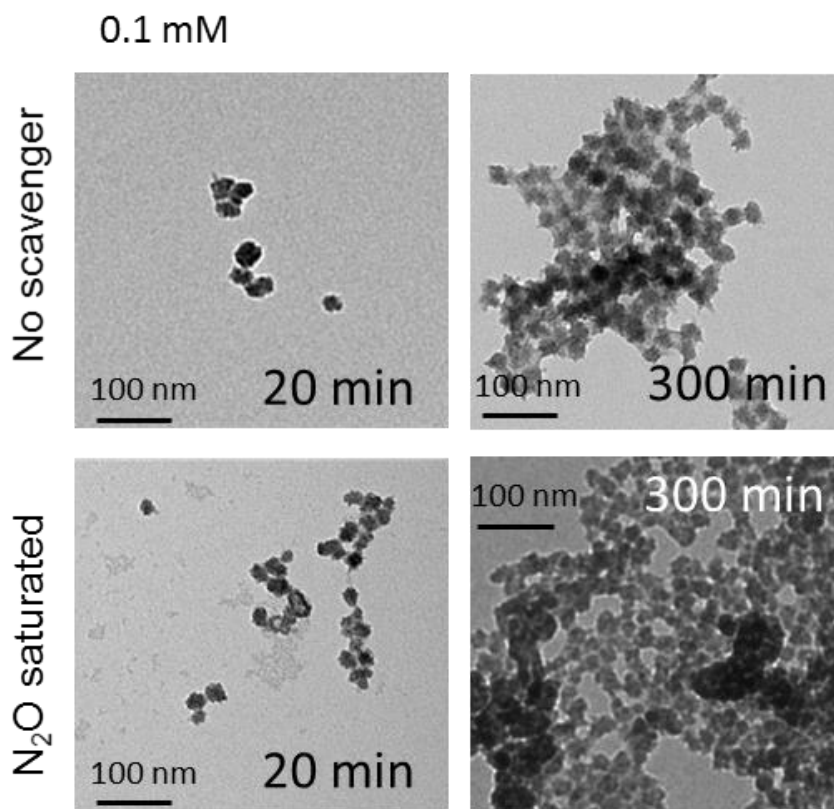


Figure 6.5: TEM images of the particles collected following γ -irradiation for different durations of 0.1 mM $[\text{Fe}^{2+}]_0$ solution with or without N_2O . Irradiation times are indicated above the images.

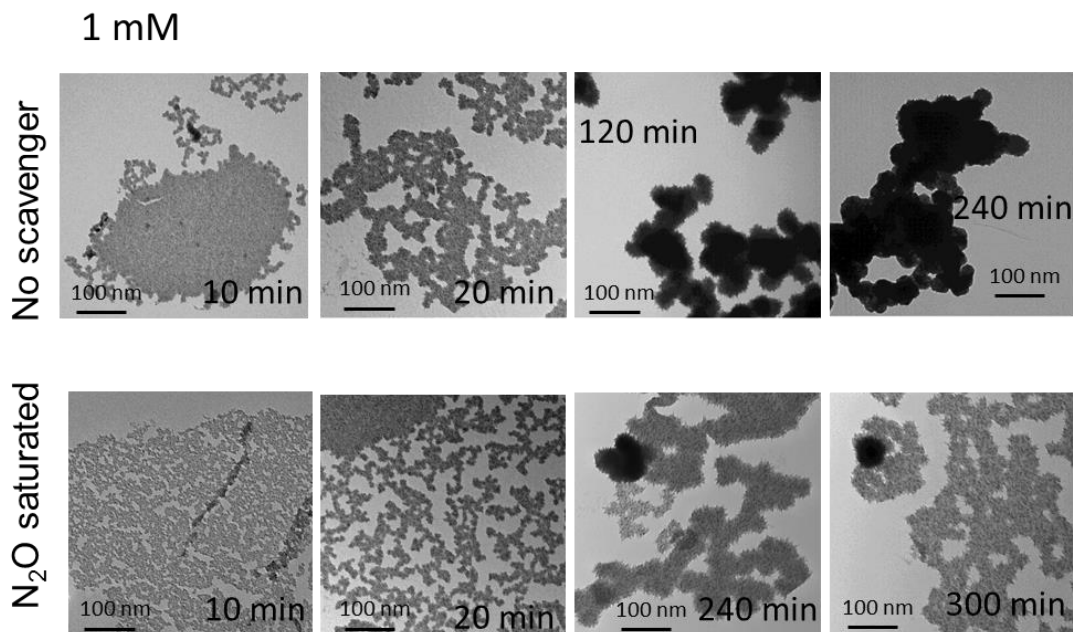


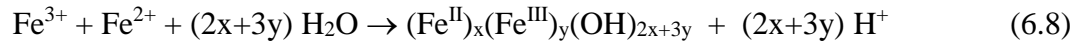
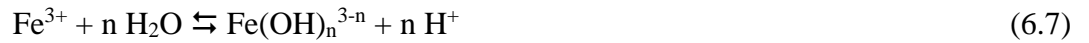
Figure 6.6: TEM images of the particles collected following γ -irradiation for different durations of 1 mM $[\text{Fe}^{2+}]_0$ solution with or without N_2O . Irradiation times are indicated above the images.

6.4. DISCUSSION

6.4.1. Mechanism of Particle Formation and Growth

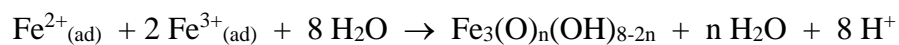
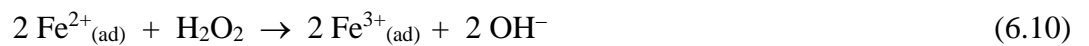
Previous studies in scavenger-free solutions have shown that iron-oxide nanoparticle formation and growth by γ -radiolysis of solutions initially containing dissolved ferrous ions undergo three distinct kinetic stages, and that the $[\text{Fe}^{2+}]_0$ affects the oxidation kinetics of the different stages differently [7]. By investigating how $[\text{Fe}^{2+}]_0$ affects the kinetics of different stages we were able to establish the dependences of oxidation yield and particle size on $[\text{Fe}^{2+}]_0$ and to propose a mechanism that could explain the observed dependences. As discussed in more details below the results from the current study on the effect of radical scavengers are consistent with the previously proposed mechanism and hence, the mechanism is first summarized below. A schematic of this mechanism is presented in Chapter 4.

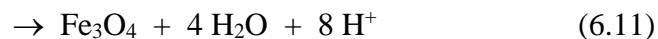
The main processes that control the kinetics in Stage 1 are the aqueous oxidation of Fe^{2+} to less soluble Fe^{3+} by radiolytically-produced $\bullet\text{OH}$, followed by hydrolysis of Fe^{3+} to form Fe^{III} hydroxide species. The formation of Fe^{III} hydroxides triggers co-precipitation of ferrous and ferric ions with hydroxide ions as mixed $\text{Fe}^{\text{II}}/\text{Fe}^{\text{III}}$ hydroxides, forming nucleate particles:



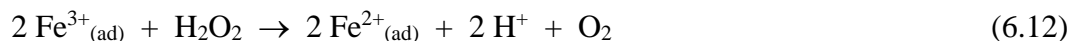
where Fe^{3+} represents all of hydrated ferric species ($\text{Fe}^{3+}_{(\text{aq})}$, $\text{Fe}(\text{OH})^{2+}_{(\text{aq})}$, $\text{Fe}(\text{OH})^{+}_{(\text{aq})}$, and $\text{Fe}(\text{OH})_{4-}_{(\text{aq})}$) and Fe^{2+} represents all of hydrated ferrous species ($\text{Fe}^{2+}_{(\text{aq})}$, $\text{Fe}(\text{OH})^{+}_{(\text{aq})}$, and $\text{Fe}(\text{OH})_{3-}_{(\text{aq})}$). In a pH range between 3.0 and 6.0 the predominant form of ferrous species is $\text{Fe}^{2+}_{(\text{aq})}$ while that of ferric species is $\text{Fe}(\text{OH})^{2+}_{(\text{aq})}$ (near pH 3.0) and/or $\text{Fe}(\text{OH})^{+}_{(\text{aq})}$ (near pH 6.0) [8].

In Stage 2, while the radiolysis-induced particle nucleation continues the dominant process is the adsorption of ferrous ions on the existing particles, followed by surface oxidation of the $\text{Fe}^{2+}_{(\text{ad})}$ to $\text{Fe}^{3+}_{(\text{ad})}$. The adsorbed $\text{Fe}^{2+}_{(\text{ad})}$ and $\text{Fe}^{3+}_{(\text{ad})}$ are then incorporated into the growing particles and the oxide particles slowly transform into a specific oxide phase(s). Molecular radiolysis product H_2O_2 is the more effective oxidant than $\bullet\text{OH}$ for surface oxidation. The dominant processes that control the overall oxidation of ferrous to ferric species in Stage 2 include:





In Stage 3, Fe^{III} has accumulated to a substantial level and its reduction by H_2O_2 becomes important:



This reaction, coupled with the oxidation of Fe^{II} by H_2O_2 (reaction 6.10), establishes a redox cycle that maintains a quasi-equilibrium between Fe^{II} and Fe^{III} in Stage 3. As the redox cycle continues the ferrous and ferric ions also continuously desorb from and adsorb on particles:



The overall result is negligible net oxidation but growth of particles by the Ostwald ripening accelerated by continuous radiolytic production of $\bullet\text{OH}$ and H_2O_2 in Stage 3.

The results from this study are also consistent with the mechanism. However, the radical scavengers affect the concentrations of radiolytically produced redox active species, and this affects the overall kinetics of the solution-particle interfacial process and the final size of the nanoparticles formed. The effect of N_2O and t-butanol on the time evolution of radiolysis product concentrations is thus discussed first.

6.4.2. Effect of Radical Scavengers on Radiolysis Product Concentrations

Computation modelling results obtained using the γ -radiolysis model are presented in Figure 6.7. In deaerated solutions free of a scavenger and Fe^{2+} , the concentrations of the primary radiolysis products at very short times (< 1 ms) after the start of irradiation increase linearly with time (i.e., the slope of the log-log plot is 1). These times are too short for

solution reactions to occur at substantial rates and the production of a primary radiolysis product at short times can be approximated by the radiation dose rate and the species g-value, e.g.,

$$\frac{d[\bullet\text{OH}]_t}{dt} \approx G_{\bullet\text{OH}} \cdot D_R \cdot \rho_w \quad (6.15a)$$

$$[\bullet\text{OH}]_t \approx G_{\bullet\text{OH}} \cdot D_R \cdot \rho_w \cdot t \quad (6.15b)$$

where $G_{\bullet\text{OH}}$ is the g-value for $\bullet\text{OH}$ in units for $\mu\text{mol}\cdot\text{J}^{-1}$, D_R is the radiation dose rate in units of $\text{Gy}\cdot\text{s}^{-1}$ ($\text{J}\cdot\text{kg}^{-1}\cdot\text{s}^{-1}$), and ρ_w is the density of water ($\text{kg}\cdot\text{L}^{-1}$). Similarly, $[\bullet\text{e}_{\text{aq}}^-]$ increases linearly with time in a deaerated solution at pH 6 (Figure 6.7):

$$[\bullet\text{e}_{\text{aq}}^-]_t \approx G_{\bullet\text{e}_{\text{aq}}^-} \cdot D_R \cdot \rho_w \cdot t \quad (6.16)$$

where $G_{\bullet\text{e}_{\text{aq}}^-}$ is the g-value for $\bullet\text{e}_{\text{aq}}^-$.

Under continuous irradiation the changes in the concentrations of primary radiolysis products quickly deviate from the linear increases as their concentrations accumulate and the rates of their solution reactions increase. The more chemically reactive a radiolysis product is, the faster its concentration reaches steady state and the lower its steady-state concentration is. At longer times (> 1 s), the concentrations of secondary radiolysis products such as O_2 also reach high levels and start influencing the radiolysis kinetics. More detailed discussion on the kinetics of continuous γ -radiolysis of water can be found elsewhere [2, 9].

In the presence of $[\text{Fe}^{2+}]_0$, $[\bullet\text{OH}]$ reaches a steady-state value faster due to the additional removal of $\bullet\text{OH}$ via reaction 6.1. On the other hand, the reaction of Fe^{3+} with $\bullet\text{e}_{\text{aq}}^-$ (reaction 6.2) cannot compete with the reaction of H^+ for $\bullet\text{e}_{\text{aq}}^-$, especially at low pHs.

Hence, $[\text{Fe}^{2+}]_0$ has a negligible effect on $[\bullet\text{e}_{\text{aq}}^-]$ at short times (< 0.1 s). Under these conditions $[\bullet\text{OH}]_{\text{SS}}$ and $[\text{Fe}^{3+}]_t$ can be approximated as:

$$[\bullet\text{OH}]_{\text{SS}} \approx \frac{G_{\bullet\text{OH}} \cdot D_R \cdot \rho_w}{k_{\text{Fe}(2+) \rightarrow \bullet\text{OH}} \cdot [\text{Fe}^{2+}]_0} \quad (6.17)$$

$$-\frac{d[\text{Fe}^{2+}]_t}{dt} = \frac{d[\text{Fe}^{3+}]_t}{dt} \approx k_{\text{Fe}(2+) \rightarrow \bullet\text{OH}} \cdot [\bullet\text{OH}] \cdot [\text{Fe}^{2+}]_0 \quad (6.18)$$

$$[\text{Fe}^{3+}]_t \approx G_{\bullet\text{OH}} \cdot D_R \cdot \rho_w \cdot t \quad (6.19)$$

These approximate solutions are confirmed by the computational calculation results presented in Figure 6.7.

The radiolysis kinetic analysis shows that in a scavenger-free solution the radiolytic production of $\bullet\text{OH}$ controls the rate of production of Fe^{3+} over a short irradiation period (< 1 s) and that this rate is independent of $[\text{Fe}^{2+}]_0$. This rate is $\sim 0.22 \mu\text{M}\cdot\text{s}^{-1}$ at the studied dose rate of $0.8 \text{ Gy}\cdot\text{s}^{-1}$ (see Table 6.1). At this rate the concentration of ferric ions quickly (in less than 10 ms) reaches its saturation limit ($\sim 10^{-2}$ nM at pH 6.0 [10]) in the solutions free of scavengers.

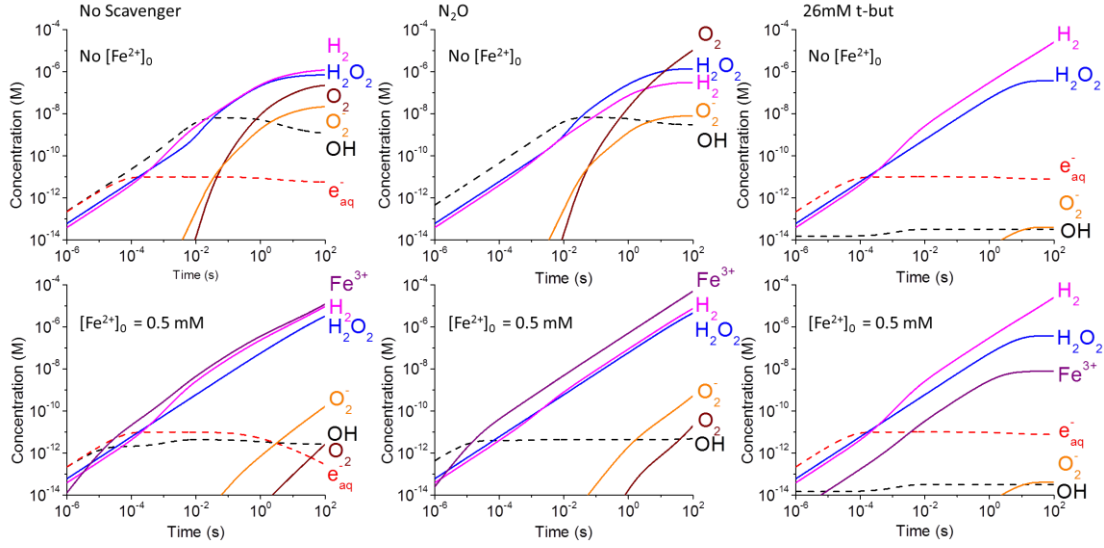


Figure 6.7: Calculated concentrations of radiolysis products as a function of irradiation time for deaerated solutions at pH 6.0, (a) free of a scavenger, (b) saturated with N_2O or (c) with t-butanol (0.026 M). The top row presents the results for the solutions free of iron species and the bottom row presents those for the solutions initially containing 0.5 mM $[Fe^{2+}]_0$ under the same scavenging conditions. Only the key radiolysis products critical to the formation of the iron nanoparticles are illustrated here, though many others are present.

The addition of N_2O affects $[•e_{aq}^-]$ and $[•OH]$ strongly due to reaction 6.3 which is the main removal reaction path for $•e_{aq}^-$ at $pH > 2$. Because of the near-diffusion limited rate of reaction 6.3, $[•e_{aq}^-]$ reaches steady state nearly instantly. The rate equation for $[•e_{aq}^-]$ in an N_2O saturated solution at early times and the $[•e_{aq}^-]_{SS}$ can be approximated as:

$$\frac{d[•e_{aq}^-]_t}{dt} \approx G_{•e_{aq}^-} \cdot D_R \cdot \rho_w - k_{•e_{aq}^-N_2O} \cdot [N_2O] \cdot [•e_{aq}^-]_t \quad (6.20)$$

$$[•e_{aq}^-]_{SS} \approx \frac{G_{•e_{aq}^-} \cdot D_R \cdot \rho_w}{k_{•e_{aq}^-N_2O} \cdot [N_2O]} \quad (6.21)$$

where $k_{•e_{aq}^-N_2O}$ is the rate constant for the reaction of N_2O and $•e_{aq}^-$.

Reaction 6.3 contributes to the production of $•OH$ in addition to the primary radiolytic decomposition of water. Thus, the rate equation for $[•OH]$ at short times (< 10 ms) before the solution reactions of $•OH$ with other radiolysis products occur at substantial rates can be approximated as:

$$\frac{d[\bullet\text{OH}]_t}{dt} \approx G_{\bullet\text{OH}} \cdot D_R \cdot \rho_w + k_{\bullet\text{e}_{\text{aq}}^- \text{N}_2\text{O}} \cdot [\text{N}_2\text{O}] \cdot [\bullet\text{e}_{\text{aq}}^-]_{\text{SS}} \quad (6.22)$$

$$[\bullet\text{OH}]_t \approx (G_{\bullet\text{OH}} + G_{\bullet\text{e}_{\text{aq}}^-}) \cdot D_R \cdot \rho_w \cdot t \quad \text{at } t < 10 \text{ ms} \quad (6.23)$$

The g-values for $\bullet\text{OH}$ and $\bullet\text{e}_{\text{aq}}^-$ are nearly the same. That is, the overall rate of $\bullet\text{OH}$ production at short times in the presence of N_2O is twice that in a solution free of N_2O .

In a N_2O saturated solution the rate equation (equation 6.3) thus yields the production rate of ferric ions at short times (< 10 ms) as:

$$[\text{Fe}^{3+}]_t \approx (G_{\bullet\text{OH}} + G_{\bullet\text{e}_{\text{aq}}^-}) \cdot D_R \cdot \rho_w \cdot t \quad (6.24)$$

That is, the radiolysis kinetic analysis indicates that the rate of production of Fe^{3+} at times $> 10 \mu\text{s}$ in the N_2O saturated solution is twice that in a solution free of N_2O , and the concentration of ferric ions reaches its saturation limit at a twice faster rate in the N_2O saturated solution. This rate is $\sim 0.44 \mu\text{M}\cdot\text{s}^{-1}$ at the studied dose rate of $0.8 \text{ Gy}\cdot\text{s}^{-1}$ (see Table 6.1).

Tertiary-butanol reacts with $\bullet\text{OH}$ (reaction 6.4). Due to the fast rate of reaction (6.4) the $[\bullet\text{OH}]$ in a t-butanol solution reaches steady state within 1 ms and the $[\bullet\text{OH}]_{\text{SS}}$ is very low. Following the similar kinetic analysis, $[\bullet\text{OH}]_{\text{SS}}$ in the absence of Fe^{2+} is,

$$[\bullet\text{OH}]_{\text{SS}} \approx \frac{G_{\bullet\text{OH}} \cdot D_R \cdot \rho_w}{k_{\bullet\text{OH}-\text{butanol}} \cdot [\text{butanol}]_0} \quad \text{at } t < 1 \text{ ms} \quad (6.25)$$

where $k_{\bullet\text{OH}-\text{butanol}}$ is the rate constant for the reaction of t-butanol and $\bullet\text{OH}$ (reaction 6.4). Because $[\bullet\text{OH}]$ reaches steady state nearly immediately the rate of Fe^{3+} production is no longer controlled by the primary radiolytic production of $\bullet\text{OH}$ even at short times. Instead the rate of Fe^{3+} production can be approximated by substituting $[\bullet\text{OH}]$ in equation (19) with $[\bullet\text{OH}]_{\text{SS}}$ defined in equation (6.25):

$$[Fe^{3+}]_t \approx k_{Fe(2+)\rightarrow\bullet OH} \cdot \frac{G_{\bullet OH} \cdot D_R \cdot \rho_w}{k_{\bullet OH-butanol} \cdot [butanol]_0} \cdot [Fe^{2+}]_0 \cdot t \quad (6.26)$$

That is, the radiolysis kinetic analysis indicates that the rate of production of Fe^{3+} in a 26 mM t-butanol solution at times < 1 s will be significantly lower than that in pure water (compare Figure 6.1a and Figure 6.1b). This rate is approximately $1.5 \text{ nM}\cdot\text{s}^{-1}$ in a 26 mM t-butanol solution at the studied dose rate of $0.8 \text{ Gy}\cdot\text{s}^{-1}$ (Table 6.1). This will significantly decrease the rate of particle nucleation as discussed in Section 6.4.1.

Table 6.1: Rate of hydroxyl radical production and time to reach saturation limit of Fe^{III} in the presence of various scavengers.

Scavenger	$\bullet OH$ Production Rate ($\mu\text{M}\cdot\text{s}^{-1}$)	Time to Reach Sat Limit (μs)
N_2O	4.4	7
None	2.2	14
t-butanol	0.0015	2000

6.4.3. Effects of $[Fe^{2+}]_0$ and Scavengers on Particle Nucleation and Growth

The main process that determines the short-term kinetics (Stage 1) is the solution-phase oxidation of Fe^{2+} to Fe^{3+} by radiolytically-produced $\bullet OH$. This is followed by hydrolysis of Fe^{3+} , which triggers co-precipitation of ferrous and ferric species as mixed Fe^{II}/Fe^{III} hydroxide particles (reaction 6.5). The radiolysis kinetic calculation results show that the rate of radiolytic production of Fe^{3+} in the solution phase is fastest in a N_2O/Ar saturated solution and slowest in a t-butanol solution (Table 6.1). This is consistent with the observed dependence of the rate of Fe^{II} to Fe^{III} conversion in Stage 1 on scavenging environment (Figure 6.1). A faster production of Fe^{3+} leads to a faster particle nucleation and a larger number of nucleate particles, which in general leads to the formation of particles with a narrow size distribution. The radiolysis kinetic analysis shows that increase in $[Fe^{2+}]_0$, however, does not affect the rate of Fe^{II} to Fe^{III} conversion in Stage 1. Thus, increase in

$[\text{Fe}^{2+}]_0$ will not affect the number of nucleate particles significantly, but it will affect the rate of adsorption of Fe^{2+} onto particles and hence the rate of oxidation of $\text{Fe}^{\text{II}}(\text{ad})$ by H_2O_2 in Stage 2.

In Stage 2 the particle nucleation continues but the dominant process is the continued adsorption of Fe^{II} onto existing particles, followed by the oxidation of $\text{Fe}^{\text{II}}(\text{ad})$ to grow mixed $\text{Fe}^{\text{II}}/\text{Fe}^{\text{III}}$ (spinel) oxide particles. For the solution oxidation in Stage 1 $\bullet\text{OH}$ is most effective. However, the molecular radiolysis product, H_2O_2 , is more effective than $\bullet\text{OH}$ for the oxidation on particle surfaces. We were not able to model the radiolysis kinetics at long time when the adsorption of $\text{Fe}^{2+}(\text{aq})$ onto and its oxidation on the growing particles is significant mostly because the kinetic parameters of the processes are not available. However, the radiolysis kinetic analysis suggests that $[\text{H}_2\text{O}_2]$ at longer times (> 10 ms) that is important for surface oxidation in Stage 2 will be also highest in a $\text{N}_2\text{O}/\text{Ar}$ saturated solution, higher in a solution free of scavengers than in a t-butanol solution. The formation of a larger number of particles in Stage 1 (and hence a larger total surface area) and the higher $[\text{H}_2\text{O}_2]$ leads to a significantly faster overall oxidation of Fe^{II} to Fe^{III} in a N_2O solution than in a scavenger-free solution.

In Stage 3, negligible net oxidation of Fe^{II} to Fe^{III} occurs, but Ostwald ripening of the particles by continuous dissolution and precipitation. Under irradiation Ostwald ripening is assisted by the redox cycle of Fe^{II} and Fe^{III} with H_2O_2 (reactions 6.10 and 6.12). The more conversion of Fe^{II} to Fe^{III} before Stage 3 begins will result in smaller particles.

6.5. SUMMARY

The effect of each of the two radical scavengers was explored to determine the importance of two key radiolytic species in the formation of iron oxide nanoparticles from

solution by irradiation with ionizing radiation. The first scavenger used was t-butanol in order to scavenge the hydroxyl radical. It was found that oxidation yield with t-butanol was severely decreased when compared to samples irradiated in the absence of t-butanol. The particle size was found to decrease with the addition of t-butanol. This effect is attributed to the diminished ability for the solution to oxidize iron which decreases the ability of particles to both nucleate and to grow. The presence of t-butanol greatly diminishes the ability to grow particles resulting in smaller particles as compared to samples in the absence of t-butanol. The composition of the particles changes with the addition t-butanol. Without a scavenger, a mixed oxyhydroxide grows with a magnetite core. Magnetite is the dominant form, but increasing the t-butanol concentration allows oxidation to occur more slowly and more stable oxides to embed within the Magnetite structure with γ -FeOOH (Lepidocrocite) grown with small amounts of t-butanol and α -Fe₂O₃ (Haematite) with greater amounts.

The second scavenger explored was N₂O which effectively scavenges against the solvated electron. It was found that iron in the system was oxidized both more quickly and more completely in the presence of N₂O than in its absence. This rapid oxidation resulted smaller and more compact particles that lost their dendritic character. The dendritic character of particles formed without the scavenger is attributed to rapid cyclization of the iron content. The composition of the particles in the presence of the N₂O is consistent with the particles formed in the absence of N₂O with some only slight alterations in the relative abundances of the oxides formed.

6.6. REFERENCES

- [1] L.L. Stookey, *Anal. Chem.*, 42 (1970) 779-781.
- [2] J.M. Joseph, B.S. Choi, P. Yakabuskie, J.C. Wren, *Radiat. Phys. Chem.*, 77 (2008) 1009-1020.

- [3] G.V. Buxton, C.L. Greenstock, W.P. Helman, A.B. Ross, *J. Phys. Chem. Ref. Data*, 17 (1988) 513-886.
- [4] J.C. Wren, in proceedings of ACS Symposium Series, Washington, DC, (2010).
- [5] J. Bessiere, M. Perdicakis, B. Humbert, *C.R. Acad. Sci., Ser. IIC: Chim.*, 2 (1999) 101-105.
- [6] S. Das, M.J. Hendry, *Chem. Geol.*, 290 (2011) 101-108.
- [7] P.A. Yakabuskie, J.M. Joseph, P. Keech, G.A. Botton, D. Guzonas, J.C. Wren, *Phys. Chem. Chem. Phys.*, 13 (2011) 7167-7175.
- [8] C.F. Baes, R.E. Mesmer, *The Hydrolysis of cations*, Wiley, New York, (1976).
- [9] P.A. Yakabuskie, J.M. Joseph, J.C. Wren, *Radiat. Phys. Chem.*, 79 (2010) 777-785.
- [10] CRC Handbook of Chemistry and Physics: 61st ed. CRC Press: Boca Raton, FL, 1980.

Chapter 7. The Effect of Temperature on Iron Oxide Nanoparticle Formation

7.1.1. INTRODUCTION

This chapter will examine the effect of reaction temperature on the the size, morphology, and composition of the particles. Temperature will increase the kinetics of all reactions in the system. These rates are critical to the system's nucleation process and affect the number of nucleation sites formed and consequently the size of the particles. Thermodynamics play an important role in dictating the composition of oxide formed. By investigating the kinetics of different stages as a function of initial concentration of ferrous ions ($[\text{Fe}^{2+}]_0$) and in different radical scavenging environments we were able to establish the dependences of oxidation yield and particle size on $[\text{Fe}^{2+}]_0$ and to propose a mechanism that could explain the observed dependences. The mechanism shows that each kinetic stage involves both chemical reactions and mass transport and/or phase transformation processes and the reactions involve not only the chemical species that are already present in solution (such as OH^- for hydrolysis) but also radiolysis products (such as $\bullet\text{OH}$ and H_2O_2) that are continuously produced in the presence of a constant flux of γ -radiation.

Increasing temperature increase the rates of all of the chemical reactions and transport processes involved in the overall growth of oxide particles. However, the quantitative effect of temperature varies considerably depending on the process involved. A process with a higher activation energy is slower at room temperature, but its rate increases more rapidly with temperature. The reverse rates of equilibrium reactions also

increase with increasing temperature and the chemical system may reach thermodynamic equilibrium state faster.

Because of the different dependences of the rate constants of the individual processes on temperature, changing temperature can influence the oxide formation and growth pathways and/or the size, morphology and composition of the particles formed by γ -radiation. This study explores the effect of temperature on radiolysis-induced oxide nanoparticle formation and growth. This work limits its study to the effect of initial Fe^{2+} concentrations in the range of 0.5 mM at an initial pH of 6. This range lies below the solubility limit of Fe^{II} , but above the solubility limit of Fe^{III} .

7.2. EXPERIMENTAL

7.2.1. Sample Preparation

All solutions were freshly prepared before each experiment with water, purified using a NANOpure Diamond UV ultrapure water system, with a resistivity of 18.2 M Ω ·cm. High-purity ferrous sulfate was obtained from Sigma-Aldrich (purity \geq 99%) and used without further purification. Pure water and aqueous solutions were deaerated by purging with ultra-high purity argon (impurity 0.001%) for more than one hour before solutions were prepared in an argon-filled glove box (O_2 level $<$ 0.1 vol.%). Solutions containing 0.5 mM Fe^{2+} were prepared with the pH adjusted to 6 using 1 N NaOH (added dropwise). The solution pH was measured using a pH meter (Mettler Toledo) inside the glove box. Aliquots of 10 mL of the prepared solutions were then transferred into 20 mL Pyrex vials (Agilent Technologies) and sealed using PTFE silicon septa.

7.2.2. Sample Irradiation

The vials were irradiated in a ^{60}Co gamma cell (MDS Nordion) as described in Chapter 3. The gamma source provided a uniform absorption dose rate of 0.8 Gy/s in the water samples at the time of this study. The samples were all irradiated at elevated temperatures in the range of 40 – 80 °C. The reaction vessel was heated to 40 °C before being lowered into the gamma cell irradiation chamber at which point the irradiation time started. The samples continued to heat to their desired final temperature and did so within ten minutes of irradiation initiation. Temperature profiles for tests targeting 60 and 80 °C are shown in Figure 7.1 to illustrate the exact deviation between the intended reaction temperature and the actual reaction temperature.

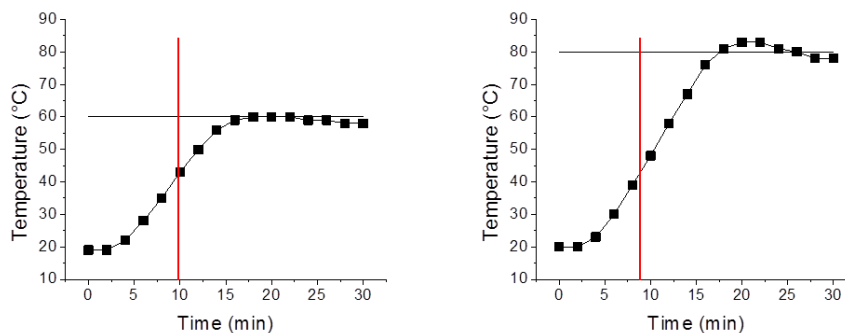


Figure 7.1: Temperature profiles of the reaction vessel. Irradiation began once the vessel reached 40 °C (the vertical red line) and reached the target temperature within 10 minutes of irradiation start time.

Samples were irradiated for 60 minutes in order to study the kinetics of the reaction. Once irradiation was completed, samples were immediately removed from the heat source and promptly cooled to room temperature by immersing the test vials in running water before analyses were undertaken. This time was minimized to reduce any reactions driven by temperature alone.

7.2.3. Sample Analysis

7.2.3.1. Gas Chromatography

After irradiation the headspace in the vials were sampled taken using an air-tight syringe with Luer lock at all time points. These samples were tested using gas chromatography to get the concentrations of both gaseous oxygen and hydrogen generated by water radiolysis.

7.2.3.2. UV-Vis Spectroscopy

The ferrozine method was used to determine the iron speciation of the sample. In this method, an aliquot of the sample at all time points was mixed with a ferrozine reagent. The volume of the aliquot varied with the initial concentration used. Ferrozine complexes with any Fe^{2+} in the solution to produce a complex with an absorbance at 563 nm with a molar extinction coefficient of $27900 \text{ M}^{-1}\text{cm}^{-1}$. Beer-Lambert's law is then used to determine the $[\text{Fe}^{2+}]$ in the solution. Another aliquot was mixed with hydroxylamine which reduces the Fe^{III} species present (both solids and in solution) to Fe^{2+} . This mixture was then mixed with the ferrozine reagent to determine the total concentration of iron in the system. The $[\text{Fe}^{\text{III}}]$ was then determined by taking the difference between these.

7.2.3.3. pH

Samples irradiated for all time points had their pHs taken using a pH meter (Mettler Toledo).

7.2.3.4. Transmission Electron Microscopy

Particles were collected by dipping a carbon-coated copper grid into the irradiated test solution and drying the sample grid in air. The TEM images were obtained with the electron microscope with electrons accelerated to 80 keV.

7.2.3.5. Raman Spectroscopy

Particles were collected from samples irradiated for 60 minutes. The samples were collected and centrifuged and left on a glass slide to dry. Raman scattering measurements to determine the particle oxide composition were performed using a Renishaw model 2000 Raman spectrometer with a laser excitation wavelength of 633 nm.

7.2.3.6. X-ray Absorption Near Edge Structure

Dried samples were obtained and had X-ray absorption near edge structure measurements were performed using the Soft X-Ray Micro characterization Beam (SXRMB) at the Canadian Light Source in Saskatoon. The particle samples were irradiated with the light source was set in the range of 7100 – 7180 eV which corresponds to the range over which the characteristic Fe K-edge absorption. The resulting fluorescent X-ray emission spectrum was collected to determine bulk sample characteristics, while the ejected electron spectrum was collected to analyze the sample surface composition.

7.3. RESULTS AND DISCUSSION

7.3.1. Radiolysis Kinetic Modeling

Due to the time required for heating a test solution to a desired temperature (Figure 7.1) the analyses of the gaseous and solution species and oxide particles as a function of time, particularly in Stage 1 and Stage 2, could not be performed. Instead the analyses were performed for 1-h irradiated samples at different temperatures. In our previous studies we have established that the radiolysis-induced oxide formation and growth involves the aqueous oxidation of Fe^{2+} by $\bullet\text{OH}$ in Stage 1 and the surface oxidation of adsorbed $\text{Fe}^{2+}_{(\text{ad})}$ by H_2O_2 in Stage 2. However, to estimate the effect of temperature on the concentrations of $\bullet\text{OH}$ and H_2O_2 that control the overall oxide formation and growth kinetics in Stage 1 and Stage 2, we have performed calculations using the radiolysis kinetic model described in the previous chapters. In this model, the effect of temperature on the overall radiolysis kinetics is incorporated in temperature dependent values for the g-values of the primary radiolysis products, the density of water, and the rate constants of elementary solution reactions [1].

The modelling results for the radiolysis of pure water as a function of temperature at two pH values, 6.0 and 3.0, are presented in Figure 7.2. The calculations at pH 3.0 were performed because the previous studies have shown that the pH drops to about 3.0 as a result of hydrolysis of ferric ions that are formed by radiolytic oxidation of ferrous ions. The results for the radiolysis of 0.5 mM $[\text{Fe}^{2+}]_0$ solutions are presented in Figure 7.3.

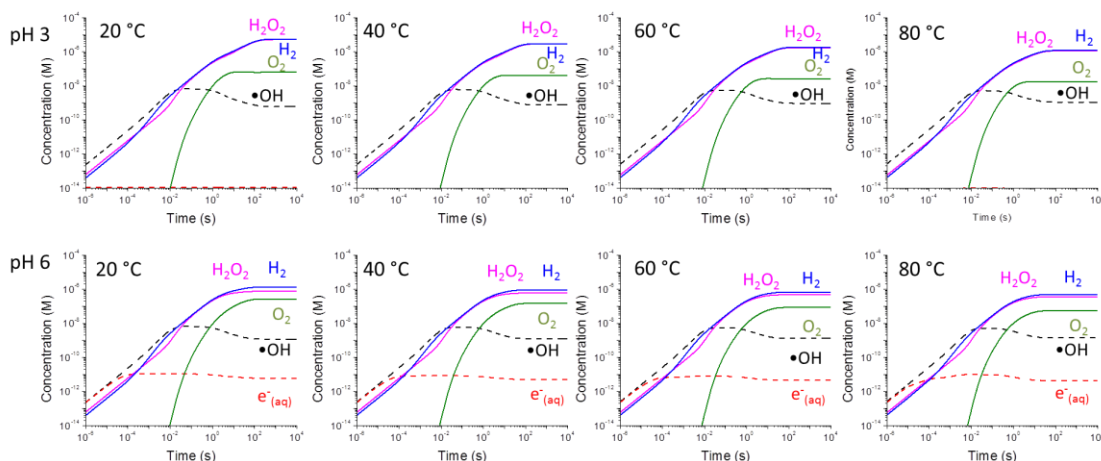


Figure 7.2: Computational modelling results for the radiolysis of pure water at different temperatures. The results obtained for two solution pHs, 6.0 and 3.0, are compared. Only the concentrations of key radiolysis products that are relevant to iron-oxide formation are shown although many more species are considered in the model.

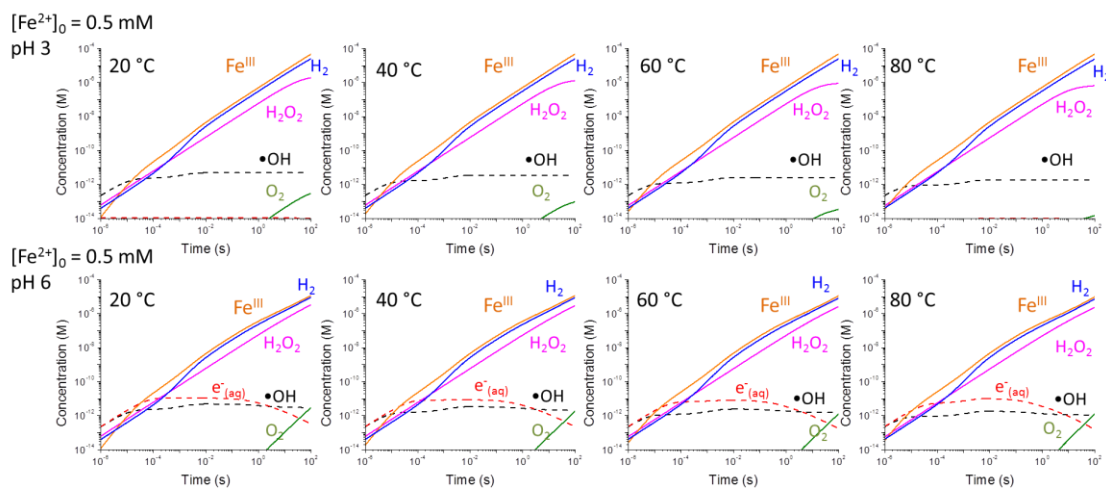


Figure 7.3: Computational modelling results for the radiolysis of 0.5 mM $[\text{Fe}^{2+}]_0$ solutions at different temperatures. The results obtained for two solution pHs, 6.0 and 3.0, are compared. Only the concentrations of key radiolysis products that are relevant to iron-oxide formation are shown although many more species are considered in the model. The concentration of Fe^{2+} remains nearly constant at 0.5 mM over the calculated reaction period of 100 s and hence, is not shown.

The calculations show temperature has a negligible effect on the concentrations of radiolysis products at short times (< 1 s). Temperature has a small effect on molecular

products, H_2O_2 , H_2 , and O_2 at longer times; increasing temperature from 20 to 80 °C decreases their concentrations at 1 h approximately by a factor of 2 at a given pH and $[\text{Fe}^{2+}]_0$. Decreasing pH from 6.0 to 3.0 decreases the concentration of $\bullet\text{e}^-_{(\text{aq})}$ significantly even at short times, but has a negligible effect on the key redox species, $\bullet\text{OH}$ and H_2O_2 , at times < 1 s and only a small effect (less than a factor of 2) at longer times.

As discussed in the previous studies the presence of Fe^{2+} affects the radiolysis kinetics, mostly via its reaction with $\bullet\text{OH}$ to produce Fe^{3+} [2]. Increasing temperature from 20 to 80 °C has a negligible effect on the solvation properties of water [1] and at a given pH has a negligible effect on the radiolytic production rate of Fe^{3+} at times < 100 s, and has a very small effect on the production of H_2O_2 at times > 10 s. On the other hand, decreasing pH from 6.0 to 3.0 at a given temperature and $[\text{Fe}^{2+}]_0$ has a small effect on the radiolytic production rate of Fe^{3+} at times > 0.1 s, and the production of H_2O_2 at times > 1 s. The calculated effect of pH on the net production of Fe^{3+} at times > 0.1 s arises from the reaction of Fe^{3+} with $\bullet\text{e}^-_{(\text{aq})}$.

In these calculations on the radiolysis of solutions containing Fe^{2+} and Fe^{3+} we did not consider the hydrolysis reactions of iron species, precipitation of ferrous and ferric ions or surface redox reactions of adsorbed species. Thus, the radiolysis model effectively only addresses the short-term kinetics when the heterogeneous reactions have negligible influence. Under continuous radiation as the ferrous and ferric ions precipitate and are incorporated into and thus grow oxide particles, the concentrations of Fe^{2+} and Fe^{3+} continuously change. Although the particle nucleation and heterogeneous oxidation are not modeled, the results presented in Figure 7.2 and Figure 7.3 indicate that increasing temperature within the studied range should have a negligible effect on the net radiolytic

production of key redox species, $\bullet\text{OH}$ and H_2O_2 . Temperature will, however, have a strong effect on slow thermal reactions.

7.3.2. Observed Effect of Temperature on Oxidation Yields After 1-h Irradiation

The $[\text{Fe}^{2+}]_{1\text{h}}$ and $[\text{Fe}^{\text{III}}]_{1\text{h}}$ after 1-h reaction time at different temperatures with or without irradiation are presented in Figure 7.4 respectively. Without irradiation $[\text{Fe}^{\text{III}}]_{1\text{h}}$ was below the detection limit of the ferrozine method at all temperatures studied and the $[\text{Fe}^{2+}]_{1\text{h}}$ was the same as $[\text{Fe}^{2+}]_0$. These results indicate that thermal oxidation of ferrous ions to ferric species is slow and is negligible over 1 h.

With radiation the $[\text{Fe}^{\text{III}}]_{1\text{h}}$ is measurable and decreases with temperature. However, the total iron concentration at 1 h ($[\text{Fe}_{(\text{total})}]_{1\text{h}}$) is smaller than the $[\text{Fe}^{2+}]_0$ and the difference increases with temperature. The cause of this apparent mass imbalance may be due to either or both of two issues. Some of the solid particles formed may have deposited on vial surfaces or sampling syringe surfaces removing iron from the solution that was then tested for iron content. Alternatively the reducing step in the ferrozine analysis may not have quantitatively reduced all of the ‘stable’ solid oxide particles. Although the deviation in total iron concentration after 1 h increases with temperature, the ratio of $[\text{Fe}^{\text{III}}]_{1\text{h}}$ to $[\text{Fe}^{2+}]_{1\text{h}}$ remains nearly constant with temperature. The near constant ratio with temperature indicates that the oxidation of ferrous to ferric species primarily occurs via reactions with radiolysis products rather than via thermal reactions.

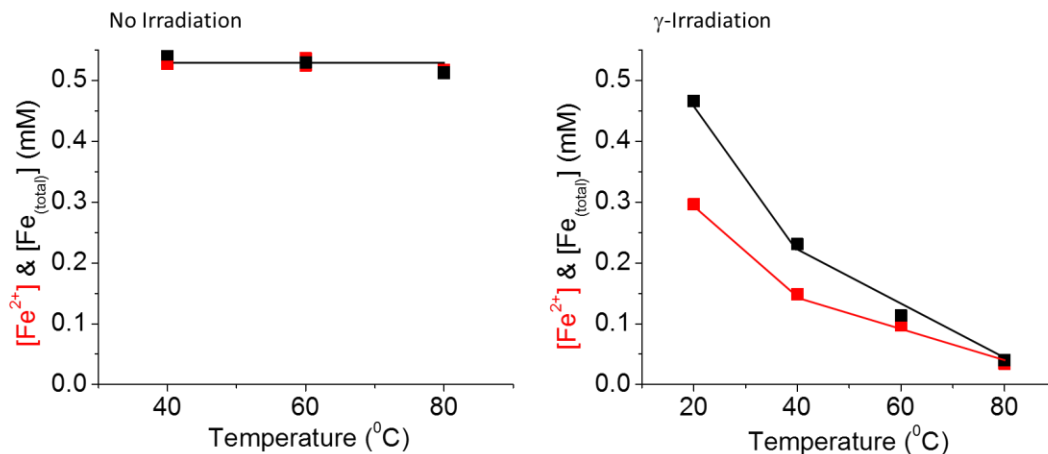


Figure 7.4: The measured concentrations of Fe²⁺ and Fe_(total) in the solution after one hour as a function of temperature with and without radiation.

In the previous studies on the effects of [Fe²⁺]₀ and radical scavengers on iron-oxide particle formation and growth kinetics (Chapters 4 and 6) we have shown that radical radiolysis product •OH is the dominant species for aqueous oxidation of Fe²⁺ to Fe³⁺ in Stage 1 while molecular radiolysis product H₂O₂ is the dominant species for surface oxidation of adsorbed species Fe²⁺_(ad) to Fe³⁺_(ad) in Stage 2. The radiolysis modeling results (Figure 7.2 and Figure 7.3) show The net radiolytic production rate for •OH in Stage 1 (lasting less than a few min at room temperature) is not expected to change significantly with temperature, because the [•OH] is not temperature dependent of the range of interest here.

The solution concentrations of molecular species, H₂ and H₂O₂, in pure water at pHs < 8.0 after 1 h of irradiation ([H_{2(aq)}]_{1h} and [H₂O₂]_{1h}) are very small [3]. The [H_{2(aq)}]_{1h} and [H₂O₂]_{1h} are calculated to be nearly independent of temperature (Figure 7.2) [3]. The [H₂O₂]_{1h} observed in pure water was below 10 μM near our detection limit of 3 μM at all temperatures. The production of H_{2(g)} in the headspace is, however, expected to increase

with temperature due to an increase in H_2 transfer rate from the solution to the gas phase with temperature [4]. Due to very low production rate of $H_{2(aq)}$ in pure water, the $H_{2(g)}$ accumulated in the headspace over 1 h ($[H_{2(g)}]_{1h}$) is still very small, and the $[H_{2(g)}]_{1h}$ was detectable only at temperatures above 50 °C (Figure 7.5).

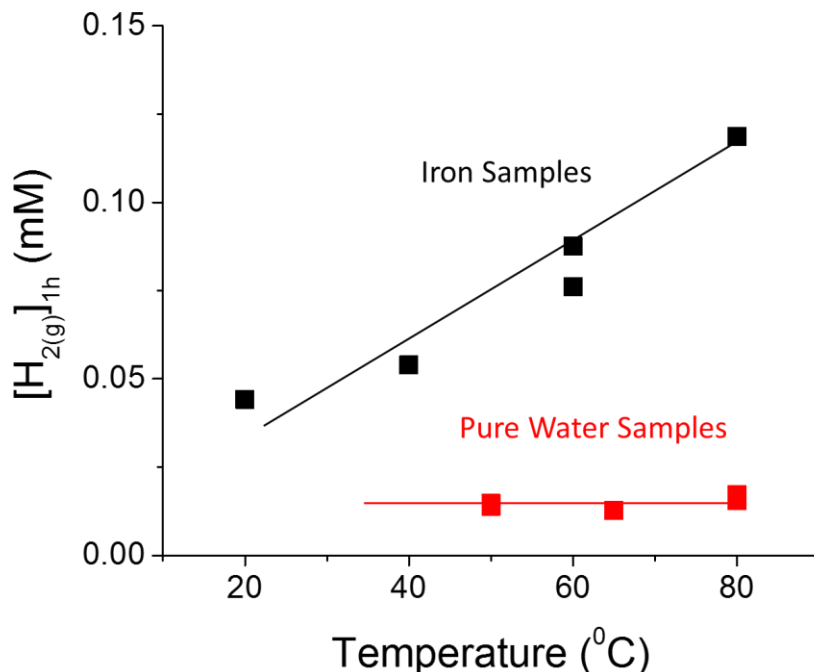


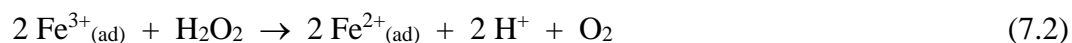
Figure 7.5: The hydrogen concentrations determined after an hour in a solution of either 0.5 mM $[Fe^{2+}]_0$ or pure water at pH 6.

Figure 7.5 shows that at a given temperature $[H_{2(g)}]_{1h}$ increases in the presence of 0.5 mM $[Fe^{2+}]_0$. The increase in $[H_{2(g)}]_{1h}$ corresponds to an increase in dissolved H_2 ($[H_{2(aq)}]_{1h}$). This increase is due to the reactions of ferrous and ferric species with radiolysis products occurring in solutions and on particle surfaces. The previous studies have established that the oxidation of ferrous to ferric species in Stage 1 occurs via reaction of Fe^{2+} with $\bullet OH$ in solution while the oxidation in Stage 2 occurs primarily via oxidation of adsorbed Fe^{II} by H_2O_2 on particle surfaces. The overall result of the radiolytic oxidation of

ferrous to ferric species is to increase $[\text{Fe}^{\text{III}}]_{1\text{h}}$ and $[\text{H}_{2(\text{aq})}]_{1\text{h}}$ at a given temperature. The increase in $[\text{Fe}^{\text{III}}]_{1\text{h}}$ due to 0.5 mM $[\text{Fe}^{2+}]_0$ can be seen from Figure 7.4, while the increase in $[\text{H}_{2(\text{aq})}]_{1\text{h}}$ due to 0.5 mM $[\text{Fe}^{2+}]_0$ can be seen from the $[\text{H}_{2(\text{g})}]_{1\text{h}}$ presented in Figure 7.5.

The constant ratio of $[\text{Fe}^{\text{III}}]_{1\text{h}}$ to $[\text{Fe}^{2+}]_{1\text{h}}$ with temperature suggests that the overall radiolytic oxidation of ferrous to ferric species does not change significantly with temperature. This is consistent with the radiolysis modeling results that show a negligible temperature effect on the radiolytic production of oxidants, $\bullet\text{OH}$ and H_2O_2 (Figure 7.2 and Figure 7.3). The negligible change in the overall radiolytic oxidation should lead to a negligible change in $[\text{H}_{2(\text{aq})}]_{1\text{h}}$ with increasing temperature. The increase in $[\text{H}_{2(\text{g})}]_{1\text{h}}$ with temperature can then be solely attributed to an increase in the interfacial transfer rate of H_2 with increasing temperature. Because of a higher $[\text{H}_{2(\text{aq})}]_{1\text{h}}$ with Fe^{2+} present, the effect of temperature on $[\text{H}_{2(\text{g})}]_{1\text{h}}$ is more noticeable.

Although increasing temperature has a negligible effect on the oxidation yield at 1 h it increases the rates of H_2O_2 reactions on particles surfaces. In the previous studies at room temperature we have suggested that at long times when most of the ferrous ions have converted to mixed $\text{Fe}^{\text{II}}/\text{Fe}^{\text{III}}$ particles, the oxidation rate of ferrous to ferric species by H_2O_2 (reaction 7.1) becomes equal to the reduction rate of ferric to ferrous species by H_2O_2 (reaction 7.2), establishing a redox cycle:



There is a quasi-equilibrium for the iron redox reactions, and dissolution and reprecipitation of ferrous and ferric ions continue (reactions 7.3 and 7.4). This results in particle growth through Ostwald ripening in Stage 3:



Large particles may settle gravitational at the bottom of a test vial or be captured less effectively by the micropipette used to extract a solution sample for testing. We can speculate that an increase in particle size with temperature could account for the decrease in $[\text{Fe}_{(\text{total})}]_{1\text{h}}$ with temperature that we have observed.

7.3.3. Effect of Temperature on Particle Composition

The chemical and phase composition of the particles formed after 1-h irradiation of 0.5 mM $[\text{Fe}^{2+}]_0$ solutions at different temperatures were characterized by XANES (x-ray absorption near edge spectroscopy) and Raman spectroscopy. For XANES, both the Fe K-edge total electron yield (TEY) and the X-ray fluorescence yield (FLY) spectra were taken. The FLY XANES is more sensitive to the bulk composition while the TEY is more sensitive to the surface composition. The TEY and FLY spectra of the particles formed at different temperatures are presented in Figure 7.6 and Figure 7.7. Also shown in the figure are the reference spectra of standard magnetite (Fe_3O_4) particles. The XANES spectra all show similar spectroscopic features, most closely resembling those of magnetite. The FLY spectra also nearly identical to the TEY spectra, indicating that there's no significant difference between the surface and bulk phases of the particles or, if present, a different surface layer is very thin.

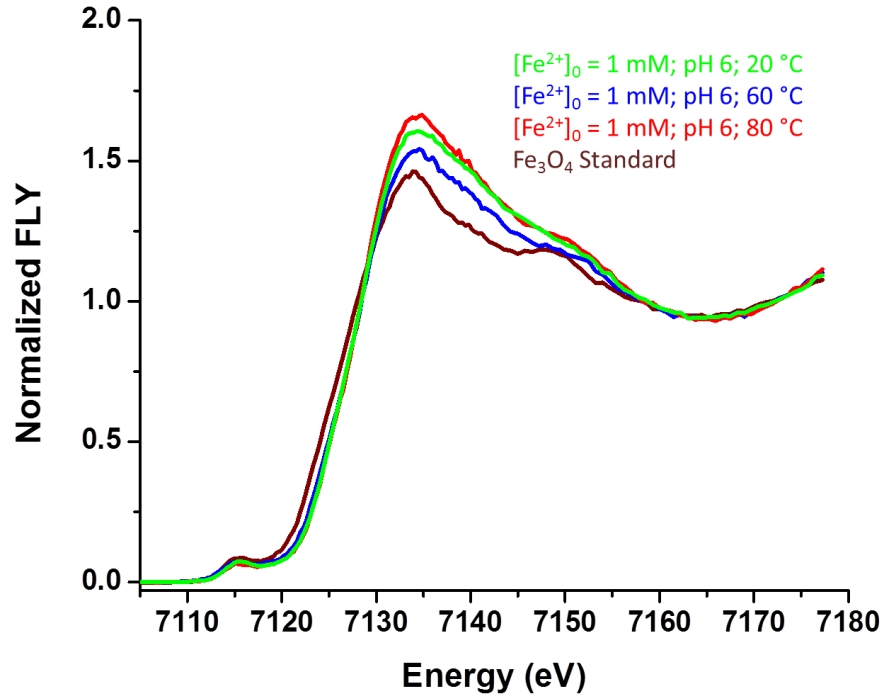


Figure 7.6: The fluorescent emission spectrum of three samples prepared with an initial pH of 6 and concentrations of 1 mM Fe^{2+} for 20 °C while 60 and 80 °C had concentrations of 0.5 mM. Each sample was prepared at a different temperature in the range of 20-80 °C. They are compared to a standard magnetite sample.

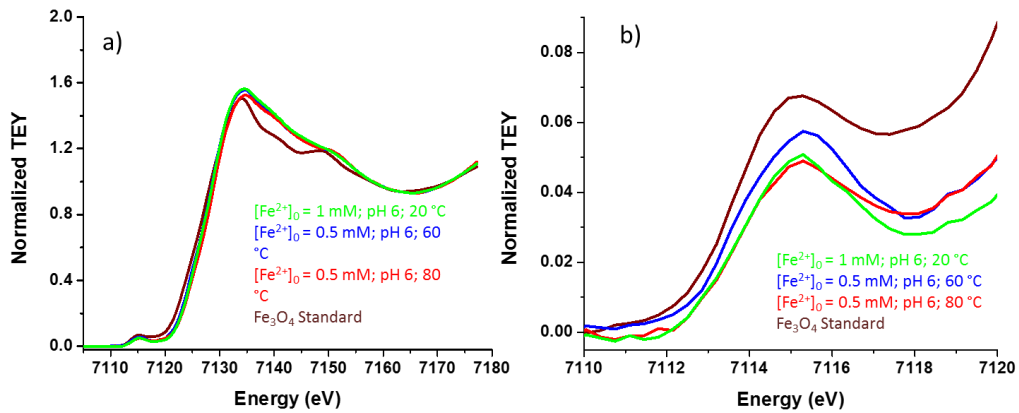


Figure 7.7: The electron emission spectrum of three samples prepared with an initial pH of 6 and concentrations of 1 mM Fe^{2+} for 20 °C while 60 and 80 °C had concentrations of 0.5 mM. Each sample was prepared at a different temperature in the range of 20-80 °C. They are compared to a standard magnetite sample. The graph on the left (a) is the full Fe K-edge while the graph on the right (b) is a magnification on the pre-K edge region.

The Raman spectra of the particles presented in Figure 7.8 show two broad bands, one over 250-500 cm^{-1} and the other over 600-800 cm^{-1} . In our previous studies, we have attributed the Raman peaks contributing to the broad band over 250-500 cm^{-1} to the vibrational modes associated with $\text{Fe}^{\text{III}}-\text{OH}$ and $\text{Fe}^{\text{III}}-\text{O}$ bonds, while the peaks contributing to the band over 600 to 800 cm^{-1} were attributed to the vibrational modes of mixed $\text{Fe}^{\text{II}}/\text{Fe}^{\text{III}}-\text{O}$ in spinel oxides ($\text{Fe}_3\text{O}_4/\gamma\text{-Fe}_2\text{O}_3$) [5, 6].

The relative intensities of the broad band centred at 700 cm^{-1} to the band centred at 400 cm^{-1} increases with increasing temperature. This temperature dependence is consistent with increases the rate of dehydration of adsorbed Fe^{II} and Fe^{III} hydroxides with increasing temperature and accelerating the growth of the mixed $\text{Fe}^{\text{II}}/\text{Fe}^{\text{III}}$ oxide (magnetite):

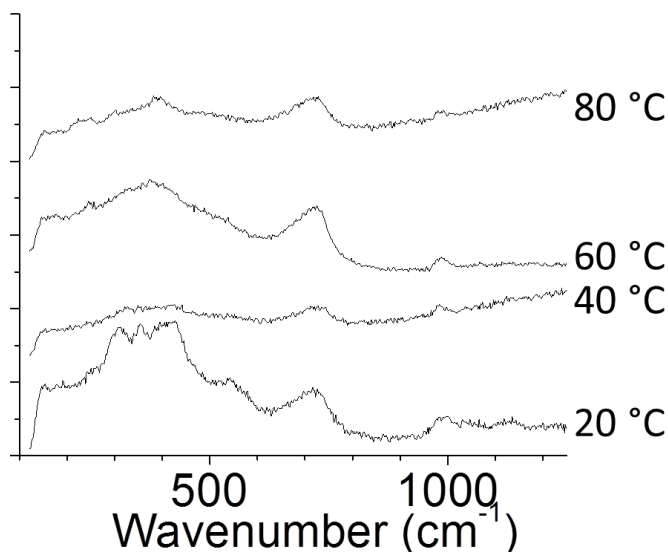


Figure 7.8: Raman spectra obtained from samples irradiated at the temperature indicated on the graph. The 20 °C sample was irradiated for five hours, while those irradiated at 40 °C or higher were irradiated for one hour.

7.3.4. Effect of Temperature on Particle Composition

The TEM images of the particles formed after 1-h irradiation of 0.5 mM $[\text{Fe}^{2+}]_0$ solutions at different temperatures are presented in Figure 7.9 and Figure 7.10. In previous studies we have established that the oxide particle growth at 20 °C is still in Stage 2 after 1-h irradiation at $0.8 \text{ Gy}\cdot\text{s}^{-1}$. The oxide particles grow in Stage 2 by the adsorption of ferrous ions, followed by surface oxidation of the Fe^{II} to Fe^{III} by H_2O_2 (reaction 1). The adsorbed $\text{Fe}^{2+}_{(\text{ad})}$ and $\text{Fe}^{3+}_{(\text{ad})}$ are then incorporated into a solid oxide phase of the growing particles, transforming into a specific oxide type. In Stage 2, the reduction of Fe^{III} to Fe^{II} by H_2O_2 (reaction 2) is still slow, the redox cycle between Fe^{II} and Fe^{III} has not yet been fully established, and growth by Ostwald ripening does not occur at any substantial rate. That is, in Stage 2, the particles grow by incorporating ferrous and ferric ions and hydroxide or oxygen anions onto existing particles (started from the nucleates formed in Stage 1) and thus, growing into particles with distinct oxide phase (magnetite at pH 6.0). These particles will be referred to as the primary particles hereafter.

The TEM images of the particles formed at higher temperatures (Figure 7.9) show that the primary particles start to aggregate earlier at a higher temperature. In addition, the individual particles that constitute the aggregates show different morphologies at different temperatures. At 40 °C particles of different sizes and densities are connected by light gel-like hydroxide (and form a gelatinous solid). At 60 °C the gel-like structure is no longer present and there are large primary particles (the dark dendritic spheres of 100-150 nm in size) and aggregates made of smaller primary particles.

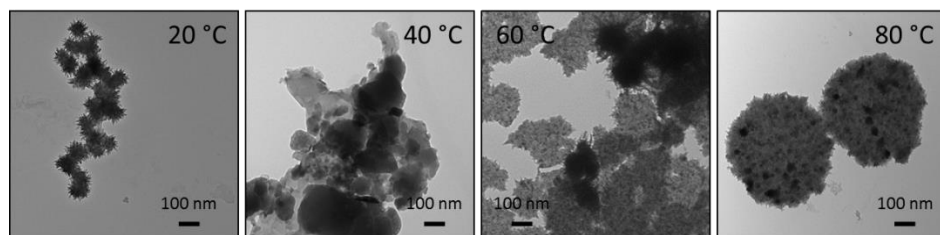


Figure 7.9: TEM images of the particles formed after 1-h irradiation of 0.5 mM $[\text{Fe}^{2+}]_0$ solutions at various temperatures (from left to right 20 °C, 40 °C, 60 °C and 80 °C).

At 80 °C, no large dendrite particles are present and the aggregates begin to grow into distinct shapes and sizes. The TEM images of different particle samples collected after 1 h of irradiation at 80 °C (Figure 7.10) indicate that the aggregation has not proceeded fully and there are various levels of aggregation present. The different aggregates show that small primary dendritic particles having dense cores and lighter outer layers become connected without losing their core oxide-phase structures.

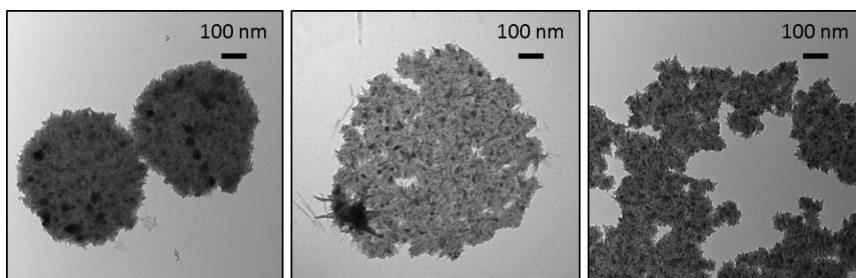


Figure 7.10: TEM images of particles all obtained from a sample with $[\text{Fe}^{2+}]_0 = 0.5$ mM, a pH of 6, heated to 80 °C, and irradiated for an hour.

7.3.5. Effect of Temperature on Particle Formation and Growth Kinetics

Although we could not obtain detailed kinetic information at elevated temperatures the observed dependences of oxidation yield and particle size and morphology on temperature provide some insights into how temperature affects the particle formation and

growth kinetics in each stage. The rates of oxide lattice formation, and the oxidation and reduction of adsorbed $\text{Fe}^{2+}_{(\text{ad})}$ and $\text{Fe}^{3+}_{(\text{ad})}$ by H_2O_2 can increase with increasing temperature. This will result in a faster conversion of mixed $\text{Fe}^{\text{II}}/\text{Fe}^{\text{III}}$ hydroxides in the outer layer of a growing particle into thermodynamically more stable magnetite. Faster redox reactions of adsorbed ferrous and ferric species by H_2O_2 establish the steady-state redox cycle (reactions 7.1 and 7.2) earlier. This will result in a shorter growth time and smaller initial particles, albeit with more stable cores. A higher temperature also promotes the rates of thermal dissolution and reprecipitation of the iron species (reactions 7.3 and 7.4). Typically, particles dispersed in solution change their sizes over time via Ostwald ripening; small particles dissolve and redeposit onto larger particles [7]. However, due to the accelerated dissolution and reprecipitation the primary particles aggregate through the formation of a gel-like network of hydroxides rather than through complete dissolution of smaller particles and reprecipitation onto larger particles. This growth mechanism is schematically shown in Figure 7.11.

At a higher temperature the formation of a magnetite particle core is faster. The core magnetite becomes more crystalline with fewer defects. Thus, the network of particles grows by aggregation of smaller individual particles with their magnetite cores still intact and distinct.

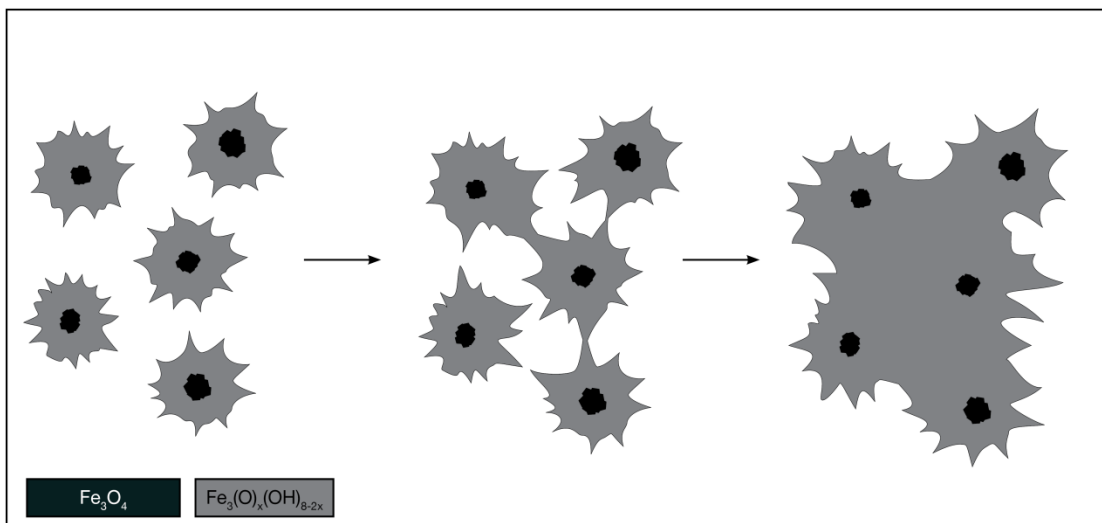


Figure 7.11: Schematic of the proposed particle growth mechanism of radiolysis-assisted Ostwald ripening.

7.4. CONCLUSIONS

The effect of temperature on γ -radiolysis induced formation and growth of iron oxide nanoparticles from dissolved ferrous ions was investigated. It was found that increasing temperature has a negligible effect on radiolytic production rates of $\bullet\text{OH}$ and H_2O_2 , but increases the rate of conversion of mixed $\text{Fe}^{\text{II}}/\text{Fe}^{\text{III}}$ hydroxides in the outer layer of initially formed particles into thermodynamically more stable magnetite. Thus, increasing temperature has a negligible effect on particle nucleation in Stage 1, but the particles grow to become more stable magnetite faster in Stage 2.

Increasing temperature increases the rates of both the oxidation of $\text{Fe}^{2+}_{(\text{ad})}$ and the reduction of $\text{Fe}^{3+}_{(\text{ad})}$ by H_2O_2 and establishes a steady-state redox cycle earlier. This results in a shorter growth time and smaller primary particles, albeit with more stable cores. The redox cycle also promotes the dissolution and reprecipitation of the iron species. At a

higher temperature this promotes the formation of a gel-like network of particles grows and the formation of aggregates of the individual primary particles.

7.5. REFERENCES

- [1] V. Subramanian, J.M. Joseph, H. Subramanian, J.J. Noël, D.A. Guzonas, J.C. Wren, *Journal of Nuclear Engineering and Radiation Science*, 2 (2016) 021021-1 – 021021-6.
- [2] P.A. Yakabuskie, J.M. Joseph, P. Keech, G.A. Botton, D. Guzonas, J.C. Wren, *Phys. Chem. Chem. Phys.*, 13 (2011) 7167-7175.
- [3] J.M. Joseph, B.S. Choi, P. Yakabuskie, J.C. Wren, *Radiat. Phys. Chem.*, 77 (2008) 1009-1020.
- [4] P.A. Yakabuskie, J.M. Joseph, J.C. Wren, *Radiat. Phys. Chem.*, 79 (2010) 777-785.
- [5] J. Bessiere, M. Perdicakis, B. Humbert, *C.R. Acad. Sci., Ser. IIC: Chim.*, 2 (1999) 101-105.
- [6] S. Das, M.J. Hendry, *Chem. Geol.*, 290 (2011) 101-108.
- [7] R. Boistelle, J.P. Astier, *J. Cryst. Growth*, 90 (1988) 14-30.

Chapter 8. The Effect of Dose Rate on the Iron Oxide Nanoparticles Formation

8.1. INTRODUCTION

The effect that different dose rates have on the kinetics of particle formation and general morphology is explored. Dose rate will significantly change the rate at which important radiolysis products are formed. These products, specifically the hydroxyl radical, are thought to play important roles in the mechanism of iron oxide particle formation especially at the early stages of particle growth.

This work limits its study to the effect of initial Fe^{2+} concentrations in the range of 0.5 mM at an initial pH of 6. This range lies below the solubility limit of Fe^{II} , but above the solubility limit of Fe^{III} .

8.2. EXPERIMENTAL

8.2.1. Sample Preparation

All solutions were freshly prepared before each experiment with water, purified using a NANOpure Diamond UV ultrapure water system, with a resistivity of 18.2 M Ω -cm. High-purity ferrous sulfate was obtained from Sigma-Aldrich (purity $\geq 99\%$) and used without further purification. Pure water and aqueous solutions were deaerated by purging with ultra-high purity argon (impurity 0.001%) for more than one hour before solutions were prepared in an argon-filled glove box (O_2 level < 0.1 vol.%). Solutions containing 0.5 mM Fe^{2+} were prepared with the pH adjusted to 6 using 1 N NaOH (added dropwise). The solution pH was measured using a pH meter (Mettler Toledo) inside the glove box.

Aliquots of 10 mL of the prepared solutions were then transferred into 20 mL Pyrex vials (Agilent Technologies) and sealed using PTFE silicon septa.

8.2.2. Sample Irradiation

The vials were irradiated in a ^{60}Co gamma cell (MDS Nordion) as discussed in Chapter 3. To study dose rate, these experiments were compared to analogous experiments performed by Yakabuskie et al. [1]. The earlier work was performed in the same Co^{60} gamma cell as the studies performed in this thesis. The half-life of Co^{60} is 5.26 years [2]. This resulted in a dose rate of 1.9 Gy/s which is higher than the 0.8 Gy/s studied herein.

8.2.3. Sample Analysis

8.2.3.1. UV-Vis

The ferrozine method was used to determine the iron speciation of the sample. In this method, an aliquot of the sample at all time points was mixed with a ferrozine reagent. The volume of the aliquot varied with the initial concentration used. Ferrozine complexes with any Fe^{2+} in the solution to produce a complex with an absorbance at 563 nm which has a molar extinction coefficient of $27900 \text{ M}^{-1}\text{cm}^{-1}$. Beer-Lambert's law is then used to determine the $[\text{Fe}^{2+}]$ in the solution. Following this, another aliquot is reduced using hydroxylamine which reduces the Fe^{III} species (both solids and in solution) to Fe^{2+} . This is then mixed with the ferrozine reagent in order to determine the total concentration of iron in the system. The $[\text{Fe}^{\text{III}}]$ is then determined by taking the difference between these.

8.2.3.2. TEM

Particles were collected by dipping a carbon-coated copper grid into the irradiated test solution and drying the sample grid in air. The TEM images were obtained with the electron microscope with electrons accelerated to 80 keV.

8.3. RESULTS

The topic of this thesis was brought about from evidence which emerged from earlier work. The dose rate of the previous study was 1.9 Gy/s rather than the 0.8 Gy/s studied herein [1]. Two main differences were observed between these studies and those performed at a higher dose rate. The first main observation is that the degree of oxidation increased with higher dose rate (Figure 8.1).

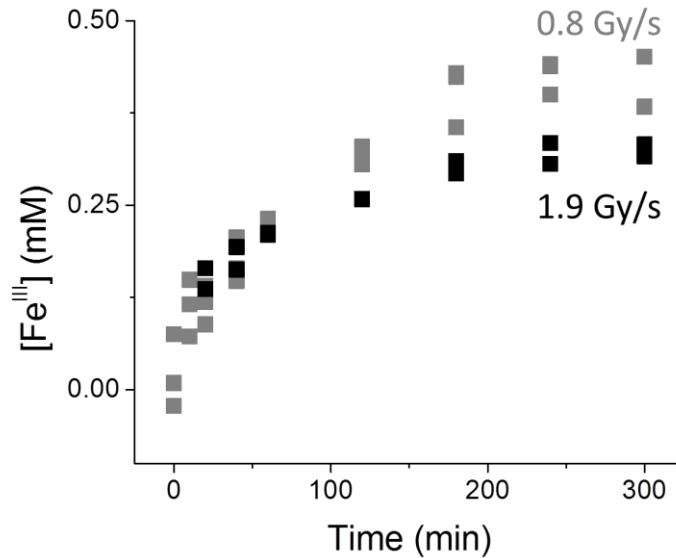


Figure 8.1: The concentration of Fe^{III} in solution as a function of irradiation time. Both systems modelled had $[\text{Fe}^{2+}]_0 = 0.5 \text{ mM}$. One system (black) had a dose rate of 1.9 Gy/s and a pH of 5.5, while the other (grey) had a dose rate of 0.8 Gy/s and a pH of 6.

The second main observation is that the particle size is smaller (Figure 8.2). Table 8.1 shows the comparison of the particles grown at different dose rates. This result is consistent with studies involving the generation of zero valent metal nanoparticles [3-5]. The studies were performed at different initial pH values. In Chapter 5, larger particles were produced at lower pH values. The particles produced with a dose rate of 1.9 Gy/s are smaller despite also a lower pH, thus the difference in size is attributed to the dose rate. The hydroxyl radicals are the species responsible for the nucleation of these particles and thus an increased concentration results in more nucleates forming at the outset. These nucleates grow into particles, but because there are more of them the total iron content in the system is spread uniformly between them causing smaller particles. This explanation is consistent with the explanation for the same trend observed in other systems [5, 6].

Table 8.1: Average particle sizes and standard deviation determined at $[\text{Fe}^{2+}_{(\text{aq})}]_0 = 0.5$ mM. The sample with a dose rate of 0.8 Gy/s had an initial pH of 6 while that of 1.9 Gy/s had an initial pH of 5.5.

Dose Rate (Gy/s)	Population	Average Diameter (nm)	Standard Deviation (nm)
0.8	9	94	6
1.9	12	76	9

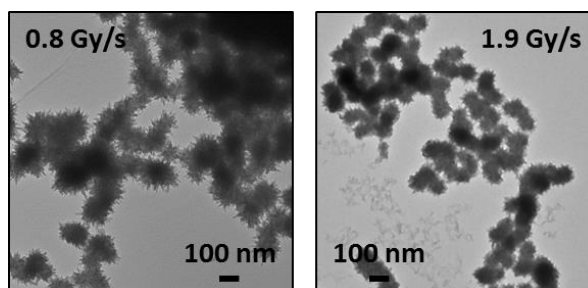


Figure 8.2: TEM images of particles obtained after 5 h of irradiation with $[\text{Fe}^{2+}]_0 = 0.5$ mM. The image on the left had a dose rate of 0.8 Gy/s and an initial pH of 6, while that on the right had a dose rate of 1.9 Gy/s and an initial pH of 5.5 which were obtained from Yakabuskie et al [1].

Figure 8.3 shows the concentrations of the relevant radiolysis products for systems both with and without Fe^{2+} initially in the system. The speciation of radiolysis products between dose rates are within an order of magnitude between each other indicating that there is no major change in the dominance of the various reactions. As indicated, the model does not accurately model the heterogeneous reactions occurring on the growing particle.

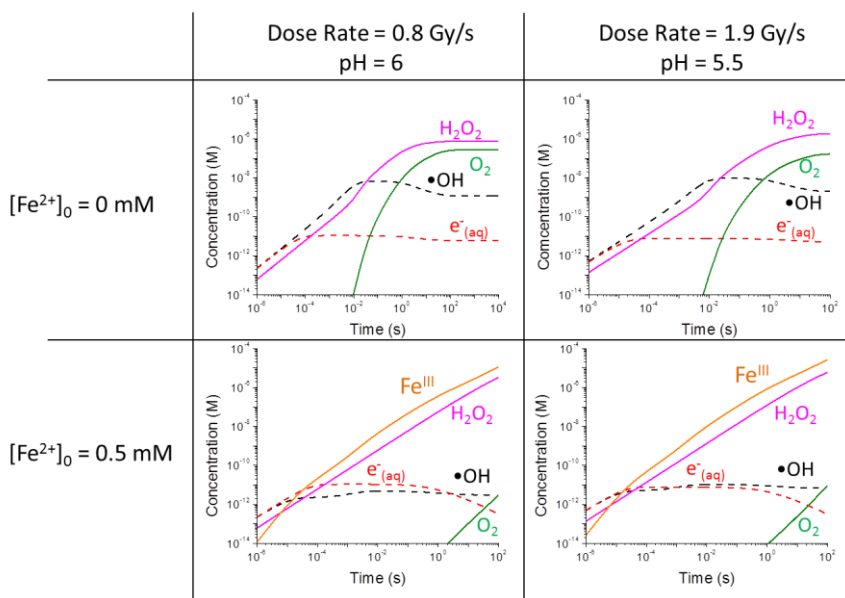


Figure 8.3: Computer modelling of the relevant radiolysis products as a function of irradiation time.

A closer look at the $[\text{Fe}^{\text{III}}]$ as a function of time, Figure 8.4, shows that the higher dose rate condition yields faster iron oxidation at these extremely short times.

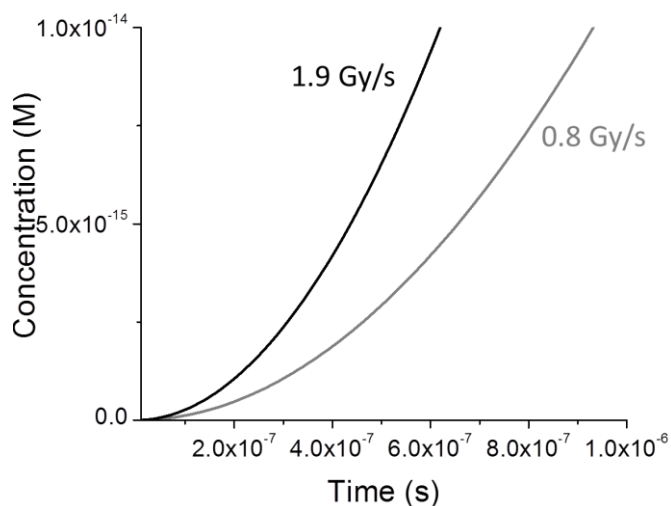


Figure 8.4: The concentration of Fe^{III} in solution as a function of irradiation time. Both systems modelled had [Fe²⁺]₀ = 0.5 mM. One system (black) had a dose rate of 1.9 Gy/s and a pH of 5.5, while the other (grey) had a dose rate of 0.8 Gy/s and a pH of 6.

As discussed in Chapter 4, at short times, the [Fe^{III}] is formed exclusively by the oxidation of Fe²⁺_(aq) by •OH. The rate of •OH production is proportional to the dose rate of the system.

$$\frac{d[\bullet\text{OH}]_t}{dt} \approx G_{\bullet\text{OH}} \cdot D_R \cdot \rho_{H_2O} \quad 8.1$$

$$[\bullet\text{OH}]_t \approx G_{\bullet\text{OH}} \cdot D_R \cdot \rho_{H_2O} \cdot t \quad 8.2$$

The hydroxyl radical will reach steady state much faster than the Fe²⁺_(aq) oxidation.

$$[\bullet\text{OH}]_{SS} \approx \frac{G_{\bullet\text{OH}} \cdot D_R \cdot \rho_{H_2O}}{k_{\bullet\text{OH}+\text{Fe}^{2+}} \cdot [\text{Fe}^{2+}]_0} \quad 8.3$$

$$-\frac{d[\text{Fe}^{2+}]_t}{dt} = \frac{d[\text{Fe}^{3+}]_t}{dt} \approx k_{\bullet\text{OH}+\text{Fe}^{2+}} \cdot [\bullet\text{OH}] \cdot [\text{Fe}^{2+}]_0 \approx G_{\bullet\text{OH}} \cdot D_R \cdot \rho_{H_2O} \quad 8.4$$

$$[\text{Fe}^{3+}]_t \approx G_{\bullet\text{OH}} \cdot D_R \cdot \rho_{H_2O} \cdot t \quad 8.5$$

From the above we see that an increase in dose rate will increase the rate of Fe^{III} generation.

8.4. DISCUSSION

The system follows the same general mechanism as outlined in Chapter 4, but briefly here:

In Stage 1 of particle formation, the Fe^{2+} is oxidized rapidly by the hydroxyl radical. With an increase dose rate the system exceeds saturation of Fe^{3+} faster and to a greater extent. This in turn results in a greater number of nucleation sites which are formed in this stage.

In stage 2, the Fe^{2+} must first adsorb onto the nucleate sites produced in Stage 1 where it is oxidized by hydrogen peroxide in a surface assisted process. The system seems to move through this stage a little faster with a higher dose rate which also lends itself towards smaller particles. A higher dose rate makes the system more reductively active and therefore the reduction of Fe^{III} by water radiolysis products becomes significant in a shorter time.

In stage 3, the system reaches its equilibrium point. Higher dose rates tend towards a more reducing system which reduces the overall oxidation yield of iron in the system at 5 hours.

8.5. CONCLUSION

The effect of dose rate was investigated and it was found that lower dose rates cause slightly higher oxidation yields and larger particles formed. Higher dose rates are associated with a faster rate of hydroxyl radical production. These radicals nucleate the system more completely. This coupled with less complete net oxidation, yield smaller particles.

8.6. REFERENCES

- [1] P.A. Yakabuskie, J.M. Joseph, P. Keech, G.A. Botton, D. Guzonas, J.C. Wren, *Phys. Chem. Chem. Phys.*, 13 (2011) 7167-7175.
- [2] M.P. Unterweger, D.D. Hoppes, F.J. Schima, *Nuclear Instruments & Methods in Physics Research Section A-Accelerators Spectrometers Detectors and Associated Equipment*, 312 (1992) 349-352.
- [3] F. Dumitrache, I. Morjan, R. Alexandrescu, V. Ciupina, G. Prodan, I. Voicu, C. Fleaca, L. Albu, M. Savoiu, I. Sandu, E. Popovici, I. Soare, *Appl. Surf. Sci.*, 247 (2005) 25-31.
- [4] J.H. Park, H.W. Kim, H.S. Kang, Y.H. Koo, B.C. Lee, *Mater. Res. Innovations*, 18 (2014) 678-684.
- [5] A. Abedini, F. Larki, E. Saion, A. Zakaria, M. Zobir Hussein, *Radiat. Phys. Chem.*, 81 (2012) 1653-1658.
- [6] A. Abedini, A.R. Daud, M.A.A. Hamid, N.K. Othman, E. Saion, *Nanoscale Res. Lett.*, 8 (2013).

Chapter 9. Summary and Future Work

9.1. SUMMARY

The formation of iron oxide nanoparticles by ionizing radiation was examined under a variety of conditions. The formation of iron oxide nanoparticles follows a three stage mechanism. In stage 1, the oxidation of Fe^{2+} by hydroxyl radical to produce Fe^{3+} is dominant. Once the system becomes supersaturated with Fe^{3+} it precipitates in the form of Fe^{III} hydroxides to form the initial nucleation sites. These nucleates can now catalyze further Fe^{2+} oxidation by way of heterogenous reactions which signals the beginning of stage 2. These reactions have lower activation energies than analogous ones in solution and are driven by weaker oxidants such as hydrogen peroxide. As the surface area of these particles increases, the reduction of Fe^{III} species becomes significant and the net oxidation in the system is attenuated. The oxidation still occurs quickly on the surface resulting in dendritic particles. Stage 3 occurs when the reverse reactions are able to counterbalance with the forward oxidation. In stage 3, the oxidation/reduction cycle continues, though net oxidation has stopped. The particles will continue to grow via radiation-assisted Ostwald ripening, though at a much slower rate and thus the particle size is dictated by this final equilibrium position. The composition of the particles grown is that of magnetite with small contributions from ferrihydrite and green rust.

The concentration of the initial Fe^{2+} alters the final redox equilibrium of the system. In stage 1, the conversion of Fe^{2+} to Fe^{III} is dependent on the rate of production of $\bullet\text{OH}$ by water radiolysis which is not impacted by the initial $[\text{Fe}^{2+}]$. At sufficiently low concentrations (0.1 mM) of Fe^{2+} all of the iron is oxidized in stage 1 and the system does

not grow into dendritic particles observed at all other concentrations. Higher concentrations undergo growth in stage 2, before finally settling into their final size in stage 3. Higher concentrations of Fe^{2+} in the system spend more time in stage 2 and ultimately reach larger sizes.

The pH of the initial system impacts the nucleation in stage 1. After this, the pH tends towards the 3.5 regardless of with which it started. Below a pH of 7, the pH impacts the solubility of Fe^{III} , in that more acidic solutions are able to solubilize it more effectively. Because Fe^{3+} is more soluble with lower pH values, fewer nucleates form. The solution pH does not change the oxidation yields of the solution therefore with lower pH solutions the same amount of iron becomes distributed over fewer nucleation sites which generate larger particles. Below pH 7, all particles formed were made of magnetite with some minor contributions from other oxides.

At pH values of 7 or higher, the system seemed to have nucleated prior to irradiation. As the particles grew in these systems, they would adsorb onto these initial nucleates and form a different composition, lepidocrocite. This composition persisted despite the system acidifying within minutes of irradiation.

Scavengers were used to study the importance of certain radiolytic products on the formation mechanism. A hydroxyl radical scavenger, t-butanol, was used to see its impact on the oxidation of the system. The presence of tert-butanol caused oxidation to diminish greatly and the resultant particles were much smaller. Beyond this, higher concentrations of tert-butanol further suppressed the rate of nucleation more than the rate of growth. Thus higher concentrations of t-butanol lead to larger particles than cases with lower concentrations of t-butanol because there are fewer relative nucleates on which the oxidized iron can grow.

Nitrous oxide, a solvated electron scavenger, was used to examine the importance of the reduction reactions. Oxidation occurred much quicker and more completely with nitrous oxide. The particles were smaller and lost their dendritic character. This was attributed to the loss of the oxidation/reduction cyclization. Most of the iron was oxidized by hydroxyl radicals via the stage 1 kinetics and therefore many nucleates persist and there was little heterogeneous growth on the nucleates.

Increasing the temperature to 80 °C did not alter the mechanism. It did accelerate the rate at which the system oxidized. Elevated temperatures destroy the size uniformity observed at room temperature. The particles formed were still predominantly magnetite, though the contributions from the thermodynamically unstable oxides were lost due to thermal conversions. Agglomeration of the particles and loss of the unstable oxides was attributed to the radiation-assisted Ostwald ripening which occurs much faster at higher temperatures.

Dose rate does not alter the mechanism. Higher doses lead to more rapid production of hydroxyl radicals. Low dose rates are capable of oxidizing the iron in the system more completely. More abundant nucleates and less thorough oxidation couple to produce smaller particles at high dose rates.

9.2. FUTURE WORK

This body of research has added to the understanding of nanoparticle formation in aqueous systems by gamma irradiation. Further experiments would clarify certain areas that are currently still at the fringes of understanding. A method of generating iron oxide nanoparticles was probed which satisfies one of the two main motivations of this work. This research lends understanding to the formation of iron nanoparticles in the primary heat

transport system, but is still in the preliminary phase of understanding this process under that set of conditions. Within the scope of the research a more comprehensive analysis of pH effects could be undertaken. This study limited itself to an upper pH of 8. This could be surpassed to bring conditions closer to those found within the primary heat transport system of a nuclear reactor. Temperature effects were only studied up to 80 °C which provides valuable information on the effect of temperature, but again, conditions in a nuclear reactor are much hotter (250 – 300 °C). On this same tangent, only trace amounts of iron would be soluble in the primary heat transport reactor system. Within these studies, a reduced concentration seems to prevent the formation of nanoparticles, but that is under the conditions studied. A much lower concentration of $\text{Fe}^{2+}_{(\text{aq})}$ would more accurately represent this phenomenon in nuclear reactor systems when coupled with elevated pH and temperature. Presently, commenting on the processes occurring in a nuclear reactor a mere speculation.

The systems studied herein were all small reaction vials with mostly stagnant systems with continuous irradiation. In a primary heat transport system, the system would only be irradiated periodically as it flowed through the core of the reactor. Studies on flowing water systems would also enhance current understanding and provide another possible lever to control growth rate and morphology. As is currently proposed, diffusion of species to the surface of the growing particle is the rate determining step of the particle growth. Flow studies would accelerate said diffusion rate and therefore further validate or undermine our model.

Though studies were performed with the intention of controlling particle composition and morphology through control over reaction parameters, no studies were performed to functionalize these particles post-synthesis. Nanoparticles have found use in

a number of growing fields. The particles generated here were generated in a clean and sterile system without the addition of potentially toxic additives, thus they provide a facile route for particle synthesis. The use of these particles could be greatly enhanced if they have functionality imbued upon them beyond simply being iron oxides.

As was discussed, similar studies have been carried out on other transition metals. A notable void in understanding is the behaviour of systems with multiple soluble metal species. With iron, the dominant precipitation process is oxidation by hydroxyl radicals and the dominant growth process is oxidation by peroxide. Different metals have different dominant precipitation processes, in some cases the reduction brings about precipitation. Combining these metals into a one-pot synthesis of particles might have a variety of unique properties. A difference in precipitation rates may lead to complex oxide alloys. If the affinity of one metal lends itself to fast precipitation, but the other metal to fast growth on the nucleated site, vastly differences in the core and shell compositions may emerge. Metals which oxidize to precipitate may form a synergistic relationship with those that reduce to precipitate. This branch of research could also expand to functionality of particles generated by this method.

Finally, this work was built upon the simple observation that an iron coupon allowed to corrode freely in stagnant water which is being irradiated generated a cloudy solution. As such, the final branch that remains to be studied is the growth of particles in solution where the iron cation originated from a sample of metallic iron. The oxide growth on the metal undergoes a similar kinetic process as the growth of the particles, it is the nucleation step that really differentiates these processes. The growth behaviour of the oxide layer on the metal will depend on its morphology, which will in turn influence the long term kinetics of the particles formed. The effect these processes have on one another in

order would help clarify the mechanism in primary heat transport system of a nuclear reactor. The most comprehensive study would be that of metallic iron samples freely corroding in flowing water which is irradiated periodically at a pH of 10.6 and a temperature in the range of 250 – 300 °C, which would give specific insight into the size and morphology of particles formed under these conditions. In the primary heat transport system of a nuclear reactor, the coolant is being irradiated by neutron particles as well as gamma radiation.

Appendix A: Copyrights

**ROYAL SOCIETY OF CHEMISTRY LICENSE
TERMS AND CONDITIONS**

Aug 09, 2016

This Agreement between Thomas I Sutherland ("You") and Royal Society of Chemistry ("Royal Society of Chemistry") consists of your license details and the terms and conditions provided by Royal Society of Chemistry and Copyright Clearance Center.

License Number	3924871360928
License date	Aug 09, 2016
Licensed Content Publisher	Royal Society of Chemistry
Licensed Content Publication	Physical Chemistry Chemical Physics
Licensed Content Title	Iron oxyhydroxide colloid formation by gamma-radiolysis
Licensed Content Author	P. A. Yakabuskie, J. M. Joseph, P. Keech, G. A. Botton, D. Guzonas, J. C. Wren
Licensed Content Date	Mar 11, 2011
Licensed Content Volume Number	13
Licensed Content Issue Number	15
Type of Use	Thesis/Dissertation
Requestor type	academic/educational
Portion	figures/tables/images
Number of figures/tables/images	1
Format	electronic
Distribution quantity	5
Will you be translating?	no
Order reference number	
Title of the thesis/dissertation	MODEL OF THE FORMATION OF IRON OXIDE NANOPARTICLES BY IRRADIATION IN AQUEOUS MEDIA
Expected completion date	Sep 2016
Estimated size	160
Requestor Location	Thomas I Sutherland

Billing Type

Billing Address

Attn: Thomas I Sutherland

Total 0.00 CAD

Terms and Conditions

This License Agreement is between {Requestor Name} ("You") and The Royal Society of Chemistry ("RSC") provided by the Copyright Clearance Center ("CCC"). The license consists of your order details, the terms and conditions provided by the Royal Society of Chemistry, and the payment terms and conditions.

RSC / TERMS AND CONDITIONS

INTRODUCTION

The publisher for this copyrighted material is The Royal Society of Chemistry. By clicking "accept" in connection with completing this licensing transaction, you agree that the following terms and conditions apply to this transaction (along with the Billing and Payment terms and conditions established by CCC, at the time that you opened your RightsLink account and that are available at any time at .

LICENSE GRANTED

The RSC hereby grants you a non-exclusive license to use the aforementioned material anywhere in the world subject to the terms and conditions indicated herein. Reproduction of the material is confined to the purpose and/or media for which permission is hereby given.

RESERVATION OF RIGHTS

The RSC reserves all rights not specifically granted in the combination of (i) the license details provided by your and accepted in the course of this licensing transaction; (ii) these terms and conditions; and (iii) CCC's Billing and Payment terms and conditions.

REVOCAATION

The RSC reserves the right to revoke this license for any reason, including, but not limited to, advertising and promotional uses of RSC content, third party usage, and incorrect source figure attribution.

THIRD-PARTY MATERIAL DISCLAIMER

If part of the material to be used (for example, a figure) has appeared in the RSC publication with credit to another source, permission must also be sought from that source. If the other source is another RSC publication these details should be included in your RightsLink request. If the other source is a third party, permission must be obtained from the third party. The RSC disclaims any responsibility for the reproduction you make of items owned by a third party.

PAYMENT OF FEE

If the permission fee for the requested material is waived in this instance, please be advised that any future requests for the reproduction of RSC materials may attract a fee.

ACKNOWLEDGEMENT

The reproduction of the licensed material must be accompanied by the following acknowledgement:

Reproduced ("Adapted" or "in part") from {Reference Citation} (or Ref XX) with permission of The Royal Society of Chemistry.

If the licensed material is being reproduced from New Journal of Chemistry (NJC), Photochemical & Photobiological Sciences (PPS) or Physical Chemistry Chemical Physics (PCCP) you must include one of the following acknowledgements:

For figures originally published in NJC:

Reproduced ("Adapted" or "in part") from {Reference Citation} (or Ref XX) with permission of The Royal Society of Chemistry (RSC) on behalf of the European Society for Photobiology, the European Photochemistry Association and the RSC.

For figures originally published in PPS:

Reproduced ("Adapted" or "in part") from {Reference Citation} (or Ref XX) with permission of The Royal Society of Chemistry (RSC) on behalf of the Centre National de la Recherche Scientifique (CNRS) and the RSC.

For figures originally published in PCCP:

Reproduced ("Adapted" or "in part") from {Reference Citation} (or Ref XX) with

permission of the PCCP Owner Societies.

HYPertext LINKS

With any material which is being reproduced in electronic form, you must include a hypertext link to the original RSC article on the RSC's website. The recommended form for the hyperlink is <http://dx.doi.org/10.1039/DOI suffix>, for example in the link <http://dx.doi.org/10.1039/b110420a> the DOI suffix is 'b110420a'. To find the relevant DOI suffix for the RSC article in question, go to the Journals section of the website and locate the article in the list of papers for the volume and issue of your specific journal. You will find the DOI suffix quoted there.

LICENSE CONTINGENT ON PAYMENT

While you may exercise the rights licensed immediately upon issuance of the license at the end of the licensing process for the transaction, provided that you have disclosed complete and accurate details of your proposed use, no license is finally effective unless and until full payment is received from you (by CCC) as provided in CCC's Billing and Payment terms and conditions. If full payment is not received on a timely basis, then any license preliminarily granted shall be deemed automatically revoked and shall be void as if never granted. Further, in the event that you breach any of these terms and conditions or any of CCC's Billing and Payment terms and conditions, the license is automatically revoked and shall be void as if never granted. Use of materials as described in a revoked license, as well as any use of the materials beyond the scope of an unrevoked license, may constitute copyright infringement and the RSC reserves the right to take any and all action to protect its copyright in the materials.

WARRANTIES

The RSC makes no representations or warranties with respect to the licensed material.

INDEMNITY

You hereby indemnify and agree to hold harmless the RSC and the CCC, and their respective officers, directors, trustees, employees and agents, from and against any and all claims arising out of your use of the licensed material other than as specifically authorized pursuant to this license.

NO TRANSFER OF LICENSE

This license is personal to you or your publisher and may not be sublicensed, assigned, or transferred by you to any other person without the RSC's written permission.

NO AMENDMENT EXCEPT IN WRITING

This license may not be amended except in a writing signed by both parties (or, in the case of "Other Conditions, v1.2", by CCC on the RSC's behalf).

OBJECTION TO CONTRARY TERMS

You hereby acknowledge and agree that these terms and conditions, together with CCC's Billing and Payment terms and conditions (which are incorporated herein), comprise the entire agreement between you and the RSC (and CCC) concerning this licensing transaction, to the exclusion of all other terms and conditions, written or verbal, express or implied (including any terms contained in any purchase order, acknowledgment, check endorsement or other writing prepared by you). In the event of any conflict between your obligations established by these terms and conditions and those established by CCC's Billing and Payment terms and conditions, these terms and conditions shall control.

JURISDICTION

This license transaction shall be governed by and construed in accordance with the laws of the District of Columbia. You hereby agree to submit to the jurisdiction of the courts located in the District of Columbia for purposes of resolving any disputes that may arise in connection with this licensing transaction.

LIMITED LICENSE

The following terms and conditions apply to specific license types:

Translation

This permission is granted for non-exclusive world English rights only unless your license was granted for translation rights. If you licensed translation rights you may only translate

this content into the languages you requested. A professional translator must perform all translations and reproduce the content word for word preserving the integrity of the article.

Intranet

If the licensed material is being posted on an Intranet, the Intranet is to be password-protected and made available only to bona fide students or employees only. All content posted to the Intranet must maintain the copyright information line on the bottom of each image. You must also fully reference the material and include a hypertext link as specified above.

Copies of Whole Articles

All copies of whole articles must maintain, if available, the copyright information line on the bottom of each page.

Other Conditions

v1.2

Gratis licenses (referencing \$0 in the Total field) are free. Please retain this printable license for your reference. No payment is required.

If you would like to pay for this license now, please remit this license along with your payment made payable to "COPYRIGHT CLEARANCE CENTER" otherwise you will be invoiced within 48 hours of the license date. Payment should be in the form of a check or money order referencing your account number and this invoice number {Invoice Number}. Once you receive your invoice for this order, you may pay your invoice by credit card. Please follow instructions provided at that time.

Make Payment To:

Copyright Clearance Center

Dept 001

P.O. Box 843006

Boston, MA 02284-3006

For suggestions or comments regarding this order, contact Rightslink Customer Support: customercare@copyright.com or +1-855-239-3415 (toll free in the US) or +1-978-646-2777.

Questions? customercare@copyright.com or +1-855-239-3415 (toll free in the US) or +1-978-646-2777.

Curriculum Vitae

Thomas I. Sutherland, PhD Candidate

Department of Chemistry, The University of Western Ontario, London, ON, Canada, N6A 5B7

Education

- 09/2011-present:** Ph. D. Candidate in Chemistry
University of Western Ontario
“Radiation Induced formation of Nanoparticles”
Supervised by Dr. J. C. Wren
- 09/2007-04/2011:** B. Sc. With specialization in Chemistry
University of Western Ontario
“Oxidative Addition of Cyclic Peroxides to a Pt(II) Centre”
Supervised by Dr. R. J. Puddephatt

Research Related Employment History

- 2011-present:** Graduate Student
University of Western Ontario
Supervised by Dr. J. C. Wren

T.A. and other Teaching Experience

- 09/2015-04/2015:** General Help for Chemistry 1301
01/2015-04/2015: Laboratory Supervision Chemistry 3372
05/2014-12/2014: Instrument Preparation for Chemistry 3372/2272
01/2014-04/2014: Laboratory Supervision for Chemistry 3372
09/2013-12/2013: Laboratory Supervision for Chemistry 2272
01/2013-04/2013: Laboratory Supervision for Chemistry 3372
09/2012-12/2012: Laboratory Supervision for Chemistry 2272
01/2012-04/2012: Laboratory Supervision for Chemistry 3372
09/2011-12/2011: Laboratory Supervision for Chemistry 1100

Scholarships and Awards

- 2015:** Teaching Assistant Award in the Faculty of Science
- 2013-2015:** The CNS Scholarship for PhD Graduate Research
- 09/2011:** Christian Sivertz Scholarship
- 05/2011-08/2011:** NSERC-USRA
University of Western Ontario
Supervised by Dr. J. C. Wren

05/2010-08/2010: NSERC-USRA
University of Western Ontario
Supervised by Dr. R. H. Lipson

05/2009-08/2009: NSERC-USRA
University of Western Ontario
Supervised by Dr. R. H. Lipson

2008-2010: The Andrew and Sarah Hamilton Award

Publications

Pellarin, K.; McCready, M.; *Sutherland, T. I.*; Puddephatt, R. "Oxidative Addition of Phthaloyl Peroxide to Dimethylplatinum(II) Complexes. *Organometallics*" *Organometallics*. **2012**. *31*, 8291-8300.

Posters

T. I. Sutherland, P. Yakabuskie, J. C. Wren "The Effect of Initial Iron Concentration and pH on the Radiolytic Formation of Iron Oxide Nanoparticles" the 36th Annual CNS-CNA Student Conference, Saskatoon, Saskatchewan, June 10th-13th, 2012.

T. I. Sutherland, P. Yakabuskie, J. C. Wren "Radiolytic Formation of Iron Oxide Nanoparticles" the 38th Annual CNS-CNA Student Conference, Vancouver, British Columbia, August 24th-28th, 2014 and University Network of Excellence in Nuclear Engineering (UNENE) R&D Workshop and Poster Session, Toronto, Ontario, December 15th, 2014 (Honorable Mention)